Quasi-Free Scattering Studies in and Around the Ca Mass Region

Luke Rose

PhD

University of York

School of Physics, Engineering and Technology

September 2024

Abstract

Quasi-free scattering studies in the Ca mass region have been conducted by the R^3B collaboration at GSI in inverse kinematics, with the goal of studying the nuclear structure of both stable and exotic nuclei. This work focuses on studying the single-particle strength in this region, which is achieved through cross-section measurements. Preliminary quasi-free scattering cross sections have been calculated for both $^{A}X(p,2p)^{A-1}Y$ and $^{A}X(p,pn)^{A-1}X$ reaction channels for the Ca isotopic chain, with the use of CH_2 and C targets. Theoretical (p,2p) cross sections for Ca isotopes were calculated using single-particle cross sections deduced from quasi-free reaction theory based on the Eikonal model. Experimental spectroscopic factors have been calculated for quasi-free scattering (p,2p) reactions for the Ca isotopic chain assuming the orbit occupation expected by the independent particle model. The values are quenched and are consistent with (e,e'p) data for stable nuclei, showing a weak correlation with nuclear asymmetry, confirming earlier R^3B measurements using lighter nuclei. Additionally, research and development for a new target-recoil tracker based on monolithic active pixel sensors for the R^3B experiment are reported here for the first time. Together with the conceptual design for a full barrel configuration which is to be used at the planned FAIR facility.

KEYWORDS: quasi-free scattering, single-particle strength, exotic, monolithic active pixel sensors, ALPIDE.

Declaration

I declare that this thesis is a presentation of original work and I am the sole author. This work has not previously been presented for an award at this, or any other, University. All sources are acknowledged as References.

Acknowledgements

Thank you to STFC, GET_INvolved Programme, R^3B, my parents and grandparents for funding my PhD. I am extremely grateful to my grandad for his encouragement and support throughout my life. I would also not have achieved any of this without my parents reassuring me through difficult times. Thank you to my brother for inspiring me at a young age into science! I am very grateful to all my friends new and old for their support throughout my PhD! Thank you to my supervisor Stefanos Paschalis for providing the opportunity to write this thesis and to participate in exciting experiments. I would also like to express my gratitude to Haik Simon for supervising me during my stay in Germany and for always helping me when I needed it. I am eternally grateful to all the members of the R^3B collaboration for their help throughout my PhD, it is impossible for me to thank everyone by name. However a special thank you to Carlos Bertulani for providing theoretical calculations for the (p,2p) reactions and for being a great friend, Prost!

Contents

Chapter 1

Introduction

The nuclear shell model as developed by Mayer and Jensen [1, 2] is a fundamental concept in nuclear physics which explains the properties and structure of nuclei. The shell model is an example of an Independent Particle Model (IPM) which describes nucleons as non-interacting particles, each in its own Single Particle (SP) state. Nucleons experience a global mean field potential generated from all other nucleons in the system. Each single particle state has quantum numbers n, l and j for the radial momentum, orbital angular momentum and total angular momentum respectively. Both protons and neutrons are fermions which are particles with half-integer spins. They obey Fermi-Dirac statistics and the Pauli exclusion principle. Fermi-Dirac statistics are statistical distributions of many non-interacting fermions that are identical with discrete energy levels. It is possible to extend this framework to weakly interacting fermions, however, additional corrections or modifications are necessary to accurately describe their behaviour in such cases. Energy levels are filled according to the Pauli exclusion principle which states that no two identical fermions can exist in the same quantum system simultaneously [3]. While the independent particle picture of fermions in a mean field potential reproduces important nuclear properties, it is an approximation as the nucleons interact with each other and the emerging system departs from the Fermi gas picture. SP states in quantum systems are referred to as orbitals. Those with the same quantum numbers can form a shell or subshell. SP states experience a strong spin-orbit (SO) interaction, which is attractive for spins aligned with the orbital angular momentum and repulsive for

spins that are anti-aligned [4]. Nuclei with closed proton or neutron shells are called "magic" and the corresponding sum of nucleons "magic numbers". For nucleons, the magic numbers are 2, 8, 20, 28, 50, and 82, with an additional magic number of 126 for neutrons. Magic number nuclei have higher binding energies compared to their neighbours on the nuclear chart and thus an increased relative stability. There is clear experimental evidence that away from beta stability this picture breaks down and magic numbers are no longer valid or different magic numbers are observed [5]. This picture can also be extended to an inert core of closed shells, with a finite number of valence nucleons primarily responsible for the nucleus's characteristics, such as total angular momentum. A common way to probe the structure of the nucleus and in particular to study valence nucleons, is direct nuclear reactions, such as Quasi-Free Scattering (QFS) using leptonic or hadronic probes with large momentum transfer. To probe nuclei far from the valley of beta stability using QFS, fast radioactive ions can be scattered on a hydrogen target to measure experimental cross sections. Theoretically calculated SP cross sections can also be calculated using the QFS reaction mechanism on hydrogen targets. Spectroscopic factors (SF) for initial ground and final states can also be deduced using nuclear structure calculations. When comparing theoretical SF and experimentally calculated spectroscopic strength a so called "quenching" is observed [6],

$$\mathrm{R} = \frac{\sigma_{\mathrm{exp}}}{\sigma_{\mathrm{th}}}. \tag{1.0.1}$$

Here R is the average reduction factor, defined as the ratio of the experimentally measured inclusive cross section, σ_{exp}, to the theoretical cross section σ_{th} to states that lie below the nucleon threshold, for a specific reaction channel. The first experimental data produced to verify this quenching was performed using electron beams with stable targets. The benefit of electron beam experiments is that there is a high accuracy in the measurement. This is due to the well-understood nature of the electromagnetic interaction. Electrons experience minimal absorption effects in the nucleus and as they are fundamental particles with no internal structure they provide clean and precise probes of nuclei. High-energy electron scattering measurements typically have lower cross sections because the probability of interaction decreases with increasing energy and momentum transfer [7]. One of major results

of these experiments as seen in Figure 1.1, is that for stable nuclei using electron induced proton knockout, a quenching of the SF of between 60-70% is observed [8].

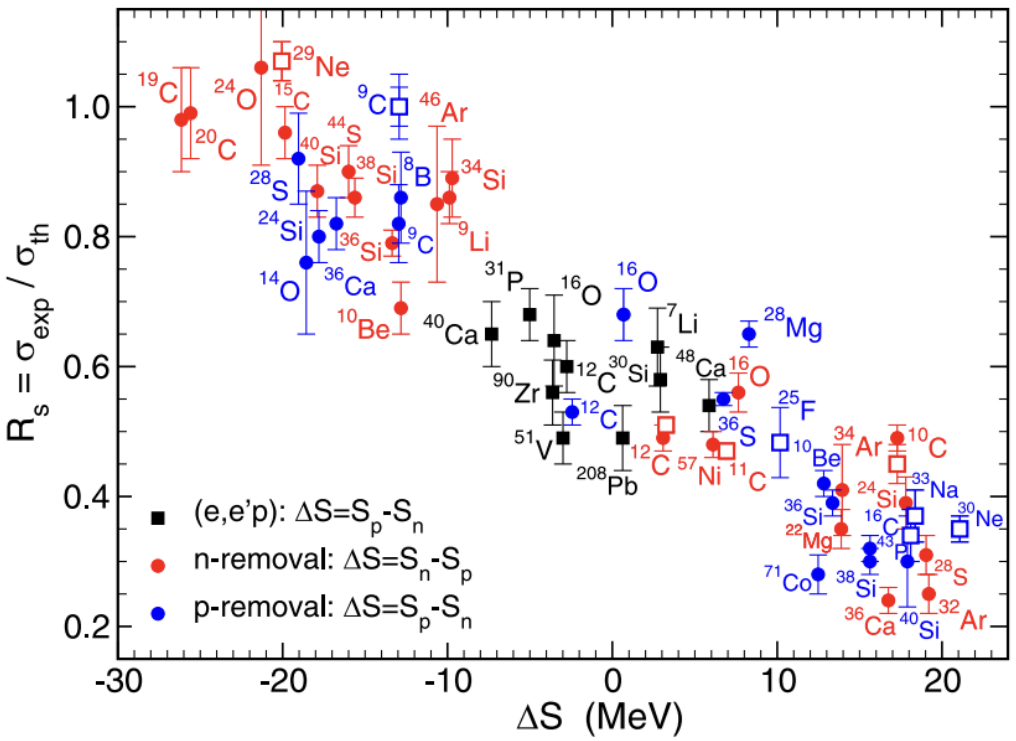

Figure 1.1: Plot taken from [9] showing the computed ratio of experimental and theoretical inclusive one-nucleon removal cross section R_s for two types of reaction, electron scattering (black square) and heavy-ion knockout reactions (red and blue circles).

This quenching has also been observed for nucleon transfer reactions [10]. The observed quenching of SF, along with its isospin dependence, is significant as it suggests the presence of correlations, particularly those not captured by shell model calculations. In the case of nucleon knockout reactions using light targets (Be, C, Li) with intermediate energy rare isotopic beams [9] a strong correlation between R and nuclear asymmetry is observed. QFS reaction studies in inverse kinematics at high beam energies have been conducted by the Reactions with Relativistic Radioactive Beams (R^3B) collaboration to probe this quenching [11, 12, 13]. Recent results for the oxygen isotopic chain are shown in Figure 1.2.

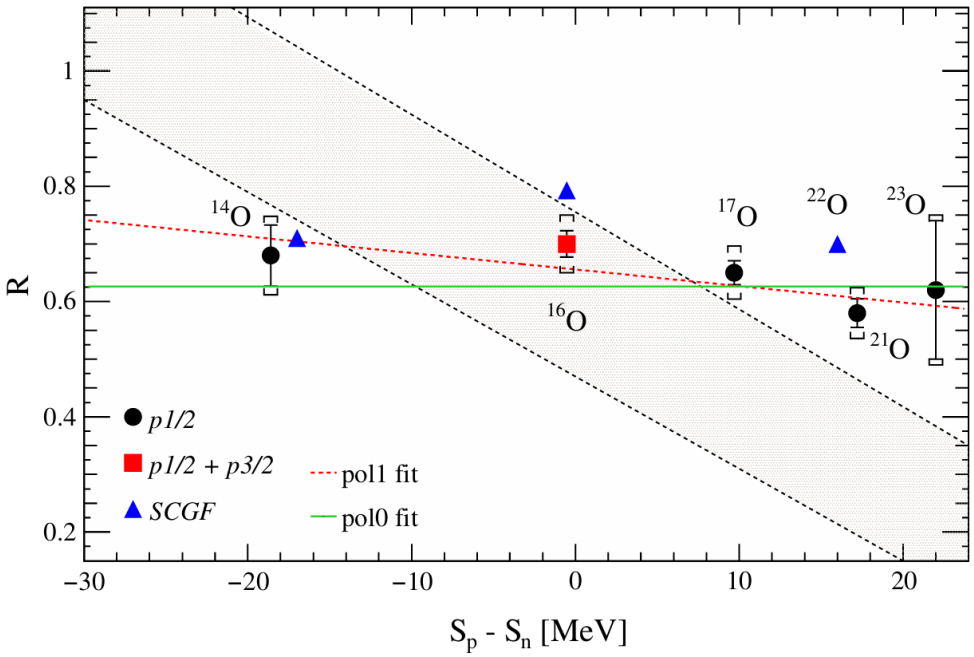

Figure 1.2: Plot taken from [14] showing the reduction factor R from (p,2p) reactions as a function of the difference in separation energies, S_p-S_n, across the oxygen isotopic chain. The shaded region shows the work of Gade et al. seen in Figure 1.1.

The grey banded diagonal region in Figure 1.2 represents points from Figure 1.1. The benefit of using this reaction probe is that in this energy regime absorption effects within the target is minimal. It is also possible to fully reconstruct the kinematics of all particles, measuring both the initial and final states. From QFS data published so far, there is no clear correlation between nuclear asymmetry and the reduction factor; instead, a more constant quenching is observed. The aim of this thesis is to extend QFS studies to the medium-mass region by investigating QFS in inverse kinematics, specifically within the Ca mass range. Studying this region of the nuclear chart offers many benefits, as the isotopic chains available offer a wide range of isotopes with varying degrees of nuclear asymmetry. Additionally, this area provides access to several magic and doubly magic nuclei, which have well-defined shell closures, such as ^{40}Ca and ^{48}Ca. In particular, the isotopes available in this experiment probe the robustness of the Z=20 shell gap as the neutron number varies from N<20 to N>28. Moreover, the relative energies of the d3/2, s1/2, and d5/2

proton shells vary when filling the f7/2 neutron orbit due to the effective proton-neutron interactions in the πsd—νf7/2 configurations and, in particular, due to the tensor force.

Chapter 2

Theoretical Overview

This chapter explores the theoretical frameworks and models essential for understanding nuclear reactions and structure, providing a foundation for interpreting experimental observations and analysing data. Throughout this chapter natural units will be used $\hbar = c = 1$.

2.1 Independent Particle Model

The nucleus is a complex system of interacting protons and neutrons, both of which are fermions composed of quarks and gluons, bound together by the strong force. Fully describing this many-body system starting from the nucleon-nucleon interaction is computationally possible for only the lightest nuclei, so mean field theoretical frameworks have been developed to simplify this picture. One such framework is the IPM which treats nucleons as non-interacting particles in an average spherically symmetric potential. Simplifying the many body problem from a system of A interacting particles to one of A independent particles. An additional simplification models the nucleus as two different Fermi-gases: one consisting of proton and one of neutrons. These Fermi gases weakly interact with each other in a confined volume with a constant potential. Nucleons can occupy all available energy levels according to the Pauli exclusion principle up to the maximum Fermi-energy, E_f [15]. The value of the Fermi momentum is derived from the condition that the total number

of occupied orbits must be equal to the number of particles,

$$p_f^p = \left(3\pi^2 \frac{\mathrm{Z}}{V_{\mathrm{vol}}}\right)^{\frac{1}{3}}, \qquad p_f^n = \left(3\pi^2 \frac{\mathrm{N}}{V_{\mathrm{vol}}}\right)^{\frac{1}{3}}. \tag{2.1.1}$$

Where V_{vol} is the volume of constant potential and p_f^p the Fermi momentum for the proton distribution and p_f^n for the neutron distribution, Z is the number of protons and N the number of neutrons in each gas. For symmetric nuclei the number of proton and neutrons is the same therefore,

$$\mathrm{Z} = \mathrm{N} = \frac{\mathrm{N}+\mathrm{Z}}{2} = \frac{\mathrm{A}}{2}. \tag{2.1.2}$$

Where A is the total number of protons and neutrons in a nucleus. Applying equation 2.1.2 to either nucleon distribution in equation 2.1.1 gives,

$$p_f = p_f^p = p_f^n = \left(3\pi^2 \frac{\mathrm{A}}{2V_{\mathrm{vol}}}\right)^{\frac{1}{3}}. \tag{2.1.3}$$

By assuming a spherical volume, the nuclear radius, R, can be calculated from,

$$R = R_0 \mathrm{A}^{\frac{1}{3}}. \tag{2.1.4}$$

Here R_0 is between 1.0 and 1.5 fm, depending on the calculation used and A is the mass number of the nuclei. Using a value of 1.2 fm the Fermi momentum is calculated to be,

$$p_f = \frac{1}{R_0}\left(\frac{9\pi}{8}\right)^{1/3} \approx 250 \text{ MeV/c}. \tag{2.1.5}$$

Where the conversion 1 fm = 197.3 MeV is used. The corresponding Fermi energy can also be calculated non relativistically as,

$$E_f = \frac{p_f^2}{2\mu} \approx 33 \text{ MeV}. \tag{2.1.6}$$

Here μ is the nucleon mass. This naive model yields already good estimations for the Fermi energy and momentum for nucleons at the Fermi surface. When one considers interactions between the nucleons, then the Fermi surface becomes defused and the valence nucleons have a finite probability to occupy levels above the Fermi energy and leave holes behind. These can be thought of as correlations that deplete the single-particle strength. In this picture the nucleons interact with the surrounding

medium and are no longer independent, they can therefore be described as quasi-particles. A more precise way of describing single particle states is to solve the many body Schrödinger equation,

$$\hat{H}\psi_\alpha(\vec{r},\sigma,\tau) = E_\alpha(\vec{r},\sigma,\tau). \tag{2.1.7}$$

In equation 2.1.7 the single particle wave function is represented by ψ_α with $\vec{r}$, σ, τ being the position vector, spin and isospin of each state, α respectively. The wave function is acted upon by a Hamiltonian operator, $\hat{H}$ producing an eigen solution E_α which corresponds to the energy of the system. The Hamiltonian operator can be expressed as a kinetic term and an interacting potential term,

$$\hat{H} = \sum_{i=1}^{\mathrm{A}} \frac{1}{2m_i}\nabla_i^2 + \sum_{i\neq j} V_{i,j}. \tag{2.1.8}$$

In equation 2.1.8 the first term is the kinetic operator for each nucleon to describe the motion in the nucleus. The second term of equation 2.1.8 represents a potential, which in the IPM is replaced by an average potential emerging from the average of the individual interactions between nucleons. Consequently, the Hamiltonian for a single nucleon becomes,

$$H(r) = -\frac{1}{2m}\nabla^2 + V(r). \tag{2.1.9}$$

For simplicity a Simple Harmonic Oscillator (SHO) with only radial dependence can be used,

$$V(r) = \frac{1}{2}m\omega^2 r^2. \tag{2.1.10}$$

The orbital angular momentum operator for a system can be expressed as,

$$\mathbf{L} = \mathbf{r} \times \mathbf{p}. \tag{2.1.11}$$

In equation 2.1.11, $\mathbf{r}$ is the position operator and $\mathbf{p}$ the momentum operator. The individual components of $\mathbf{L}$ obey commutation rules such that,

$$[\mathbf{L}_a, \mathbf{L}_b] = i\epsilon_{abc}\mathbf{L}_c, \qquad a,b,c \in \{x,y,z\}. \tag{2.1.12}$$

Where ϵ_{abc} is the 3 dimensional Levi-Civita tensor. The magnitude of the vector operator can be expressed by taking the dot product,

$$\mathbf{L}^2 = \mathbf{L}\cdot\mathbf{L} = \mathbf{L}_x^2 + \mathbf{L}_y^2 + \mathbf{L}_z^2. \tag{2.1.13}$$

The commutation relation between $\mathbf{L}^2$ and $\mathbf{L}$ is given by,

$$[\mathbf{L}^2, \mathbf{L}_a] = 0, \qquad a \in \{x, y, z\}. \tag{2.1.14}$$

The total angular momentum, $\mathbf{J}$, can be expressed as,

$$\mathbf{J} = \mathbf{L} + \mathbf{S}. \tag{2.1.15}$$

Where $\mathbf{S}$ is the spin quantum operator. The square of the total angular momentum operator is given by,

$$\mathbf{J}^2 = (\mathbf{L} + \mathbf{S})^2 = \mathbf{L}^2 + \mathbf{S}^2 + 2\,(\mathbf{L} \cdot \mathbf{S})\,. \tag{2.1.16}$$

Using the angular momentum operator it is possible to rewrite equation 2.1.9 and 2.1.10 in terms of spherical coordinates as,

$$H(r) = -\frac{1}{2mr^2}\left(\frac{\partial}{\partial r}\left(r^2\frac{\partial}{\partial r}\right) + \mathbf{L}^2\right) + \frac{1}{2}m\omega^2 r^2. \tag{2.1.17}$$

Here $\mathbf{L}^2$ acts on the spherical harmonic function $Y_{l,m}$ producing,

$$\mathbf{L}^2 Y_{l,m}\,(\theta, \phi) = l\,(l+1)\,Y_{l,m}\,(\theta, \phi)\,. \tag{2.1.18}$$

The spherical harmonic function has quantum numbers l and m indicating the degree and order of the function. The θ and ϕ simply represent the spherical coordinates. A centrifugal potential can be found by factoring out from equation 2.1.17,

$$V_{l^2}(r) = \frac{l(l+1)}{2mr^2}. \tag{2.1.19}$$

The SHO potential, however, is not a complete description of what has been experimentally observed, so further modifications to the potential can be introduced,

$$V(r) = V_{l^2}(r) + V_{l\cdot s}(r) + V_0(r). \tag{2.1.20}$$

Here $V_{l\cdot s}$ is the SO coupling potential and finally V_0 the central potential. While the SHO is convenient for carrying out analytical calculations, it extends to infinity and is unrealistic. As a further improvement the SHO is replaced by a centralised potential which can be found by considering the nuclear density distribution as a Fermi distribution,

$$V_0(r) = v_0 \int d^3r' f(r - r')\rho(r'). \tag{2.1.21}$$

Where v_0 gives the depth and $f(r - r')$ gives the shape of the potential well. The solution to equation 2.1.21 leads to a Woods-Saxon potential,

$$V_{\mathrm{WS}}(r) = \frac{-v_0}{1 + e^{\frac{r-R}{\mathrm{a}}}}. \tag{2.1.22}$$

The symbol a represents the surface thickness and R is the nuclear radius. It is possible to calculate R using equation 2.1.4 assuming the distribution is a hard sphere, however as Fermi-distributions are defuse spheres this is only a first order approximation. Each modification to the potential affects the shell structure of nuclei.

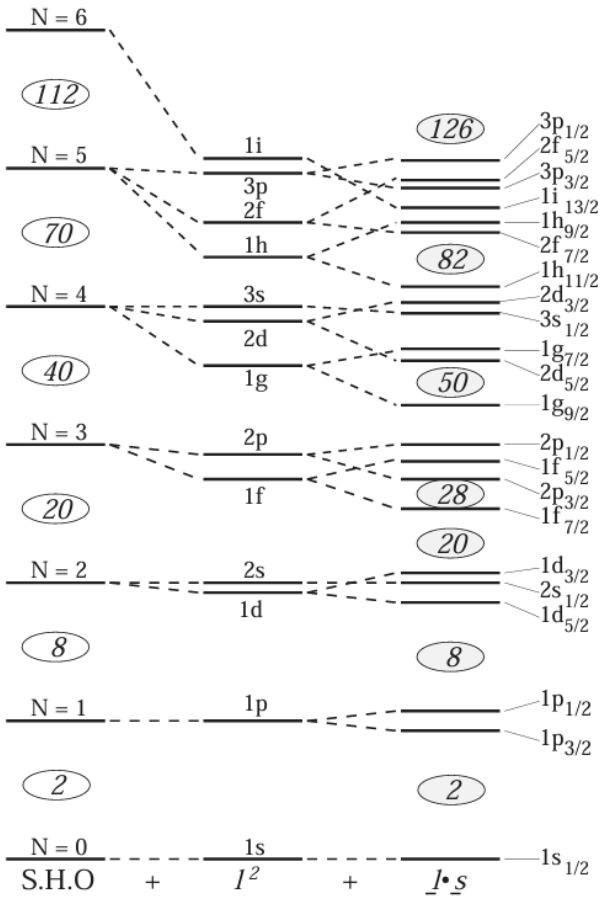

Figure 2.1: The spin orbit term causes a reordering of the nuclear shells from what the plain Woods-Saxon predicts and the emergence of the magic numbers at shell closures. Figure taken from [11].

Figure 2.1 shows that when considering only the SHO there are single shells. The inclusion of the angular momentum potential and Woods-Saxon is represented in the middle and shows now that orbitals and shell gaps are present. However, this does not reproduce the experimentally observed magic numbers. This is done by the inclusion of SO coupling which produces the orbital splitting that reproduces the magic numbers. The IPM assumes that nucleons move independently of each other within a average potential, however both short and long range interactions effect the structure of nuclei. This modifies the strength and configuration of shells close to the Fermi surface. To measure this effect one can take the overlap of the initial and final state wave functions after a nucleon is removed and express it as the sum of single particle states,

$$\langle \Psi_{\mathrm{A}-1}^{I_{\mathrm{A}-1}}(\vec{r}) \, | \Psi_{\mathrm{A}}^{I_{\mathrm{A}}}(\vec{r}) \rangle = \sum_{j=I_{\mathrm{A}}-I_{\mathrm{A}-1}}^{I_{\mathrm{A}}+I_{\mathrm{A}-1}} c_j \psi_j(\vec{r}). \tag{2.1.23}$$

In equation 2.1.23 I_{A} and $I_{\mathrm{A}-1}$ are the angular momentum of the initial and fragment nuclei respectively. By normalising the single particle states we get,

$$S_j = |c_j|^2. \tag{2.1.24}$$

This is a so called spectroscopic factor which can be used to link experimental data and theoretical calculations. The sum over all states of a specific orbital can be interpreted as the average occupancy number of that specific orbital. The theoretical cross section for a nucleon removal with SP quantum numbers n, l and j can be expressed as,

$$\sigma_{\mathrm{th}}(I_f) = \sum_j C^2 S(I_f, n, l, j) \sigma_{\mathrm{sp}}(n, l, j). \tag{2.1.25}$$

Here $\sigma_{\mathrm{sp}}(n, l, j)$ is the single particle cross section. The spectroscopic factor is given by C^2S where C^2 is the square of the isospin coefficient which is often set to 1. From Figure 1.1 and 1.2 it is seen that for both (e,e'p) knockout reaction and (p,2p) QFS reactions that for stable isotopes there is a quenching of 35-40% when comparing experiment to theory. With the ability to use relativistic beams for knockout reactions in inverse kinematics at intermediate energies it is now possible to study exotic nuclei.

2.2 Glauber Framework

The Glauber framework made famous by Roy Glauber in his series of lectures in 1959 is a way of explaining high-energy collisions between nuclei [16]. The framework consists of several approximations such as, the sudden approximation which is valid when the time interval of the reactions is shorter than the characteristic nuclear time of around 10^{-22} s [17]. Thereby one can assume that the nucleons are "frozen" during a reaction and do not participate in a reaction unless a collision occurs. The eikonal approximation is also then valid which treats the trajectory of particles as well defined straight lines, which aids with theoretical calculations. These approximations can also be expressed as,

$$\frac{\Delta E}{E} << 1 \tag{2.2.26}$$

$$\frac{\Delta \theta}{\theta} << 1 \tag{2.2.27}$$

$$\frac{\Delta k}{k} << 1 \tag{2.2.28}$$

Where E represents the energy transferred, θ is scattering angle of the beam and k is the momentum transferred. The symbol Δ then indicates the change in quantity. Equation 2.2.26 is the approximation that only a small amount of energy is transferred in a collision. Equation 2.2.27 is the approximation that only a small angular scattering occurs between the incoming nuclei and outgoing fragment. And finally equation 2.2.28 is the approximation that the collision only has small momentum transfer.

2.3 Quasi-Free Scattering

QFS is a direct reaction mechanism used to probe nuclei [7]. In inverse kinematics a bound projectile scatters off a stationary proton, subsequently a particle can be ejected which can be written as (p,pN) where N can be either a nucleon or a cluster of nucleons. At sufficiently high energies no other interaction should occur as the nucleon is removed from the projectile (no absorption). The spectator nucleons in the projectile remain unaffected, allowing for precise measurement of the knocked-out system. This enables the recovery of structural information about the parent

nucleus. The residual daughter nuclei can then be in an excited state containing holes. If the hole is produced below the Fermi surface, the nucleus will have an excitation energy $E^*_{\mathrm{A}-1}$,which can be measured if the hole state de-excites and emits a gamma ray, provided the transition is not forbidden. By applying energy conservation rules one can uncover this result,

$$B_N = S_N + E^*_{\mathrm{A}-1} = T_{\mathrm{A}} - (T_{\mathrm{A}-1} + T_{KO} + T_S). \tag{2.3.29}$$

This says that the binding energy B_N of the nucleus can be separated into the separation energy $S_N = (M_{\mathrm{A}} - M_{\mathrm{A}-1} - m_{\mathrm{N}})$ and the excitation energy $E*_{\mathrm{A}-1}$. The separation energy is the minimum energy required to remove a bound nucleon or cluster of nucleons from a nucleus of mass M_{A}. This is then equal to the energy conservation of all the particles involved. The kinematics of the reaction can be further examined when considering the momentum conservation. Figure 2.2 shows a Feynman diagram for the QFS interaction.

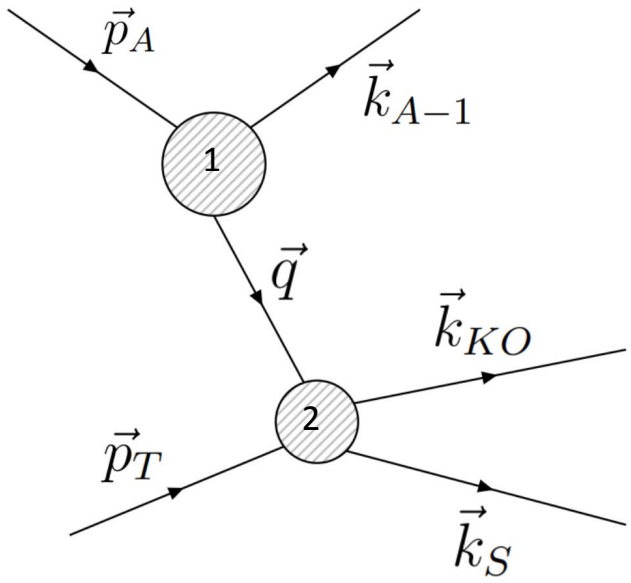

Figure 2.2: Feynman diagram describing the QFS (p,pN) reaction. Symbols are defined in the text.

Here, inverse kinematics are used, where $\vec{p}_{\mathrm{A}}$ is the four momentum for the parent nuclei with mass A. The target momentum $\vec{p}_T = (E_T, 0)$ as the target is at rest. The residual nucleus, the scattered proton and knocked out nucleon are represented by: $\vec{k}_{\mathrm{A}-1}$, $\vec{k}_S$ and $\vec{k}_{KO}$ respectively. The momentum transfer is denoted by $\vec{q}$, and index raising and lowering is performed using the mostly negative Minkowski metric,

$$\eta^{\mu\nu} = diag(1, -1, -1, -1), \tag{2.3.30}$$

The conservation of momentum for four vectors is given by,

$$\sum_i p_i^{\mu} = 0. \tag{2.3.31}$$

Using equation 2.3.31 the momentum conservation at each vertex in Figure 2.2 can be evaluated. Momentum conservation at vertex 1 is given by,

$$\vec{p}_{\mathrm{A}} - \vec{k}_{\mathrm{A}-1} = \vec{q}. \tag{2.3.32}$$

And for vertex 2,

$$\vec{q} + \vec{p}_T = \vec{k}_{KO} + \vec{k}_S \tag{2.3.33}$$

Then by equating both equation 2.3.32 and 2.3.33 to the momentum transfer $\vec{q}$ a relation between only non virtual particles is given by,

$$\vec{p}_{\mathrm{A}} + \vec{p}_T = \vec{k}_{\mathrm{A}-1} + \vec{k}_{KO} + \vec{k}_S. \tag{2.3.34}$$

This gives an equation for the momentum conservation for a QFS reaction. From [18] an equation for the separation energy of a removed nucleon is given by,

$$E_s = T_{\mathrm{A}} - \gamma(T_{KO} + T_S) - 2(\gamma - 1)m_p + \beta\gamma(k_{KO_{||}} + k_{S_{||}}) - \frac{q^2}{2M_{\mathrm{A}-1}}. \tag{2.3.35}$$

Here γ, β are the Lorentz factor and velocity of the incoming beam particle respectively. T_A, T_{KO} and T_S are the kinetic energies of the incoming beam particle the knocked out proton and the scattered proton respectively. Finally q^2 is squared magnitude of the internal momentum between vertex 1 and vertex 2.

2.4 Experimental Cross Sections

There are several different ways of representing the data from an experiment. Here the formalism for expressing cross section built on by Tanihata et al. [19] is presented:

- σ_{Elastic} : Total elastic cross section, projectile remains in its ground state and no nucleons are removed.
- $\sigma_{\text{Inelastic}}$: Total inelastic cross section, projectile is excited to a bound state, but no nucleons are removed.
- $\sigma_{\text{Interaction}}$: Total interaction cross section, nucleons are removed from the projectile.
- σ_{Reaction} : Total reaction cross section, all observable reaction channels.
- σ_{Total} : Total cross section, all possible reaction channels.

The total reaction cross section can be expressed as,

$$\sigma_{\text{Reaction}} = \sigma_{\text{Inelastic}} + \sigma_{\text{Interaction}}. \tag{2.4.36}$$

Both inelastic and interaction cross sections can be observed within an R^3B experiment directly, whereas the elastic cross section cannot. At high energies the inelastic cross section is very small and is suppressed via Pauli blocking in a nucleus-nucleus collision, therefore one can use the approximation,

$$\sigma_{\text{Reaction}} \approx \sigma_{\text{Interaction}}. \tag{2.4.37}$$

Furthermore one can decompose the interaction cross section into two reaction modes.

- $\sigma_{\Delta\text{Z}}$: Total charge changing cross section, charge of projectile is not equal to fragment.
- $\sigma_{\Delta\text{N}}$: Total neutron removal cross section, more than one neutron is removed from the projectile.

One can therefore express the total interaction cross sections as,

$$\sigma_{\text{Interaction}} = \sigma_{\Delta\text{Z}} + \sigma_{\Delta\text{N}}. \tag{2.4.38}$$

One can split the charge changing cross section into the sum of the proton removal cross section and the neutron removal cross section,

$$\sigma_{\Delta\text{Z}} = \sigma_{\tilde{\Delta}\text{Z}} + \sigma_{\tilde{\Delta}\text{N}}. \tag{2.4.39}$$

The interaction cross section can therefore be expressed as,

$$\sigma_{\text{Interaction}} = \sigma_{\tilde{\Delta Z}} + \sigma_{\tilde{\Delta N}} + \sigma_{\Delta N}. \tag{2.4.40}$$

The interaction cross section can also be calculated experimentally from a formula representing the beam current density as a function of target thickness,

$$\frac{dJ}{dz} = -\sigma_{\text{Interaction}} J(z)\tilde{T}. \tag{2.4.41}$$

Here $J(z)$ is the beam current at position z and $\tilde{T}$ is the number of scattering centres per unit length within the target which can be expressed as,

$$\tilde{T} = \frac{\rho N_a}{\text{A}}. \tag{2.4.42}$$

Where ρ is the density of the target, A is the mass number of the target material and N_a is Avogadro constant. Figure 2.3 is a diagram representing equation 2.4.41, where A_r is the area of the beam and L the target thickness.

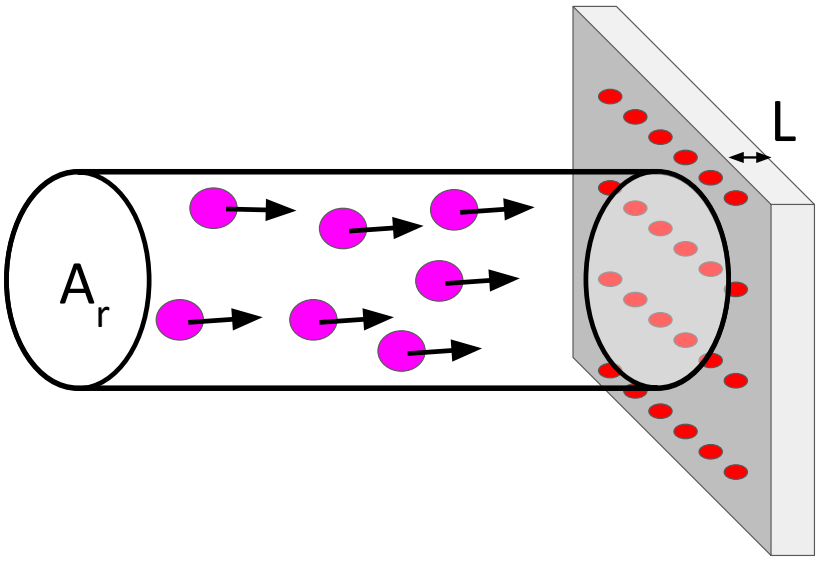

Figure 2.3: Diagram showing a cylindrical beam of particles with area A_r impinging on a target of thickness L.

Integrating equation 2.4.41 over the full length of the target gives,

$$\begin{aligned} \int \frac{1}{J} dJ &= -\int_0^L \sigma_{\text{Interaction}} \tilde{T} \\ ln(J(L)) - ln(J(0)) &= -\sigma_{\text{Interaction}} \tilde{T} L \\ J(z) &= J(0) e^{-\sigma_{\text{Interaction}} \tilde{T} L}. \end{aligned} \tag{2.4.43}$$

The beam current before the target is then relabeled as "I" for incoming and the beam current after target as "U" for the unreacted beam,

$$U_{\text{target}} = I_{\text{target}} e^{-\sigma_{\text{Interaction}} T}. \tag{2.4.44}$$

Where the full number of scattering centres in the target is given by,

$$T = \tilde{T} L. \tag{2.4.45}$$

An efficiency correction is applied using data from the empty target runs to account for possible losses in the Data AcQuisition (DAQ) and detector acceptances,

$$U_{\text{target}} = \left(I_{\text{target}} e^{-\sigma_{\text{Interaction}} T} \right) \frac{U_{\text{empty}}}{I_{\text{empty}}}. \tag{2.4.46}$$

Rearranging equation 2.4.46 gives the formula for interaction cross section,

$$\sigma_{\text{Interaction}} = -\frac{1}{T} ln \left(\frac{I_{\text{empty}}}{U_{\text{empty}}} \frac{U_{\text{Target}}}{I_{\text{Target}}} \right). \tag{2.4.47}$$

The uncertainty for this measurement can be calculated using error propagation for each variable,

$$\Delta\sigma_{\text{Interacation}} = \frac{1}{T} \left(\left(\frac{\Delta I_{\text{empty}}}{I_{\text{empty}}} \right)^2 + \left(\frac{\Delta I_{\text{target}}}{I_{\text{target}}} \right)^2 + \left(\frac{\Delta U_{\text{empty}}}{U_{\text{empty}}} \right)^2 + \left(\frac{\Delta U_{\text{target}}}{U_{\text{target}}} \right)^2 \right)^{\frac{1}{2}}. \tag{2.4.48}$$

2.4.1 Thick Target Formalism

For a thick target, corrections to the cross sections can be applied. When a projectile enters the target and undergoes a reaction a residual nuclei is produced. This residual then has the possibility to react again within the target.

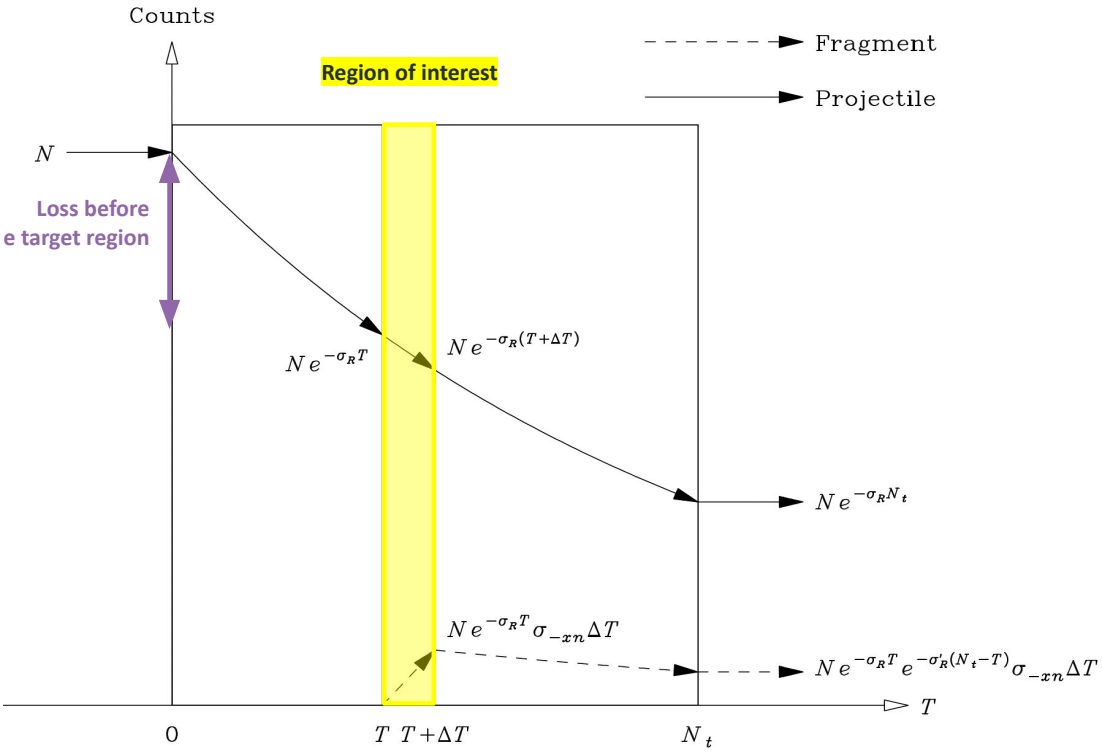

Figure 2.4: Quantitative description of reaction loss in target due to secondary reaction of the residual nuclei. Figure taken from [20].

Figure 2.4 shows that the initial projectile count at position T in the target is,

$$N(T) = Ne^{-\sigma_R T} \tag{2.4.49}$$

Here N is the total number of incoming projectiles and σ_{R} is the total reaction cross section. This equation is equivalent to 2.4.44, however uses symbols from the author of [20]. If no other reaction was to occur then one simply integrates over the entire thickness of the target giving the same solution as equation 2.4.43. However if secondary reactions are considered the differential cross section becomes,

$$\frac{dN'(T)}{dT} = Ne^{-\sigma_R N_t}e^{-(\sigma_R-\sigma'_R)T}\sigma_{-xn}. \tag{2.4.50}$$

Here σ'_R is the total reaction cross section for the residual nuclei from the first reaction and σ_{-xn} is the cross section for a secondary reaction.

Integrating equation 2.4.50 gives,

$$\begin{aligned}
\int_0^T dN'(T) &= \int_0^{N_t} N e^{-\sigma_R N_t} e^{-(\sigma_R - \sigma'_R)T} \sigma_{-xn} dT \\
N'(N_t) &= N\sigma_{-xn} e^{-\sigma_R N_t} \int_0^{N_t} e^{-(\sigma_R - \sigma'_R)T} dT \\
N'(N_t) &= N\sigma_{-xn} e^{-\sigma_R N_t} \left[\frac{e^{-(\sigma_R - \sigma'_R)T}}{-(\sigma_R - \sigma'_R)} \right]_0^{N_t} \\
N'(N_t) &= N\sigma_{-xn} e^{-\sigma_R N_t} \left(\frac{e^{-(\sigma_R - \sigma'_R)N_t} - 1}{-(\sigma_R - \sigma'_R)} \right)
\end{aligned} \tag{2.4.51}$$

Equation 2.4.51 can be rearranged to give the cross section for a nucleon to be knocked out,

$$\sigma_{-xn} = \frac{N'(N_t)}{N} \left(\frac{(\sigma_R - \sigma'_R)}{e^{-\sigma'_R N_t} - e^{-\sigma_R N_t}} \right) \tag{2.4.52}$$

The total reaction cross section between the projectiles and residual differs only very slightly, unless halo nuclei or other highly unstable nuclei are considered. Therefore, the approximation $\sigma_R \to \sigma'(R)$ can be applied. This is done by using L'Hôpital's rule to equation 2.4.52,

$$\begin{aligned}
\lim_{\sigma_R \to \sigma'_R} \sigma_{-xn} &= \frac{N'(N_t)}{N} \lim_{\sigma_R \to \sigma'_R} \left(\frac{(\sigma_R - \sigma'_R)}{e^{-\sigma'_R N_t} - e^{-\sigma_R N_t}} \right) \\
\sigma_{-xn} &= \frac{N'(N_t)}{N} \lim_{\sigma_R \to \sigma'(R)} \left(\frac{\frac{d}{d\sigma_R}(\sigma_R - \sigma'_R)}{\frac{d}{d\sigma_R}\left(e^{-\sigma'_R N_t} - e^{-\sigma_R N_t}\right)} \right) \\
\sigma_{-xn} &= \frac{N'(N_t)}{N} \lim_{\sigma_R \to \sigma'(R)} \frac{1}{N_t e^{-\sigma_R N_t}} \\
\sigma_{-xn} &= \frac{N'(N_t)}{N} \frac{1}{N_t e^{-\sigma'_R N_t}}.
\end{aligned} \tag{2.4.53}$$

Therefore, the one proton removal cross section can be calculated using,

$$\sigma_{-1p} = \frac{1}{N_t} \cdot \frac{N_{-1p}}{N_{\text{unreacted}}}. \tag{2.4.54}$$

Here N_{-1p} is the number of nuclei that lose exactly one proton. This is then generalised, such that a cross section for any interaction can be calculated using,

$$\sigma_{\text{target}} = \frac{1}{\epsilon T_{\text{target}}} \cdot \frac{R_{\text{reaction}}}{I_{target}}. \tag{2.4.55}$$

Here σ_{target} represents the cross section for a reaction channel, ϵ the efficient correction for any loss of the fragments, R_{reaction} and I_{target} the counted number of reaction products and the number of incoming nuclei of interest respectively. The number of scattering centres within the target is given by T_{target}.

Chapter 3

Experimental Setup

The s467 experiment [21] was performed during February 2020 at GSI in Darmstadt, Germany using the R^3B setup. The aim of the experiment was two-fold: testing the roles of three-body interactions of nucleons in neutron-rich isotopes and the detailed measurements of the quenching of the single-particle strength through reaction cross section measurements. The rest of this chapter will be dedicated to the setup used for the experiment.

3.1 Beam Production

A schematic of the GSI facility is shown in Figure 3.1. The ions of choice are first produced at the ion source [22] and accelerated by the UNIversal Linear ACcelerator (UNILAC) [23]. The beam is then fed into the SchwerIonenSynchrotoron (SIS18) [24], a 218 m long ring capable of accelerating ions up to 90% the speed of light. For the s467 experiment, ^{86}Kr was accelerated up to 580 AMeV at a beam intensity of 10^9 particles per spill with a spill length of 2 s. This beam energy is chosen to ensure that nucleons inside the nucleus behave as if they are nearly free during the reaction, which also falls within the energy regime where the impulse approximation remains valid.

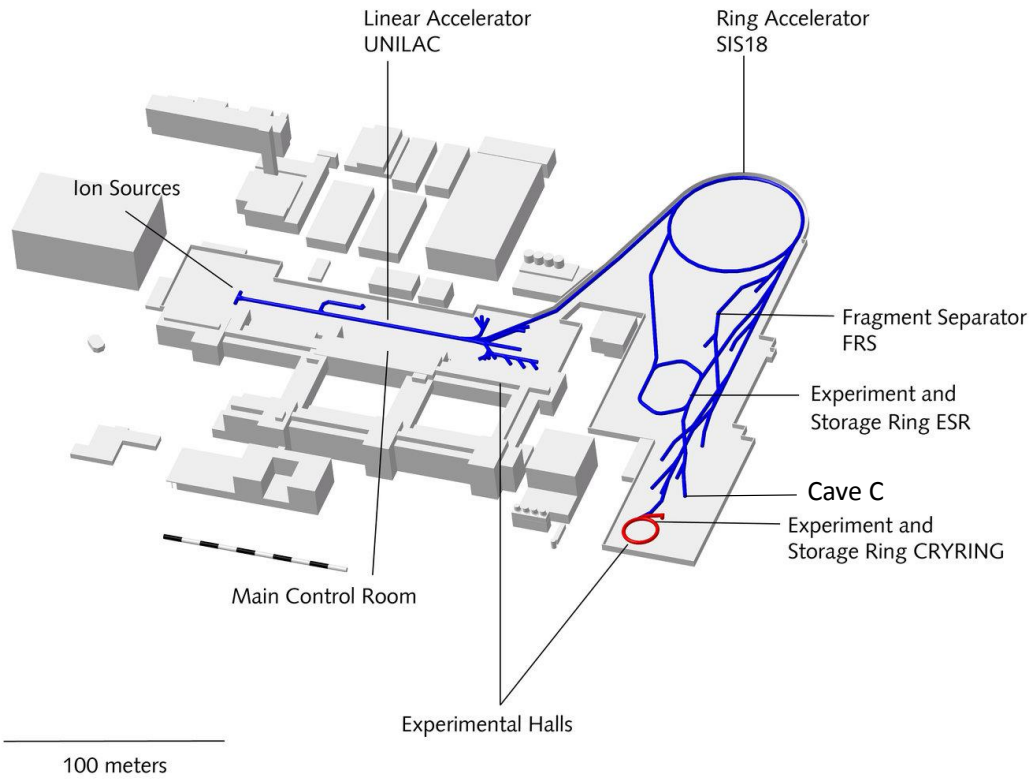

Figure 3.1: Overview of the GSI facility. The R^{3}B setup is located in Cave C.

3.2 Fragment Separator

Fully stripped ^{86}Kr is extracted from the SIS18 and fired at a ^{9}Be primary target with density 2500 mg/cm^2 located at the start of the FRagment Separator (FRS) [25]. This produces a cocktail beam which is passed through several magnets allowing for a selection using the Bρ-ΔE-Bρ method. Figure 3.2 shows an overview of the FRS.

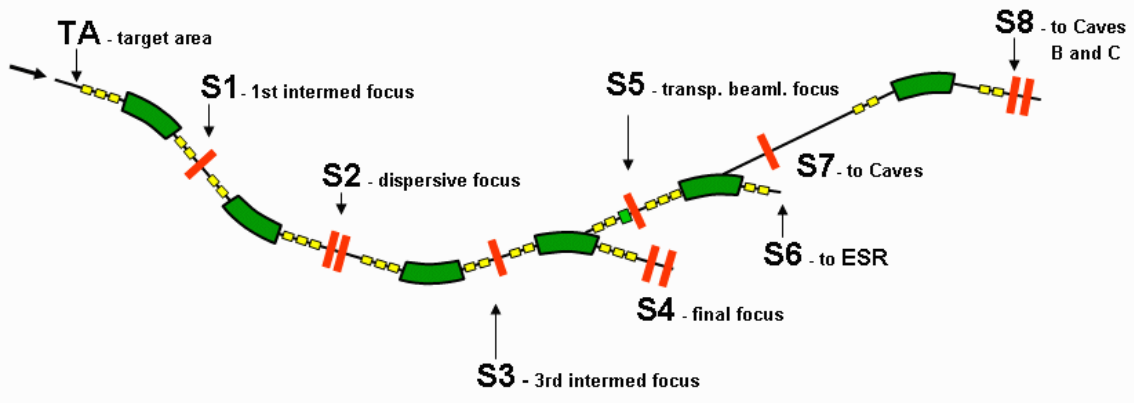

Figure 3.2: Schematic of the FRS beam line at GSI. TA is the primary target area where the ^{9}Be target is located. S2 and S8 are focal points where time of flight detectors can be installed.

These ions are then separated depending on their magnetic rigidity which can be related to the mass to charge value using,

$$\frac{\mathrm{A}}{\mathrm{Q}} = \frac{\mathrm{B}\rho}{\beta\gamma}. \tag{3.2.1}$$

Here a particle with mass A and charge Q travels through a uniform magnetic field B thus experiencing the Lorentz force. If the ion velocity β is also perpendicular to B the ion will display characteristics of centripetal force and move in a circular radius ρ. As the velocity is relativistic a Lorentz factor is included,

$$\gamma = \frac{1}{\sqrt{1-\beta^2}}. \tag{3.2.2}$$

These nuclei of interest are finally passed into Cave C where the R^{3}B setup is located.

3.2.1 S2 and S8 Focal Points

A 1 mm thick BC420 plastic scintillator with an active area of 200×50 mm^2 was installed at S2 for the Time-of-Flight (ToF) and the x-position dispersion measurement which is used for the momentum reconstruction event-by-event. The paddle has two Hamamatsu H10580 PMT attached at each end which can be seen in Figure 3.3. Each PMT has a timing resolution of 270 ps Full Width Half Maximum (FWHM) [26].

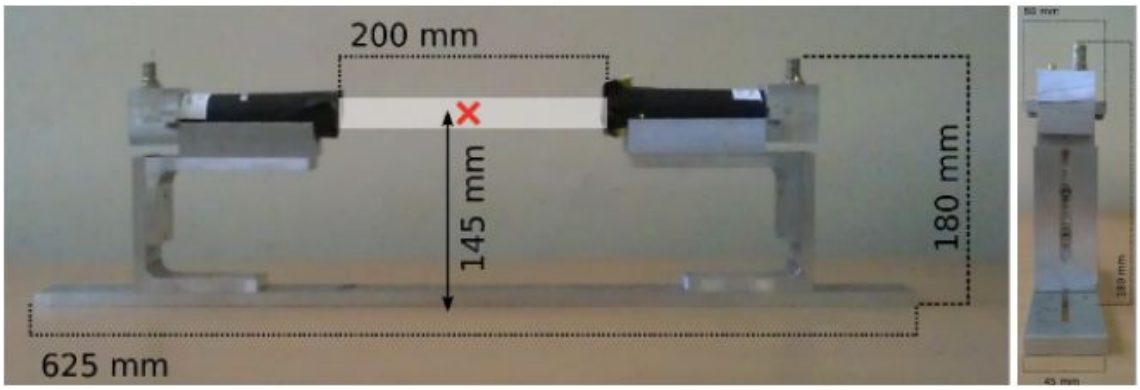

Figure 3.3: The S2 ToF detector front and side view with two PMTs connected at either side of the scintillator.

The x-position in S2 can be measured from the time difference between the two PMTs of the paddle. The position resolution however is rather poor and is not necessary for the final measurement. The ToF was then reconstructed with the flight path of S2–Cave C, where another plastic scintillator was installed. An additional EJ230 plastic scintillator located on a ladder as seen in Figure 3.4 was used.

Figure 3.4: The S8 scintillator ladder capable of holding up to 10 scintillating paddles of varying thickness and type.

The ladder is capable of holding up to 10 paddles. For this experiment a paddle 1.5 mm thick was used, which is read out by two Hamamatsu H6533 PMTs on either side of the paddle. The purpose of the detector is to increase the efficiency measurement due to losses from the high count rate at S2. The beam after S8 is then delivered to Cave C.

3.3 The R^{3}B Setup

Figure 3.5 provides an overview of the detectors used in Cave C. The detectors in the figure are color-coded based on what they are made from: purple represents plastic scintillating detectors, primarily used for time-of-flight measurements of ions; blue indicates multi-wire proportional chambers, utilized for ion position determination; green corresponds to gas drift chambers, designed for precise charge identification of ions; red denotes the calorimeter surrounding the target, responsible for reconstructing the kinematics of reaction products such as protons and gamma rays; and orange represents the large-acceptance magnet, essential for fragment separation in

mass determination. The magnet also ensures that no fragments impinge on NeuLAND, improving neutron detection efficiency. Additionally, the setup includes two plastic detectors, S2 and S8, used in the FRS.

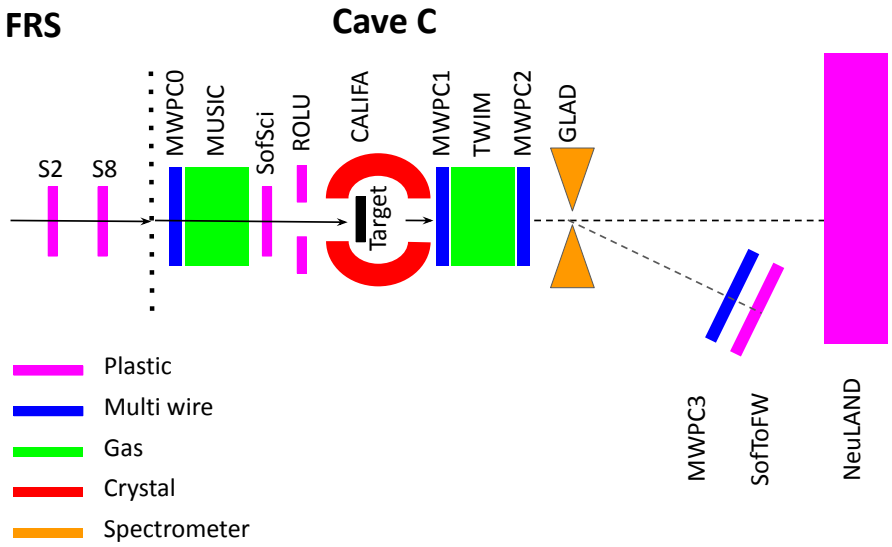

Figure 3.5: Detectors used in the analysis of the s467 experiment.

3.3.1 The SofSci Detector

The start detector constructed by the Studies On FIssion with ALADIN (SOFIA) collaboration called Sofia Scintilator (SofSci) is made from a plastic paddle of EJ-232 plastic with an active area of 50×32 mm^2 and 1 mm thick. This paddle is then connected to two Hamamatsu H6533 PMTs. The detector is read out using a specially produced VFTX [27] module. For this experiment the VFTX firmware is designed to allow a 7 ps timing resolution.

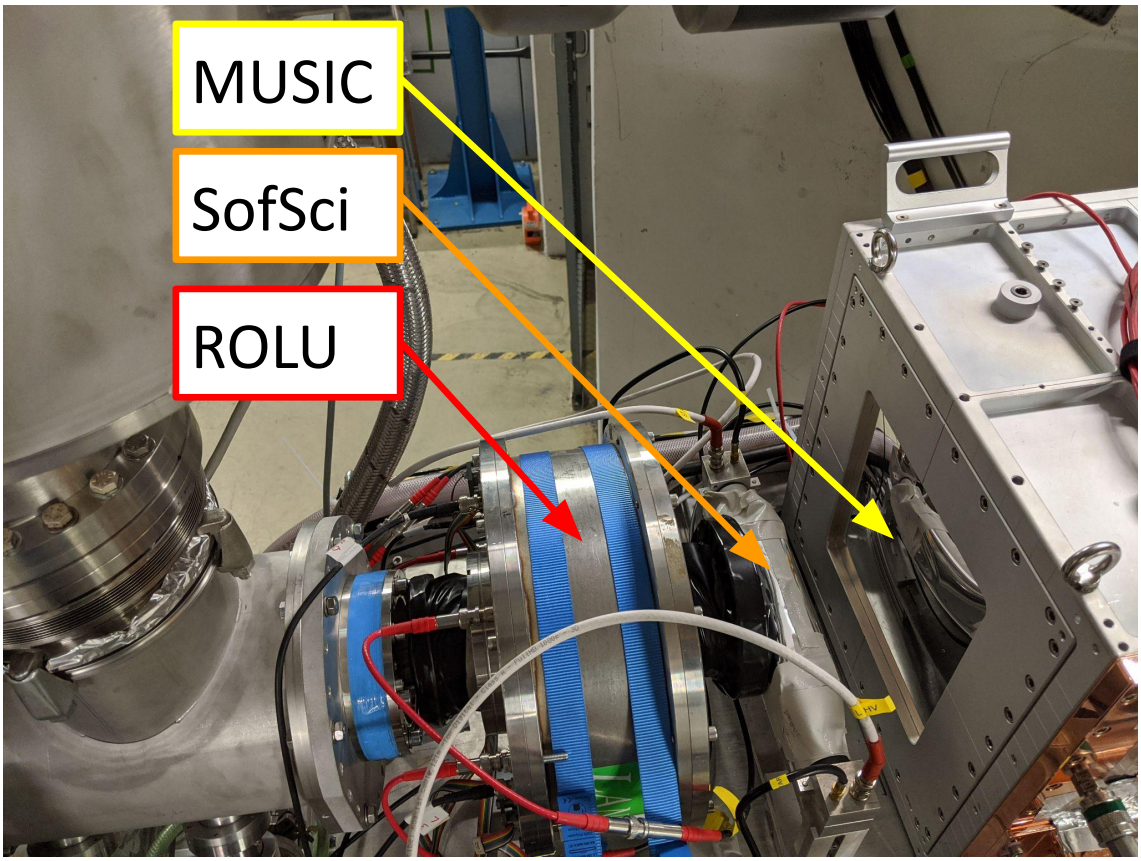

Figure 3.6: SofSci detector is marked by the orange arrow. It is located in between ROLU (red) and MUSIC (yellow).

Figure 3.6 shows SofSci is placed downstream of MUSIC and upstream of ROLU. The timing signal from SofSci is used in the calculation of the ToF for both incoming and outgoing ions.

3.3.2 ROLU Detector

Directly behind the SofSci detector is a veto detector called ROLU (Rechts Oben Links Unten). This is constructed out of four scintillating paddles mounted on IGUS drives [28] allowing them to be driven in and out of the beam. They are positioned such that only a square aperture of variable opening can be set in this experiment, the aperture is set to 20×20 mm^2. This ensures only particles close to the beam axis that hit the target area cause accepted triggers and the rest are vetoed. The start signal of the SofSci detector in anti-coincidence with ROLU define the minimum

bias good-beam trigger. Figure 3.6 shows the ROLU detector highlighted by a red arrow.

3.3.3 Gas Ionization Chamber Detectors

The MUlti Sampling Ionization Chamber (MUSIC) and TWIn-Music (TWIM) [29] are ionization chambers used to determine the energy and also the x angle of the ion that passes through them. MUSIC contains a mixture of 75% methane and 25% Argon with a surface area in the (x,y) plane of 200×200 mm^2 and a thickness of 400 mm. It contains 8 anodes within its volume. The beam causes ionization of the gas and the electrons/ions produced, induce a current at the anode and cathode. This signal is used to measure the charge of the ions through energy loss measurement and the x-angle trajectory through timing measurements at the subsequent anodes (which reflect the drift time in the detector). The MUSIC detector can be seen in Figure 3.6 indicated with a yellow arrow. The TWIM detector can be seen in Figure 3.7 placed in front of GLAD.

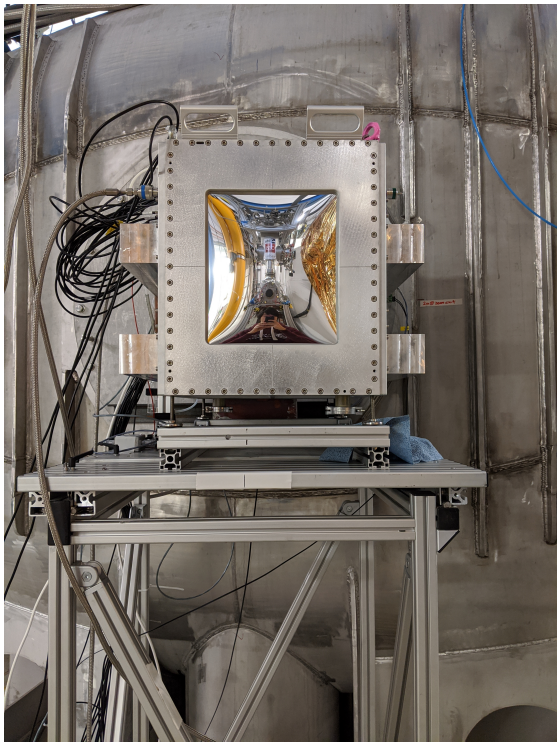

Figure 3.7: The TWIM detector placed between the exit of the target chamber and the entrance flange of GLAD.

3.3.4 The MWPC Detectors

The MWPC (Multi Wire Proportional Chamber) detectors are fundamental in the tracking of both the incoming beam and the residual nuclei after target. Four detectors were used MWPC0, MWPC1 and MWPC2 were placed before GLAD and MWPC3 after GLAD as shown in Figure 3.5. These detectors consist of a mesh made of Aluminium evaporated on mylar foil for MWPC0 , MWPC1 and MWPC3. For MWPC2 Gold is evaporated on mylar foil. Each MWPC contains a gas mixture of 84% Argon and 16% carbon dioxide at a temperature of 300 K and a pressure of 1 atm. When a heavy ion passes through the detector it ionises the gas and the electron/ions produced cause a current to flow. This results in charge being measured on each pad and an (x,y) position being recorded. MWPC0 and MWPC1 have an active surface area of 200×200 mm^2 and consist of 64×64 pads in MWPC0 and 64 vertical and 40 horizontal in MWPC1 and MWPC2. MWPC3 has

288 vertical pads and 120 horizontal pads. MWPC0 allows for an absolute position measurement of the beam in the xy plane when entering the cave. Using all three of these detectors before GLAD it is possible to perform a fitting procedure using unreacted beam particles to calibrate the x and y position offsets of each detector. Once calibrated tracking of the ions can be performed before and after the target. MWPC3 is then used to measure the position of the fragment after GLAD so that the Bρ of the fragment can be reconstructed. A dismounted MWPC1 can be seen in Figure 3.8.

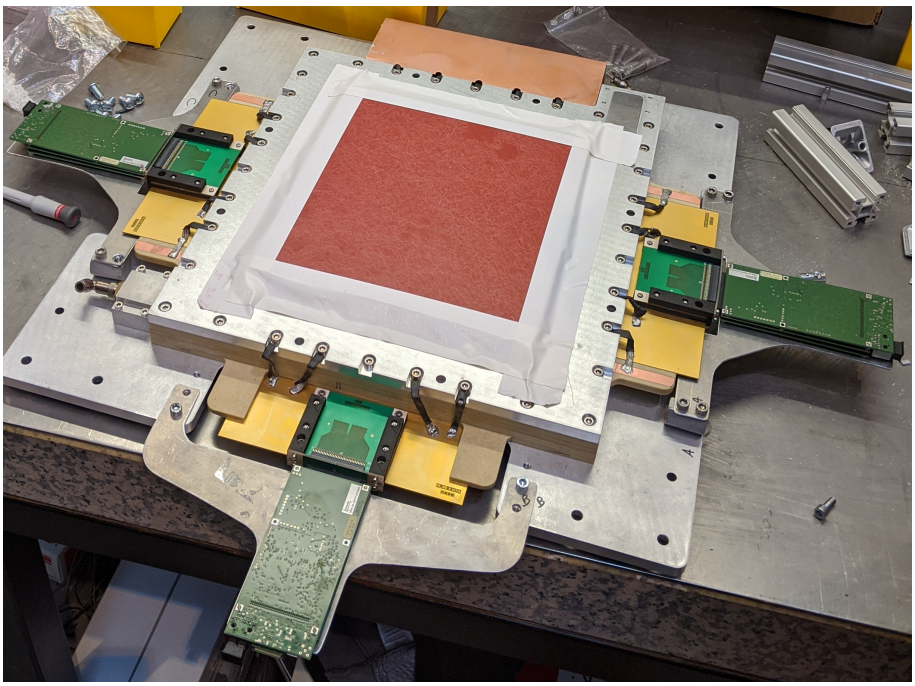

Figure 3.8: MWPC1 detector before mounting.

3.3.5 The CALIFA Detector

CALIFA is the CALorimeter for In Flight detection of γ-rays and high energy charged pArticles [30]. The array has been optimised for the joint measurement of both Lorentz boosted protons and Doppler boosted gammas. The detector is placed directly around the target chamber. During the s467 experiment CALIFA contained 1204 highly segmented CsI(Tl) scintillating crystals split into two main parts, the barrel and the end cap. The nominal angular coverage of the barrel covers

between 43 and 140 degrees and the cap 19 to 43 degrees with respect to the beam axis [31, 32]. However, for the s467 experiment CALIFA was only partially filled with angular coverage of 19 to 43 degrees in the cap and 43 to 84 degrees in the barrel. During the experiment the Internal Phoswich (IPhos) region located in the cap was 35% complete which can be seen in Figure 3.9.

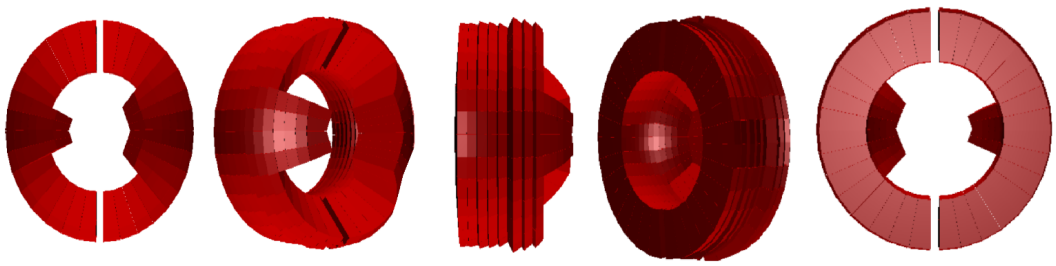

Figure 3.9: Simulation geometry of the CALIFA detector for the s467 experiment shown at different viewing angles, here the IPhos is only 35% complete.

The CsI(Tl) crystals are wrapped in reflective foil and connected to two Hamamatsu S8664-1020 Avalanche Photo Diode (APD) with an active area of 10×10 mm^2 in series with one ceramic housing. The APD's are then connected to duel range pre-amplifiers allowing for selection of either: gamma mode, proton mode or both. The crystal shapes were designed using dedicated simulations and have complex geometries. The length of the crystals are between 18–22 cm. The Wixhausen half of CALIFA can be seen in Figure 3.10.

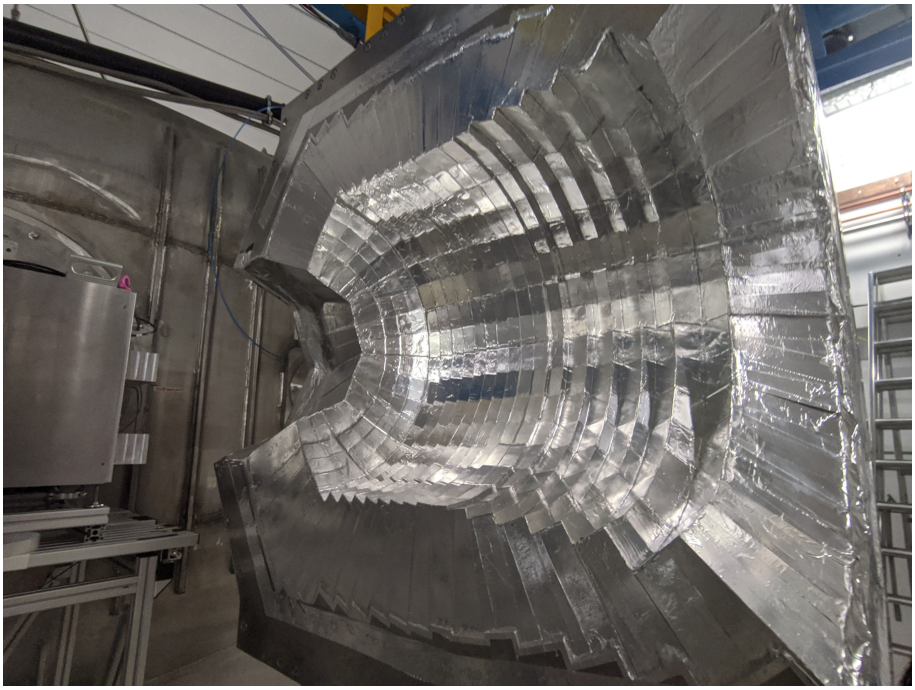

Figure 3.10: The CALIFA detector is defined in two sections which are named after the closest towns they are directed at these are: Wixhausen (right with respect to the beam direction) and Messel (left with respect to the beam direction). Here the Wixhausen side is seen with reflective Aluminium foil glued externally acting as an additional shield for noise, fields and ambient light.

3.3.6 GLAD

The Giant Large Area Dipole (GLAD) [33, 34] is a zero-degree superconducting dipole magnet that provides a large angular acceptance of ±80 mrad separating fragments and allowing for the detection of neutrons produced in nuclear reactions. It comes with a maximum bending angle of 40 degrees which allows for a momentum resolution $\frac{\Delta p}{p} \approx 10^{-3}$, providing a much improved isotropic separation of its predecessor ALADIN [35]. During the experiment two beam settings were used one neutron rich setting (^{50}Ca setting) and one proton rich setting (^{38}Ca setting).
Table 3.1 shows the current required to bend the main fragment of interest 18 degrees. Figure 3.11 shows the exit of GLAD.

Beam setting	^{38}Ca	^{50}Ca
Beam energy [AMeV]	580	580
GLAD current [A]	1349	2014

Table 3.1: GLAD current for each beam setting of the s467 experiment.

.

Figure 3.11: GLAD during the preparation of the s467 experimental campaign.

3.3.7 SofToFW Detector

The Sofia Time Of Flight Wall (SofToFW) [36] is a plastic scintillating detector built up of 28 EJ228 vertical bars read out on both sides by two PMTs with an active area of 900×600 mm^2 and 5 mm thick. The inner 19 pairs are read out by Hamamatsu H6533 and the outer 9 are read out by Hamamatsu H10580. The time difference between the two PMTs of the same bar can be used to calculate the vertical position within that bar and from which numbered paddle is hit a rough horizontal position can be estimated. The timing information is calculated from the average time of the two PMTs of the hit paddle and used in the ToF calculation between the start detector and the SofToFW. From this an absolute ToF measurement of

the fragments is obtained. The timing resolution for ToF is 40 ps FWHM and a position resolution in Y of 3 mm FWHM. The detector can be seen in Figure 3.12.

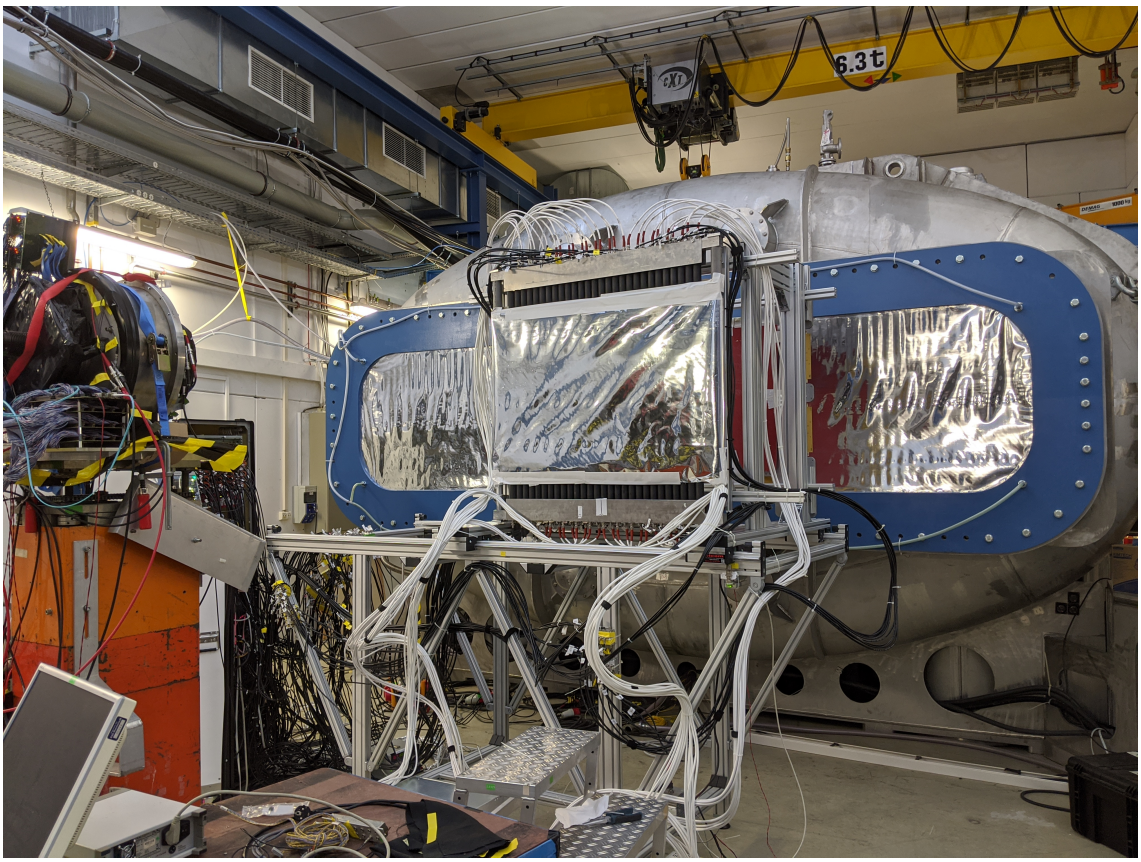

Figure 3.12: SofToFW detector located behind GLAD and directly behind MWPC3.

3.3.8 NeuLAND

NeuLAND (Neu Large-Area Neutron Detectors) [37] is the new neutron detector currently used in the R^{3}B experiments. At the time of the s467 experiment the NeuLAND detector consisted of 8 double planes of plastic scintillating bars with each plane containing 50 bars. The organic scintillator materials used for bars are RP-408 and EJ200. Each bar has a volume 5×5×250 cm^3 given a total active area of 250×250 cm^2 and at the time of the experiment a total thickness of 160 cm. At the end of each bar is a Hamamatsu R8619 PMT. This high granularity allows for high-resolution measurements and a large multi-neutron detection efficiency.

3.3.9 Trigger Logic

The TRigger LOgic (TRLO) consists of many different trigger combinations which form Trigger PATterns (TPATs). Trigger decisions are programmed using a digital module called VULOM [38].

log2(Tpat)	Name	SofSci and !ROLU	CALIFA	NeuLAND	S2	Pulser
0	Min Bias	•				
1	CALIFA	•	•			
2	NeuLAND	•		•		
3	CALIFA and NeuLAND	•	•	•		
4	S2				•	
8	CALIFA off-spill		×			
9	NeuLAND off-spill			×		
15	Pulser					×

Table 3.2: Table showing the trigger logic used for the s467 experiment where circles denote the detector used for on-spill triggers and crosses for off-spill triggers.

From Table 3.2 one sees both the name and number assigned to the trigger decision for onspill and offspill triggers. No downscale factors were used for the s467 experiment due to low beam rates. Here !ROLU corresponds to the anit-coincidence signal from ROLU such that no hit is registered in the veto detector. This means that only ions passing through the reaction target will generate triggers.

3.3.10 Data Acquisition

During the experiment DAQ is performed using both the Multi-Branch System (MBS) [39] developed at GSI and by Drasi [40]. The decision to accept an event comes from the TRLO and then if a detector system is firing too frequently it can be down scaled to avoid over saturation. If the trigger decision is satisfied, all systems that triggered send data to the main time orderer. Within this data is a timestamp which is compared to a main clock. This data is then time stitched using a stitching window of 4 μs this means that data from a detector $\pm$ 2 μs of a given timestamp will be merged. The output file is then saved in List Mode Data (LMD) format which can be further processed into a ROOT [41] file using software called Unpack

& Check Every Single Bit (UCESB) [42].

3.3.11 Data Analysis

For the analysis, the R3BRoot [43, 44] software package was used. This is a software package based on ROOT [41] and FairRoot [45]. Figure 3.13 shows a flow chart describing the data processing. Detector data can either be taken from an LMD file or directly from UCESB stream. This data is converted into map level, this consists of the basic outputs of detector electronics, such as Analogue to Digital Converter (ADC) units or Time to Digital Converter (TDC) units. From here the data is calibrated using a set of calibration parameters and macros, such as gain matches or pedestal subtraction. Then a final task called "Cal2Hit" or "Cal2Cluster" is applied. Data can then be analysed.

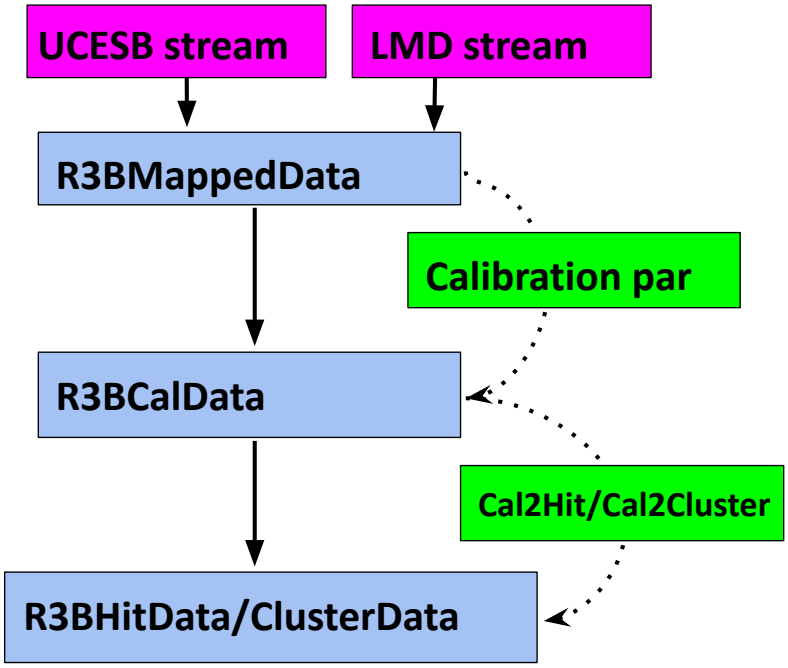

Figure 3.13: Flow diagram of typical R3BRoot data analysis.

Chapter 4

Calibrations

This chapter will present an overview of some of the detector calibration methods. The first section describes the calibrations for ToF detectors and the A/Q stability during the experiment. The second section will show MUSIC and TWIM calibrations. The third will cover the calibration of the MWPC detectors. And the final section will deal with the CALIFA calibration.

4.1 Time of Flight Calibrations

During the experiment the FRS was tuned to transmit as many isotopes as possible using a limited momentum space acceptance. A standard Bρ-ΔE-ToF Particle IDentification (PID) is used to find the ion of interest. The plastic scintillators S2, S8 and SofSci were used for the ToF calculation. As these systems do not use the same clock there is a timing offset between the electronics. An accurate value of the flight path length must also be calculated. Starting from the equation for velocity β,

$$\beta c = \frac{\mathrm{L}}{\mathrm{ToF}}. \tag{4.1.1}$$

Where L is the path length and ToF the Time of Flight. The timing offset, T_{offset} can then be found using,

$$\Delta t = \mathrm{ToF} + T_{offset}. \tag{4.1.2}$$

Substituting the ToF with equation 4.1.1 and then multiplying by β gives,

$$\beta\Delta t = \frac{L}{c} + \beta T_{offset}. \tag{4.1.3}$$

To calculate these offset values LISE++ simulations [46] were performed for different primary beam settings listed in Table 4.1.

Beam energy [AMeV]	580	580	450
Target	Non	^{9}Be	^{9}Be
β [c]	0.78124	0.74946	0.72867
Bρ [Tm]	9.28082	8.39528	7.88889

Table 4.1: Magnetic rigidities and velocities calculated using LISE++ for three different calibration runs. These values are used to calibrate path lengths and timing offsets for the s467 experiment.

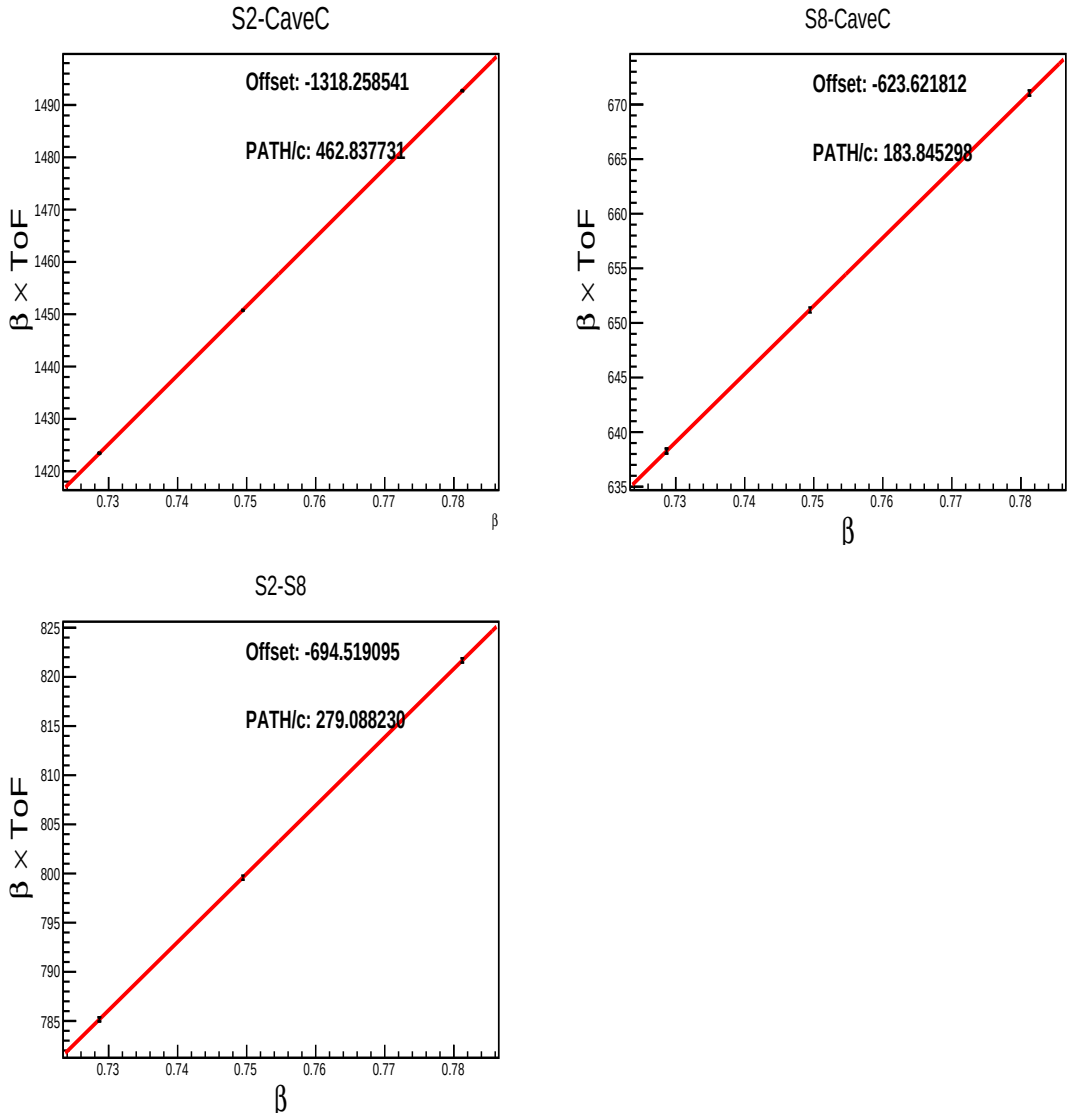

Figure 4.1: The top left plot represents S2 to Cave C, the top right shows S8 to Cave C, and the bottom left depicts S2 to S8. The three scintillator pair combinations and their corresponding timing offsets and path lengths are calculated from a linear fit using equation 4.1.3.

Equation 4.1.3 is then the fit function of these plots in Figure 4.1. The calculated gradient of the line is the timing offset and the y intercept is the ion path length. The stability of the FRS A/Q identification for each run setting can be seen in Figure 4.2.

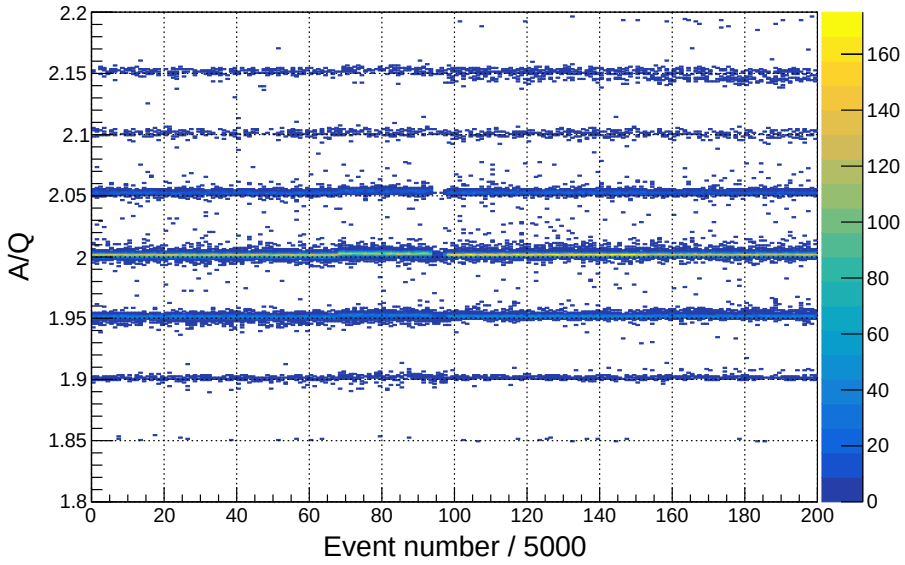

(a) ^{38}Ca setting, empty target runs.

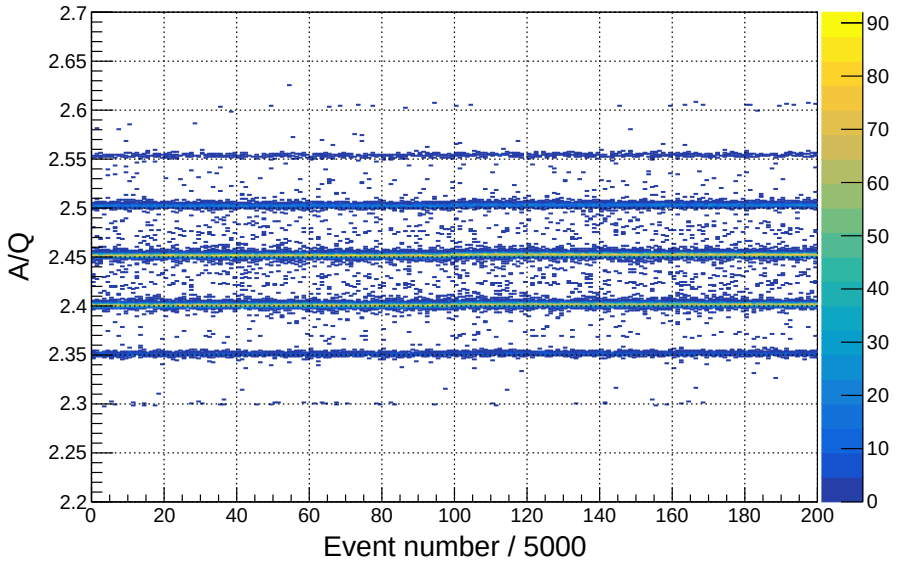

(b) ^{50}Ca setting, empty target runs.

Figure 4.2: FRS A/Q identification stability over time for empty target runs for Z=20. Here the horizontal axis corresponds to event number scaled by 5000. For plot (a) and (b) this corresponds to roughly 3 hours of beam time for each respective setting.

As can be seen in Figure 4.2 the A/Q measurement is consistent over the whole

experiment.

	^{39}Ca	^{40}Ca	^{41}Ca	^{48}Ca	^{49}Ca	^{50}Ca
$\mu_{\mathrm{A/Q}}$	1.951	2.002	2.053	2.401	2.452	2.503
$\sigma_{\mathrm{A/Q}}$ $[\times 10^{-3}]$	1.276	1.272	1.287	1.566	1.578	1.606
$\frac{\sigma_{\mathrm{A/Q}}}{\mu_{A/Q}}$ $[\times 10^{-4}]$	6.540	6.354	6.269	6.522	6.436	6.416

Table 4.2: FRS mass resolution values for abundant Ca isotopes . The standard deviation, $\mu_{\mathrm{A/Q}}$ is calculated from a gauss fit from the slice at the mean for each isotope. The resolution is then calculated by taking the ratio of the standard deviation and the mean, $\frac{\sigma_{\mathrm{A/Q}}}{\mu_{A/Q}}$.

Table 4.2 shows the mass resolution for Ca isotopes is around 0.06% which is more than sufficient for the scope of this study.

4.2 MUSIC and TWIM

The stability of the energy signals from MUSIC and TWIM (which are used for the charge identification) are sensitive to several factors such as temperature fluctuations and gas pressure and can cause gain drifts over time. To check and correct for this the energy values are plotted versus the event number as shown in Figure 4.3. A fit function is applied to the mean value per bin and from the fit a mean for the run is calculated. Figure 4.4 shows these mean gains for each run for anode 0 in both detectors. These values can then be corrected by applying a gain factor such that the mean drift is constant for all runs per setting. This procedure is then repeated for each anode in both MUSIC and TWIM.

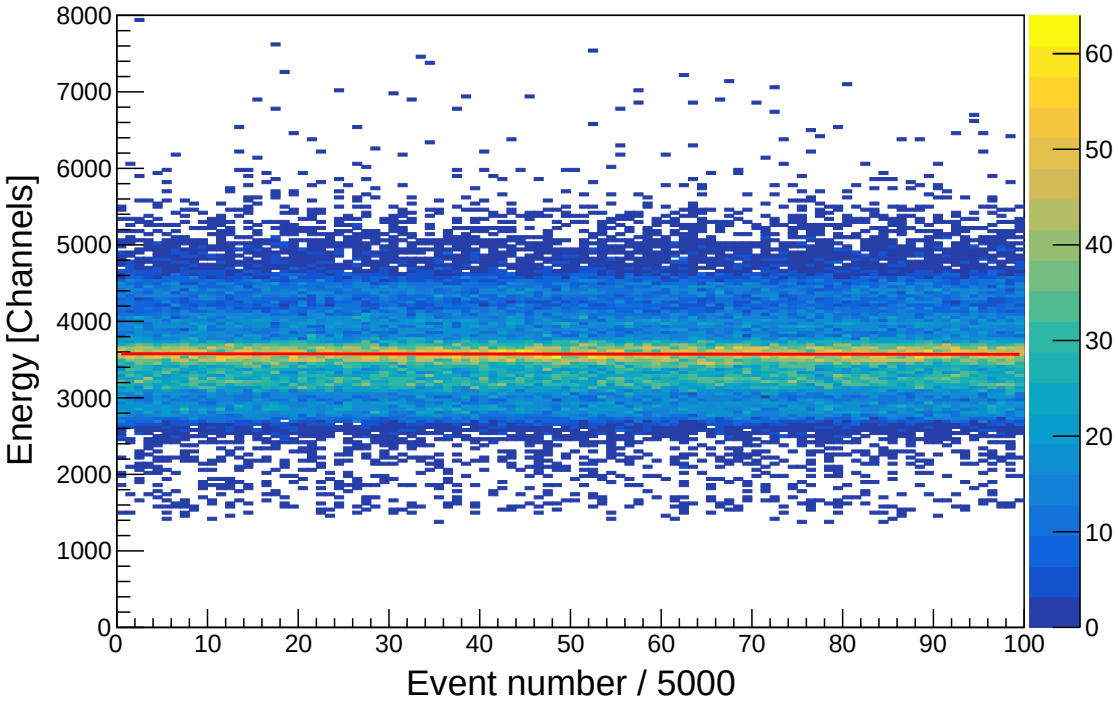

(a) MUSIC empty target ^{38}Ca setting run263 anode 0.

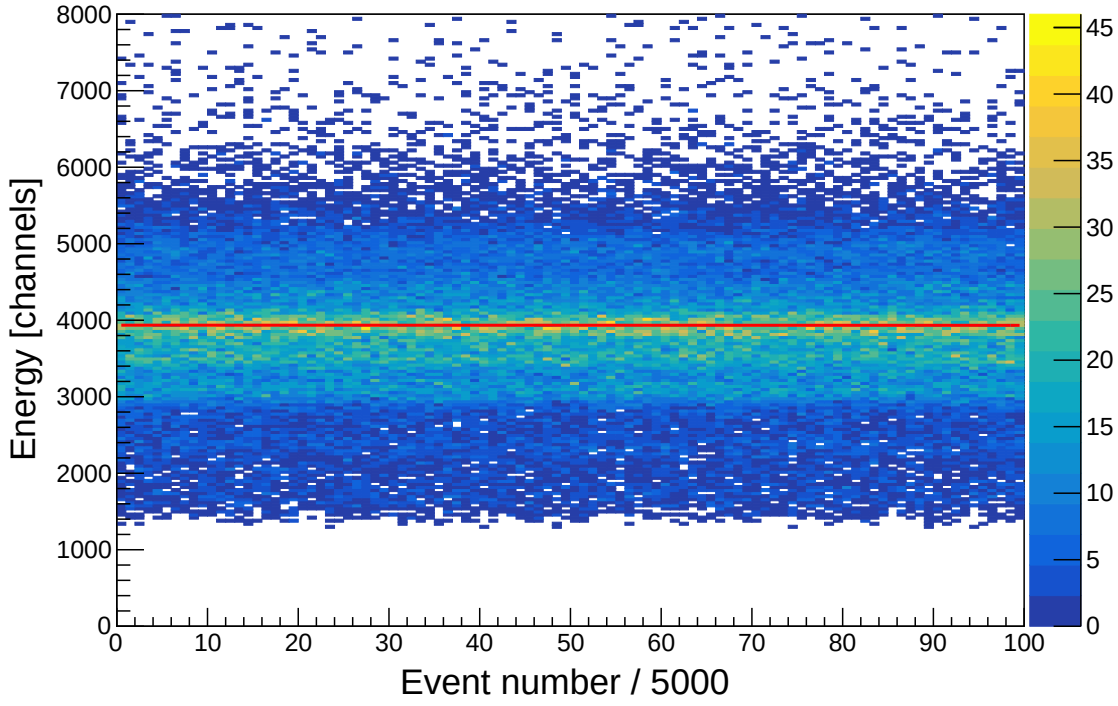

(b) TWIM empty target ^{38}Ca setting run263 anode 0.

Figure 4.3: Energy plotted against event number for anode 0 in both MUSIC (a) and TWIM (b) for run 263. Here only a single run is shown which corresponds to one hour of beam time.

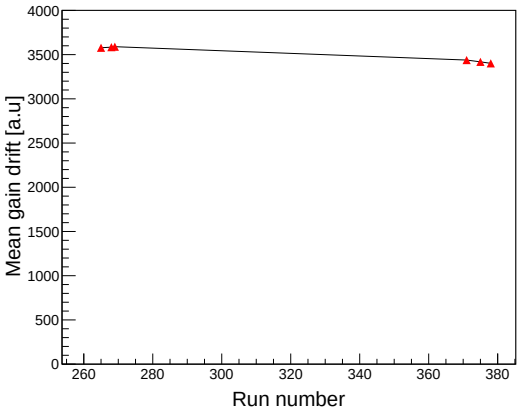

(a) MUSIC empty target, ^{38}Ca setting.

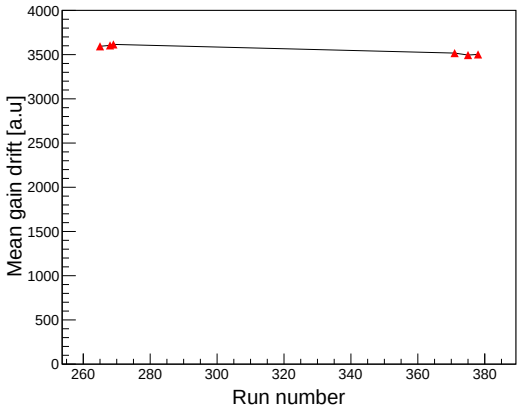

(b) TWIM empty target, ^{38}Ca setting.

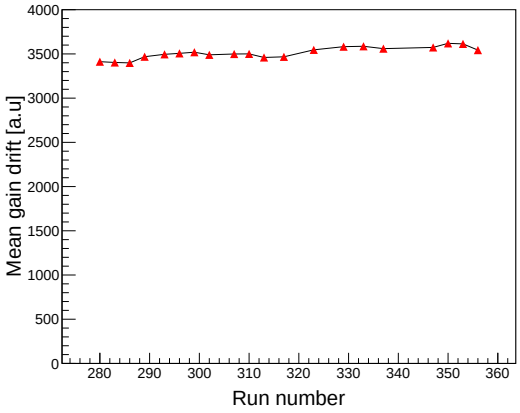

(c) MUSIC empty target, ^{50}Ca setting.

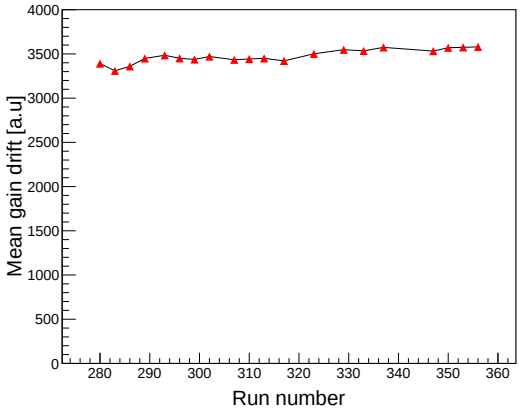

(d) TWIM empty target, ^{50}Ca setting.

Figure 4.4: Figure (a) and (c) show the mean gain drift as a function of run number for the empty target setting for ^{38}Ca and ^{50}Ca for the MUSIC detector. Figure (b) and (d) show the same but for the TWIM detector.

4.3 MWPC Calibration

The alignment of the detectors was initially assessed by generating position correlations between MWPC1 and MWPC2 (the two closest detectors). Figure 4.5 shows the uncalibrated position correlation between MWPC1 and MWPC2 in the x axis (a) and the y axis (b).

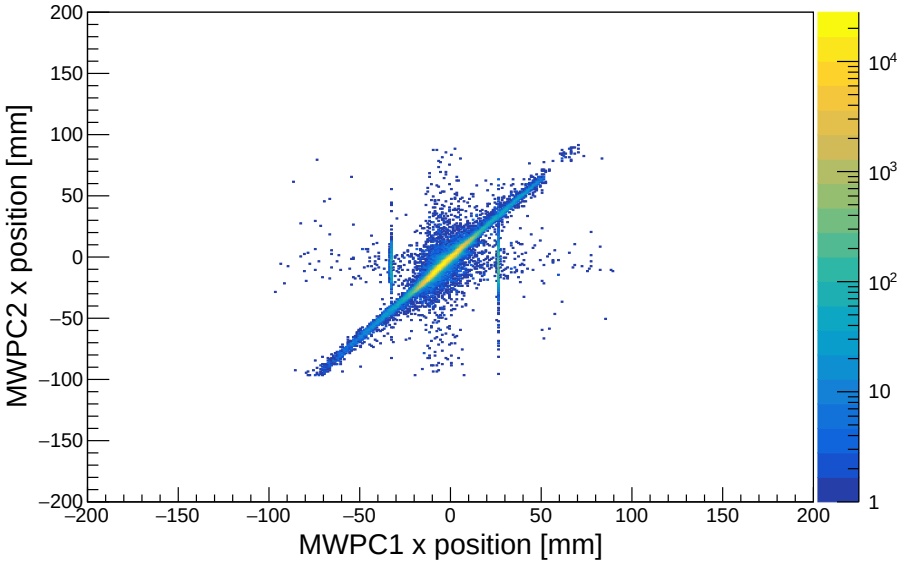

(a) Uncalibrated x position correlation between MWPC1 and MWPC2.

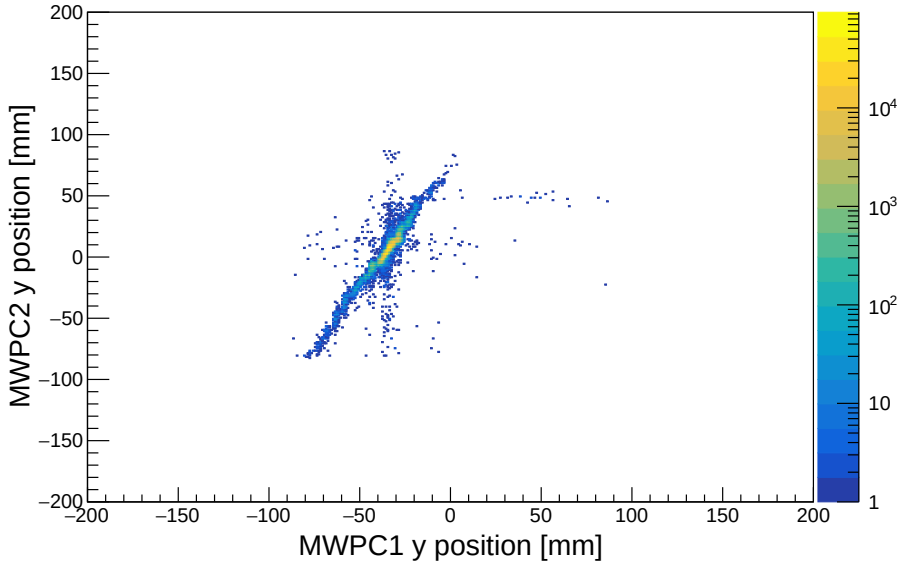

(b) Uncalibrated y position correlation between MWPC1 and MWPC2.

Figure 4.5: Empty target position correlation plots between MWPC1 and MWPC2. Plot (a) shows the x correlation and plot (b) shows the y correlation.

Plot (a) shows uncorrelated events coming from MWPC1 and in plot (b) a large position offset coming from MWPC1. The non correlating events were investigated by checking the pedestals of each detector.

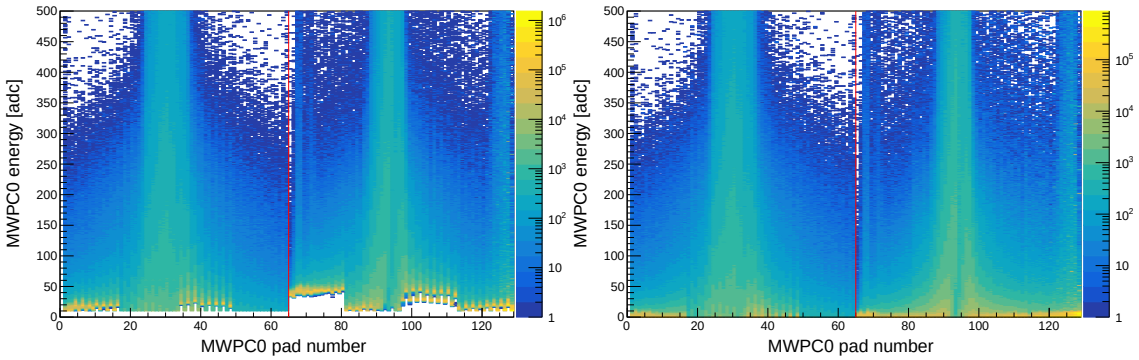

(a) MWPC0 mapped level pedestal.

(b) MWPC0 calibrated level pedestal.

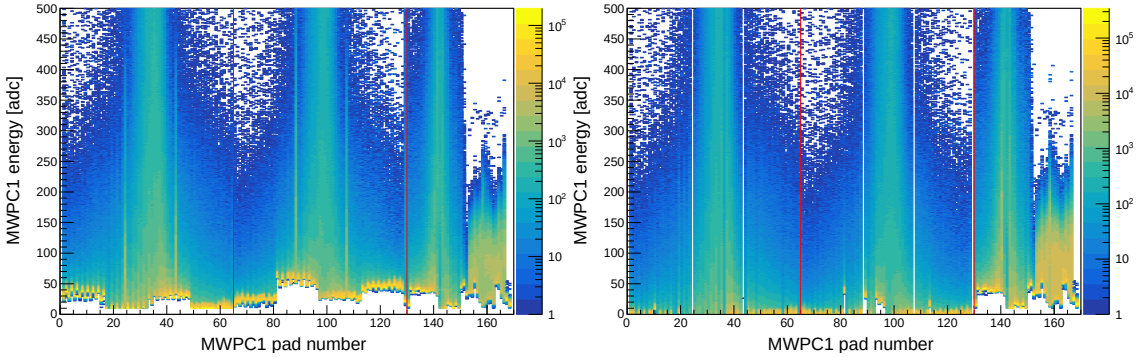

(c) MWPC1 mapped level pedestal.

(d) MWPC1 calibrated level pedestal.

Figure 4.6: Plots (a) and (c) show pedestals before calibration and (b) and (d) after calibration of the energy signals in MWPC0 and MWPC1.

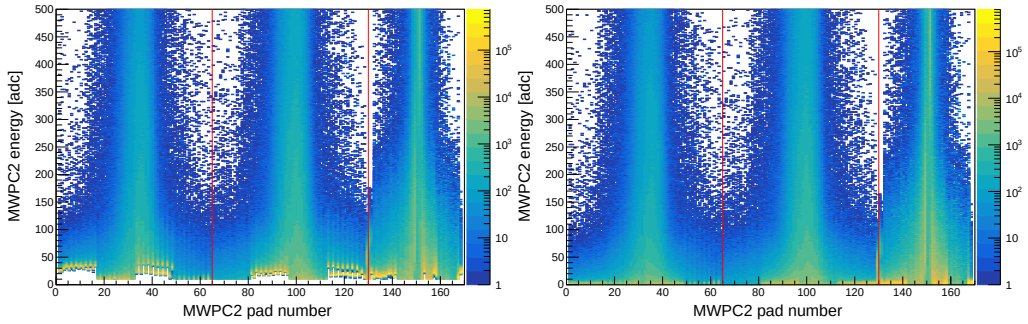

(a) MWPC2 mapped level pedestal. (b) MWPC2 calibrated level pedestal.

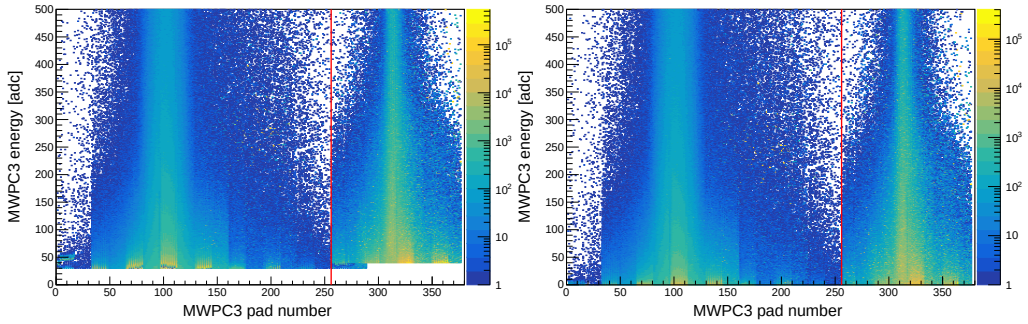

(c) MWPC3 mapped level pedestal. (d) MWPC3 calibrated level pedestal.

Figure 4.7: Plots (a) and (c) show pedestals before calibration and (b) and (d) after calibration of the energy signals in MWPC2 and MWPC3.

From Figure 4.6 it is seen that in MWPC1 four pads are overactive, causing an issue with the position reconstruction. These pads are removed and a baseline subtraction is applied to all pedestals where the peak of the noise in each pad is found and then subtracted. For the alignment, tracks of unreacted beam for the empty target runs are used and the two furthest detectors (MWPC0 and MWPC2) are assumed to have absolute position taken from their measured position value. Both the xz and yz projection for MWPC1 are calculated and subtracted from the measured values and mean offsets for both x and y are calculated. From Table 4.3 it is seen that the change in x position offset for Ca isotopes varies less than 0.2 mm and for y less than 0.6 mm from the median value.

	^{38}Ca	^{39}Ca	^{40}Ca	^{41}Ca	^{42}Ca	^{43}Ca	^{47}Ca	^{48}Ca	^{49}Ca	^{50}Ca	^{51}Ca
x_{offset} [mm]	-1.0	-1.0	-0.9	-0.9	-1.0	-1.0	-1.1	-1.1	-1.1	-1.0	-1.0
y_{offset} [mm]	-37.2	-37.4	-37.4	-37.4	-37.9	-37.8	-37.2	-37.4	-37.5	-37.6	-37.7

Table 4.3: Mean values from Gaussian fits applied to the difference between projected and measured MWPC position in both x and y.

The larger variation in the y offset is due to the poorer resolution coming from the technical specification of the MWPC's. As the variation in the offsets across the Ca isotopic chain is less than that of the position resolution of the detectors, a simple average offset value for both x and y is taken. Figure 4.8 shows the x and y position correlation plots after calibration centralised at the origin.

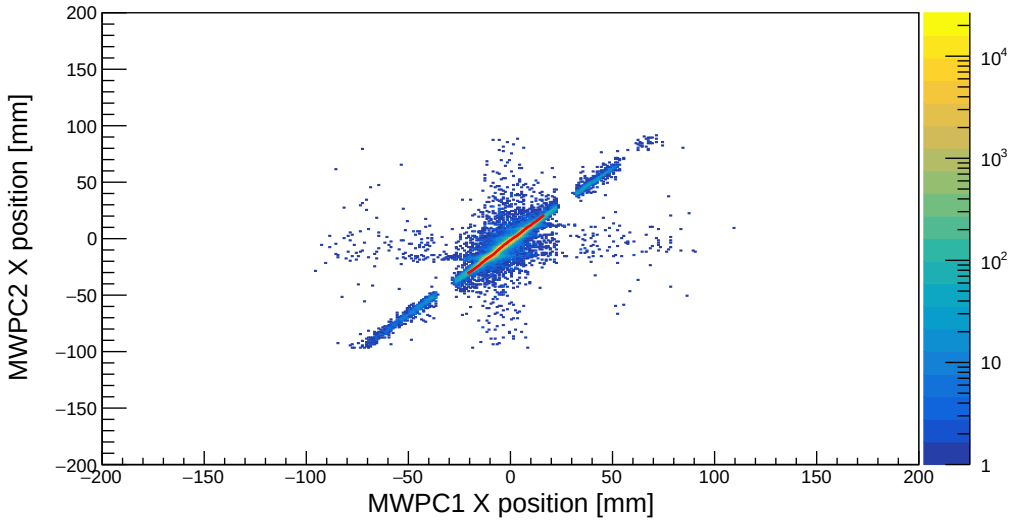

(a) x position correlation between MWPC1 and MWPC2.

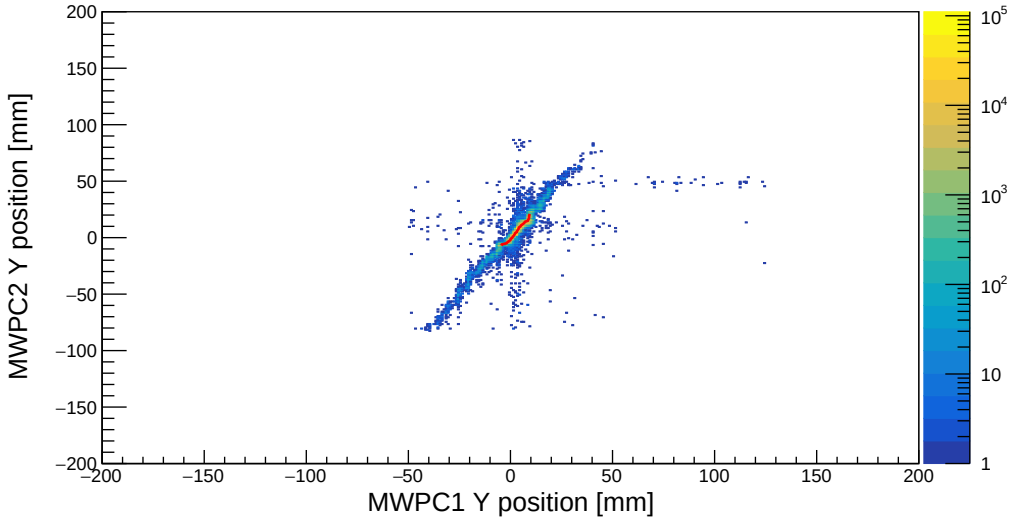

(b) y position correlation between MWPC1 and MWPC2.

Figure 4.8: Calibrated correlation plots for all ions from empty target runs between MWPC1 and MWPC2. Plot (a) is the x correlation and plot (b) is the y correlation.

4.4 CALIFA Calibration

Energy calibrations for CALIFA into the proton range is made difficult as radioactive sources typically do not provide gamma energies larger than 5 MeV. Protons typically deposit energy greater than 20 MeV therefore it is a good assumption that

a cluster with less than 20 MeV is not a proton. All crystals were calibrated using ^{22}Na and ^{60}Co source. Both these sources release two well defined gamma rays of 0.511 MeV and 1.275 MeV for ^{22}Na and 1.173 MeV and 1.332 MeV for ^{60}Co.
Figure 4.9 shows in plot (a) the mapped level energy spectra form cystal 1000–2000 fo a ^{22}Na source. Plot (b) shows the energy spectrum after calibration of the data in plot (a). The peak positions channel by channel can be found with Gaussian fits and then a offset and gain factor is determined per this can be calculated using,

$$E_i = g_i E_\gamma - o_i. \tag{4.4.4}$$

Here, E_γ is the empirically known energy of the gamma ray. g_i and o_i are the gain and offset of crystal i and E_i the mean adc (analog-to-digital converter units) value of the Gaussian fit.

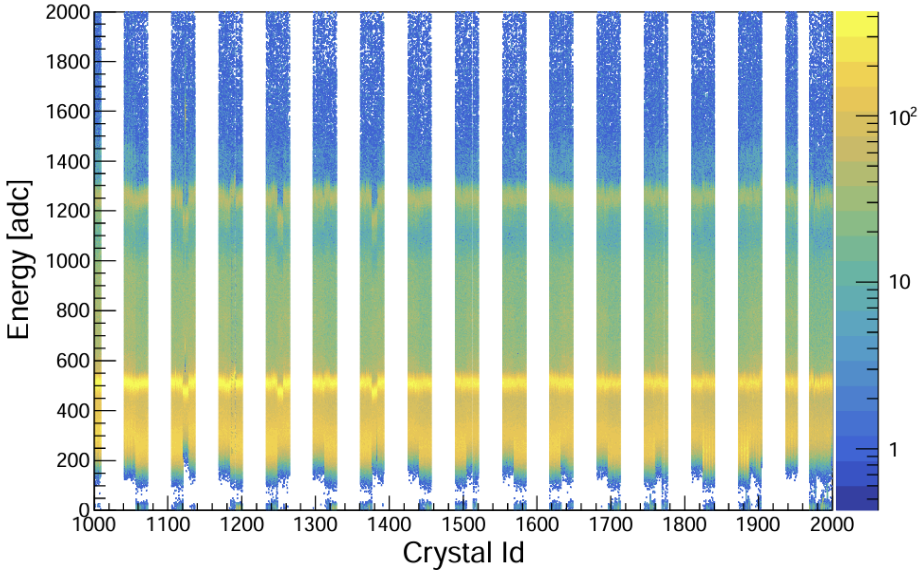

(a) CALIFA mapped level energy spectra.

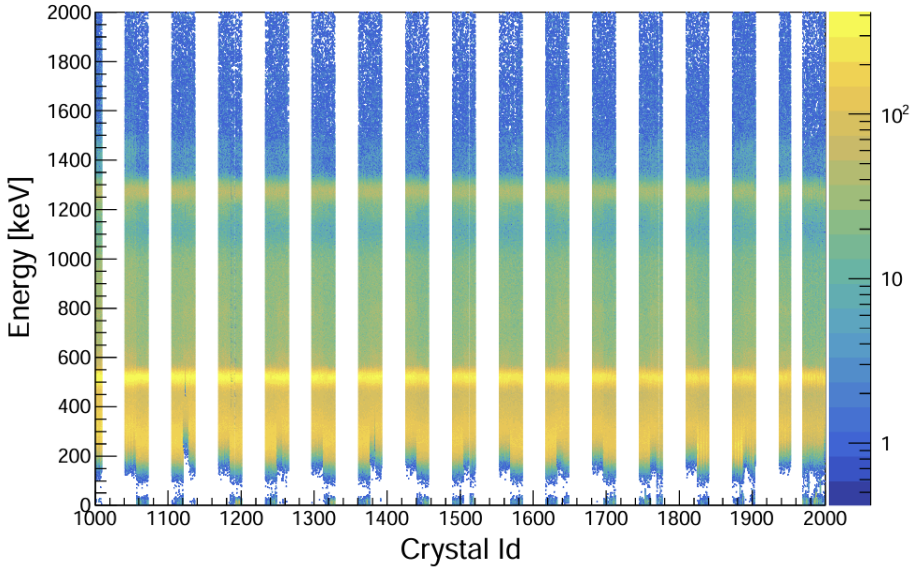

(b) CALIFA calibrated level energy spectra.

Figure 4.9: Plot (a) shows the mapped level energy for crystals 1000-2000 when measuring a ^{22}Na. Plot (b) then shows the same spectra after gain matching is applied.

Chapter 5

Simulations

It is critical to the analysis of R3B experiments to perform simulations to predict and understand the responses of detectors. An event generator developed by Leonid Chulkov [47] can be used to reconstruct kinematic variables of the scattered proton and knocked out nucleon. Figure 5.1 shows a flowchart detailing the procedure. Parameters are first set such as: which reaction channel, internal momentum spread, beam energy and binding energy. These parameters are stored in a header file called "info.hh" which is then parsed to a macro called "qfs.cc". This macro then generates primary event seeds using information stored in the header file. The output of this macro is a ROOT file called "quasi.root". Analysis of the original event seeds can be performed using a macro called "ana_file.C" to check the reaction kinematics and for comparison with simulated data. The event seeds are subsequently parsed into the FairRoot simulation package, which simulates the response of these seeds to the detectors and stores the output in a new ROOT file called "sim_quasi.root" for analysis using R3BRoot macros.

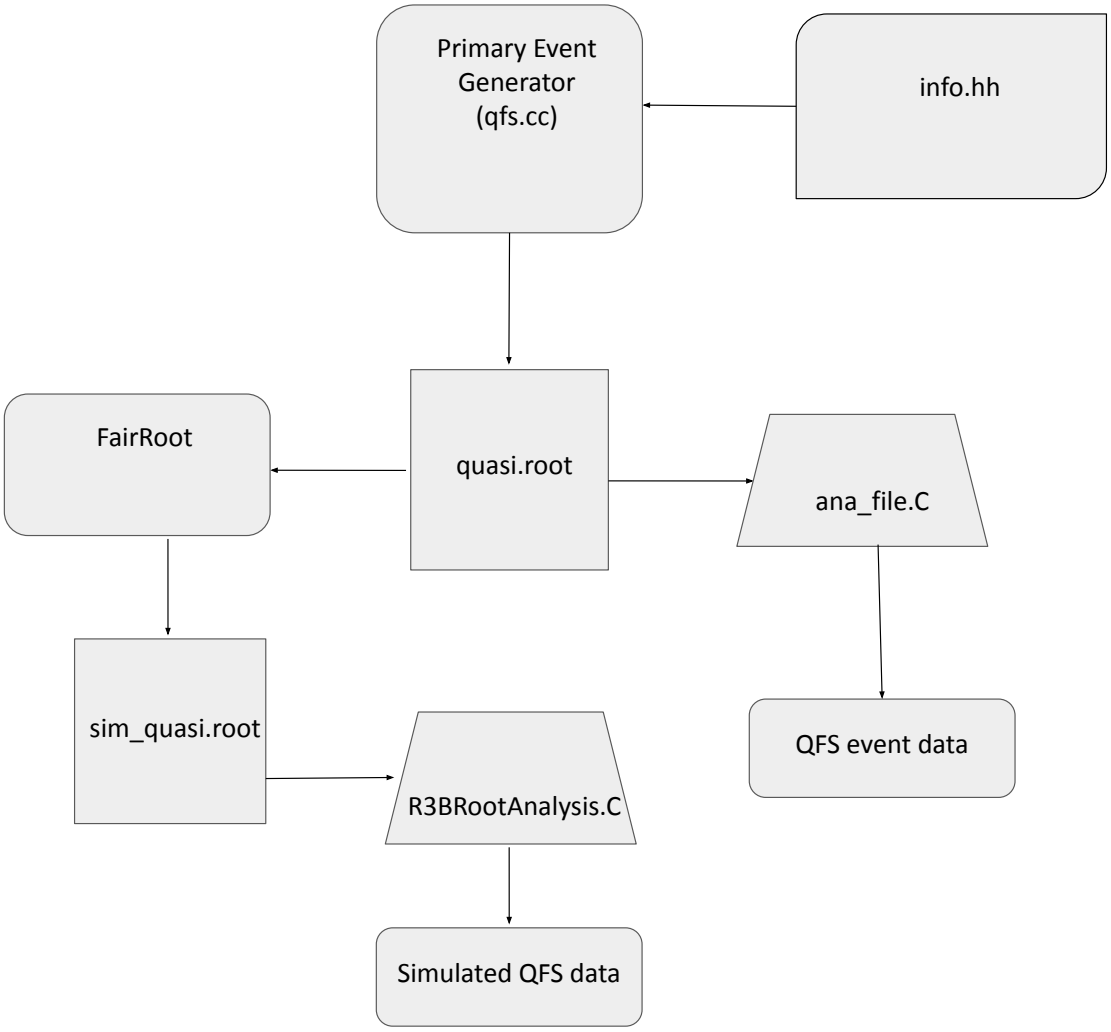

Figure 5.1: Flow chart showing how QFS events seeds are produced and then fed into FairRoot to produce simulation data. This allows for the data analysis of both the original seeds and simulated data.

5.1 QFS Event Generator

As mentioned, there are several parameters required when producing the event seeds. These parameters are each very sensitive and cause modifications to correlations.

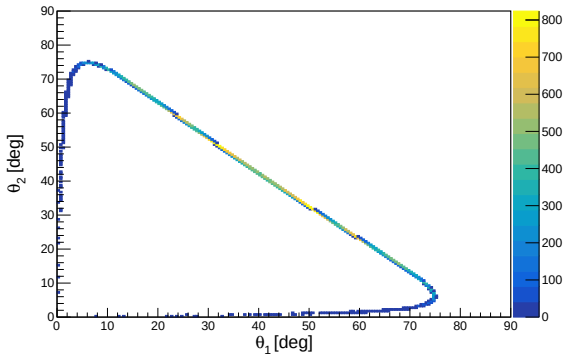

(a) 1 MeV/c internal momentum spread.

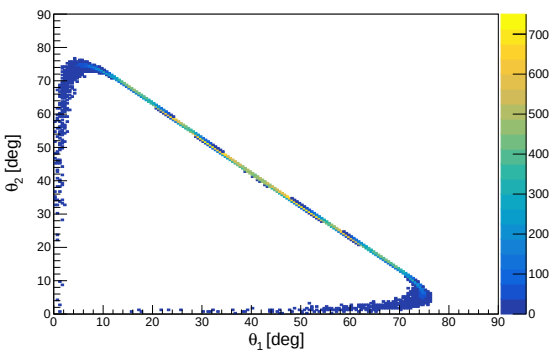

(b) 10 MeV/c internal momentum spread.

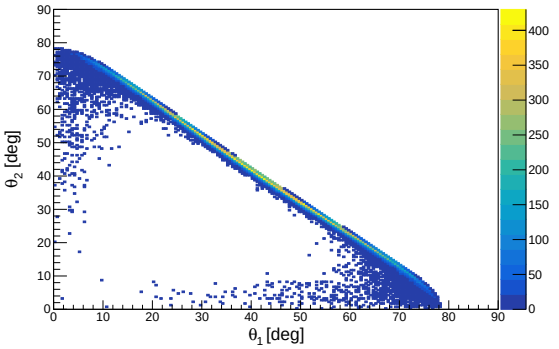

(c) 50 MeV/c internal momentum spread.

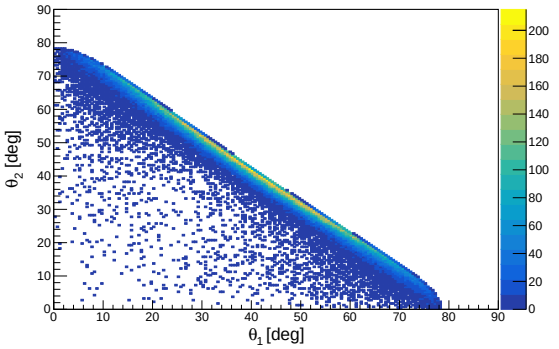

(d) 100 MeV/c internal momentum spread.

Figure 5.2: The plots (a)-(d) display theta correlation plots between the knocked out proton from ^{48}Ca and the scattered proton from the target for varying internal momentum spread of 1, 10, 50 and 100 MeV/c.

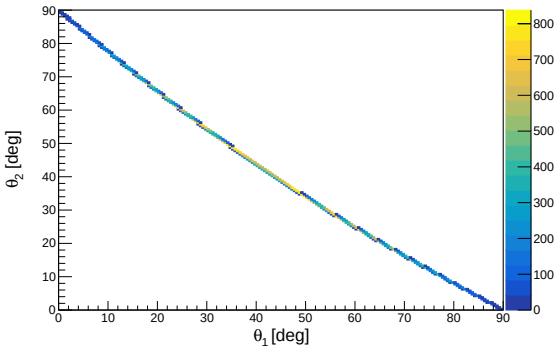

(a) 1 MeV/c internal momentum spread.

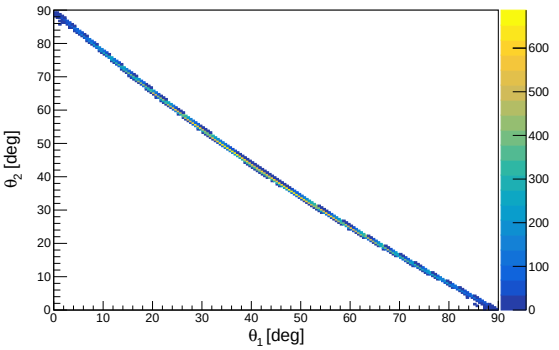

(b) 10 MeV/c internal momentum spread.

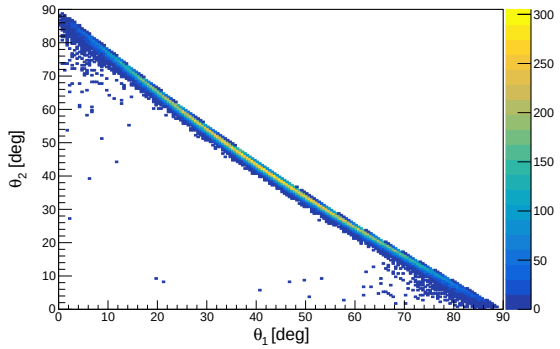

(c) 50 MeV/c internal momentum spread.

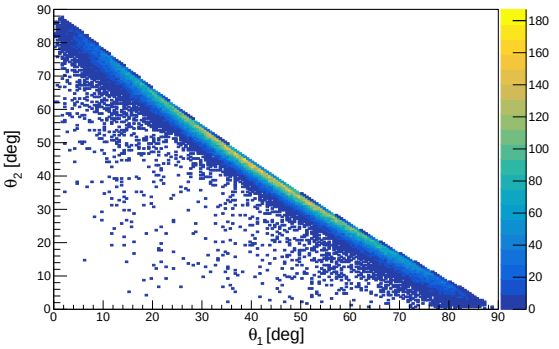

(d) 100 MeV/c internal momentum spread.

Figure 5.3: The plots (a)-(d) display correlation plots after removing the binding energy between the knocked out proton from ^{48}Ca and the scattered proton from the target for varying internal momentum spread of 1, 10, 50 and 100 MeV/c.

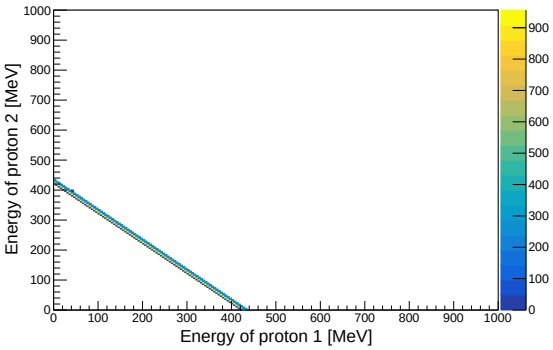

(a) 1 MeV/c internal momentum spread.

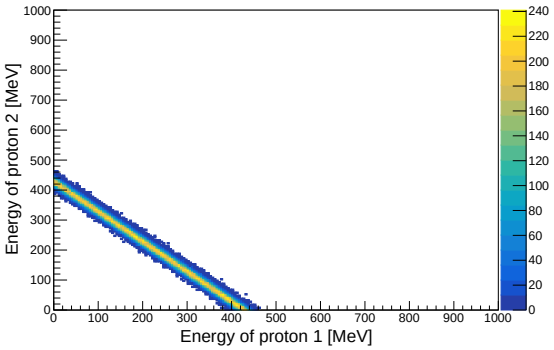

(b) 10 MeV/c internal momentum spread.

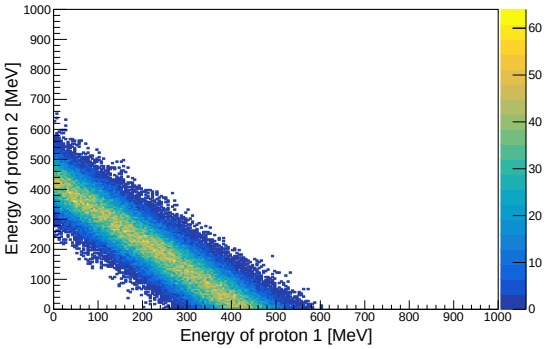

(c) 50 MeV/c internal momentum spread.

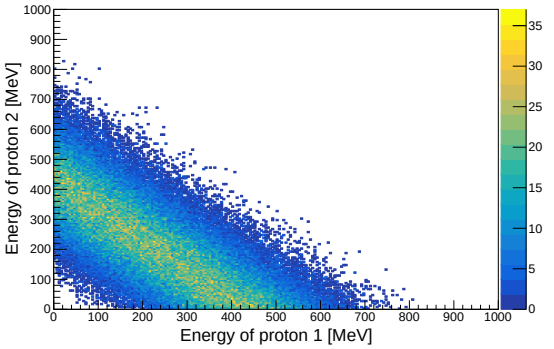

(d) 100 MeV/c internal momentum spread.

Figure 5.4: The plots (a)-(d) display energy correlation plots between the knocked out proton from ^{48}Ca and the scattered proton from the target for varying internal momentum spread of 1, 10, 50 and 100 MeV/c.

Figure 5.2 highlights the effect of increasing the internal momentum spread of the nucleon that is to be knocked out. Figure 5.3 shows the same as Figure 5.2 but with the removal of the binding energy of the nucleus. Finally Figure 5.4 shows by increasing the momentum spread we smear the energy of the knocked out and scattered nucleon. By equating both the internal momentum spread and binding energy to zero the reaction's kinematics resemble those of elastic scattering which is what is expected. Event seeds are now calculated for the Ca nuclei with significantly large statistics in the s467 experiment. Both the QFS (p,2p) and QFS (p,pn) reaction channels are considered. Parameters for the beam energy at the centre of the target

are calculated using LISE++, mass excess values for the incoming and fragment nucleus were taken from [48] and are summarised in Tables 5.1, 5.2 and 5.3.

	^{39}Ca	^{40}Ca	^{41}Ca	^{47}Ca	^{48}Ca	^{49}Ca	^{50}Ca
Mass excess [MeV]	-27.282	-34.846	-35.559	-42.344	-44.224	-41.300	-39.589

Table 5.1: Ca mass excess values [48].

	^{38}K	^{39}K	^{40}K	^{46}K	^{47}K	^{48}K	^{49}K
Mass excess [MeV]	-28.800	-33.807	33.535	-35.413	35.7120	-32.2845	-29.6115

Table 5.2: K mass excess values [48].

	^{39}Ca	^{40}Ca	^{41}Ca	^{47}Ca	^{48}Ca	^{49}Ca	^{50}Ca
E [AMeV]	411.2	392.4	374.6	513.3	495.0	477.4	460.7
Beta [c]	0.720	0.711	0.701	0.764	0.758	0.750	0.743

Table 5.3: The first row represents the beam energy at the centre of target calculated from LISE++. The second row gives the corresponding beta at the centre of target.

An internal momentum spread of 120 MeV/c was assumed for all nuclei at the time of the simulations, which was calculated by fitting opening angle distributions to experimental data for ^{48}Ca, as discussed later in this chapter. Figure 5.5 show the momentum information for both the knocked out and scattered proton for the ^{48}Ca(p,2p)^{47}K reaction channel.

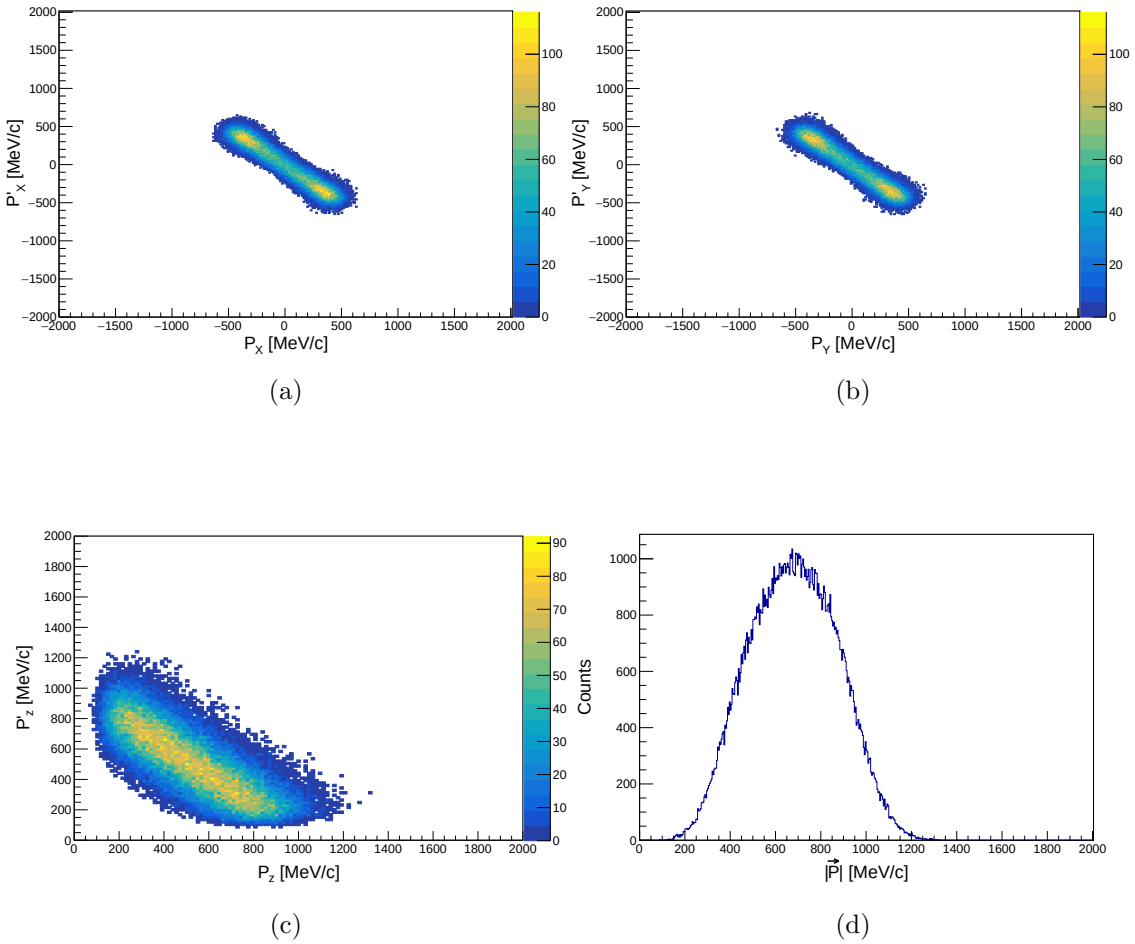

Figure 5.5: The plots (a)-(d) show momentum distributions for generated ^{48}Ca(p,2p)^{47}K events using information from Tables 5.1, 5.2 and5.3. Histograms (a)-(c) correspond to the x, y and z momentum distributions of the protons where P and P' have a random assignment between the struck and recoil proton. Histogram (d) corresponds to the magnitude of the momentum of both protons.

The event seeds are then also calculated for the (p,pn) reaction channel. Figure 5.6 shows the momentum distributions for ^{48}Ca(p,pn)^{47}Ca reaction channel again with a internal momentum spread of 120 MeV/c.

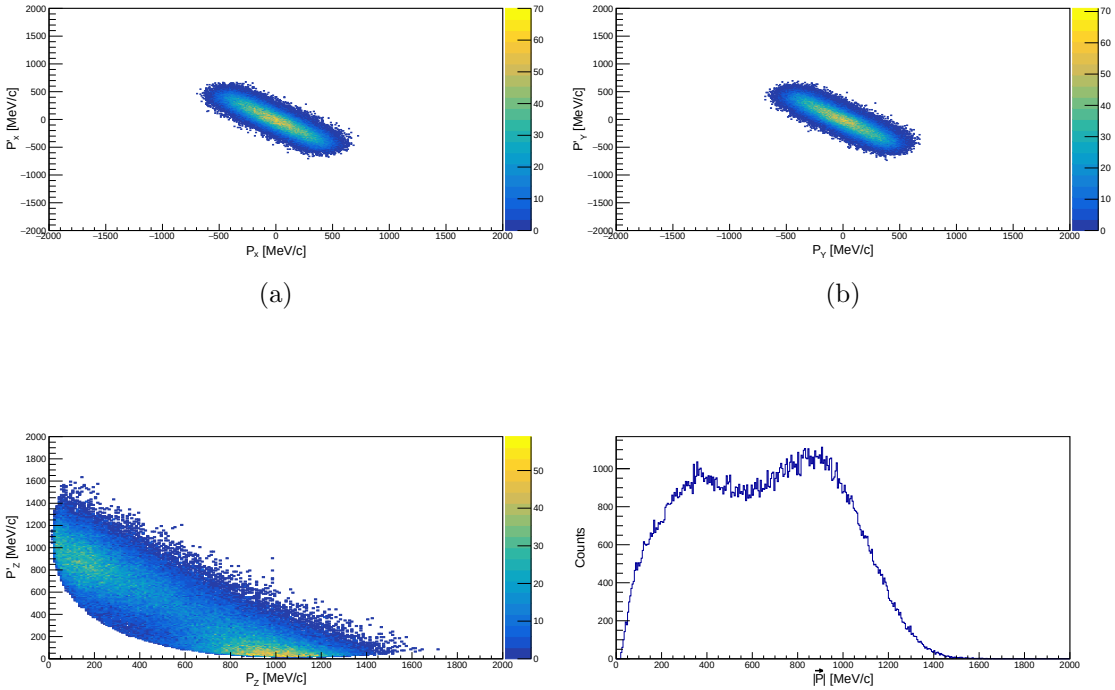

Figure 5.6: Momentum distributions for generated ^{48}Ca(p,pn)^{47}Ca events using information from Tables 5.1,5.2,5.3 . Histograms (a), (b) and (c) correspond to the x, y and z momentum distributions of the protons and knocked out neutron where P and P' have a random assignment. Histogram (d) corresponds to the magnitude the momentum.

It is important now to highlight some physical cuts which are necessary later on for the identification of proton or neutrons within CALIFA and their effects on the event seeds. A cut on the azimuthal angles between nucleons is made,

$$||\phi_1 - \phi_2| - \pi| < \phi \tag{5.1.1}$$

Here ϕ_1 and ϕ_2 is the azimuthal angle of the scattered proton and knocked out nucleon. This is done to restrict tagging clusters too close in space and to select only the strongly correlated nucleons coming from a QFS reaction. Figure 5.7 shows the effect of changing ϕ as a function of detection efficiency for both (p,2p) and (p,pn).

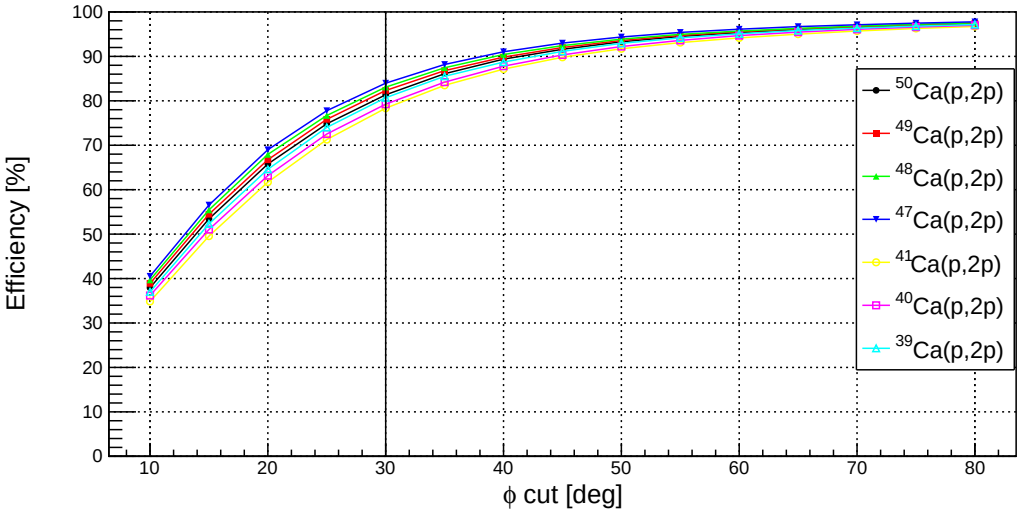

(a) Phi cut efficiencies for ^{A}Ca(p,2p)$^{A-1}$K

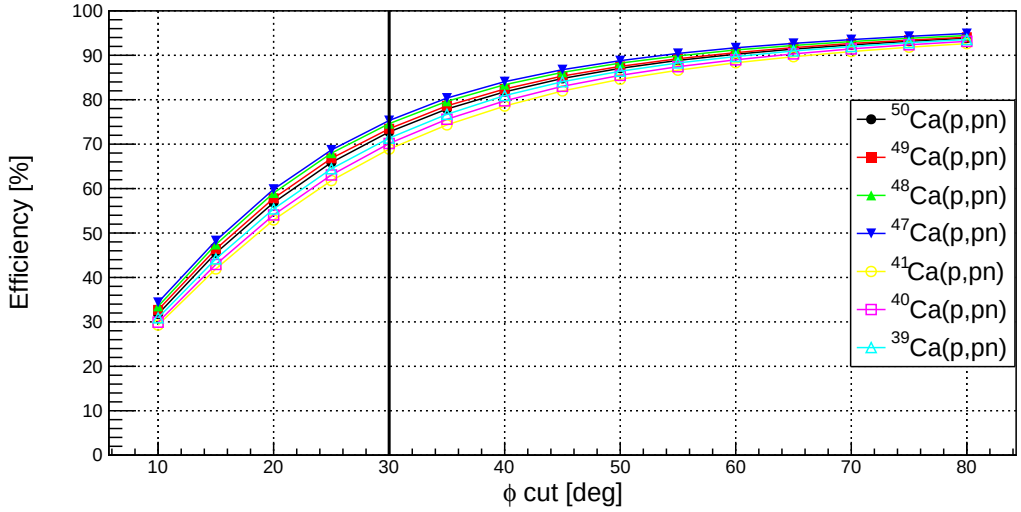

(b) Phi cut efficiencies for ^{A}Ca(p,pn)$^{A-1}$Ca

Figure 5.7: The percentage of events seeds remaining by making the cut represented in the equation 5.1.1 for varying values of ϕ.

If too low a ϕ cut is made a significantly large number of statistics are lost. A ϕ cut of 30 degrees shown as a black vertical line in Figure 5.7 is determined as a good compromise yielding on average an efficiency of 82% for (p,2p) and 72% for (p,pn). To increase this gate any larger would risk cluster misidentification. The variation in efficiency for different isotopes is within 2.5% for all cuts and no large deviation is seen. The event seeds are then passed through the FairRoot simulation framework.

This framework is based on Geant4 [49] where events are simulated in steps, at each step the energy deposited in a material is recorded for a predefined number of maximum steps. At the end of the maximum step the energy in each volume is summed giving an energy deposition in each material. This value is then digitised which is a process which converts this into the expected detector response and can be subsequently analysed following the exact same reconstruction algorithms as for experimental data. Figure 5.8 shows the θ and ϕ correlations for the reaction channel ^{48}Ca(p,2p)^{47}K.

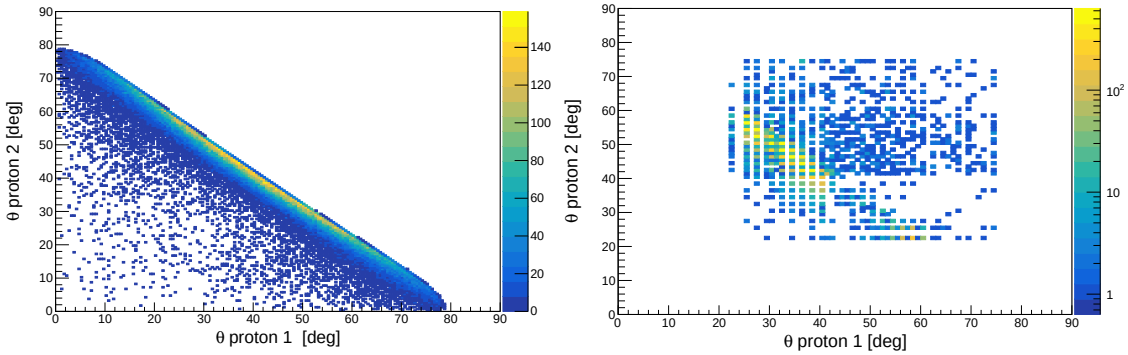

(a) Event seed θ correlation.

(b) Simulated θ correlation.

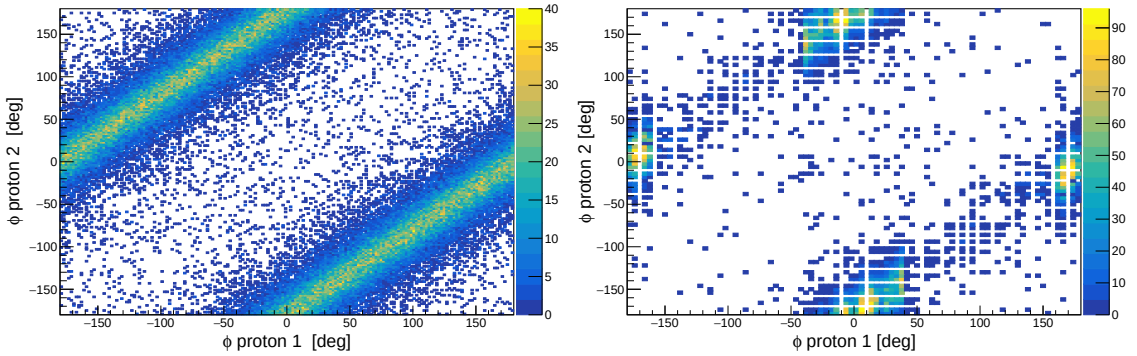

(c) Event seed ϕ correlation.

(d) Simulated ϕ correlation.

Figure 5.8: Plots (a)-(b) show θ correlation plots and plots (c)-(d) show ϕ correlations for the reaction channel ^{48}Ca(p,2p)^{47}K. Plots (a) and (c) are QFS event seed data and plots (b) and (d) are simulated data after being parsed through R3BRoot.

In Figure 5.8 plots (a) and (c) show the event seed angular correlation between protons. Plots (b) and (d) show the same as (a) and (c) but after being parsed through the full simulation framework. It is clear from plot (b) that there is a reduced θ acceptance and that the angular resolution of CALIFA is some what limited.

5.2 Reaction Vertex Studies

Studies on the effect of the positioning of the reaction vertex where performed as this is crucial to determine the overall CALIFA (p,2p) and (p,pn) efficiency.

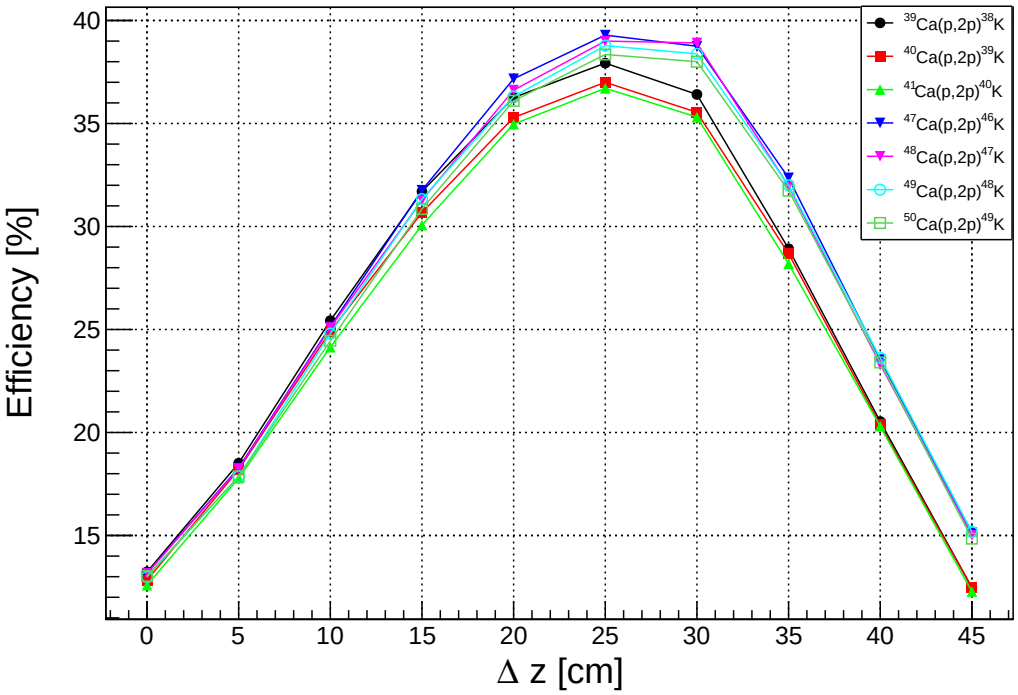

Figure 5.9: Efficiencies calculated from simulation for several Ca isotopes as a function of the targets z position.

From Figure 5.9 it is clear that the proton detection efficiency is rather sensitive to the exact target position along the beamline. The value for the target position was calculated using two different independent measurements to be either, 39.5 mm or 35.3 mm.

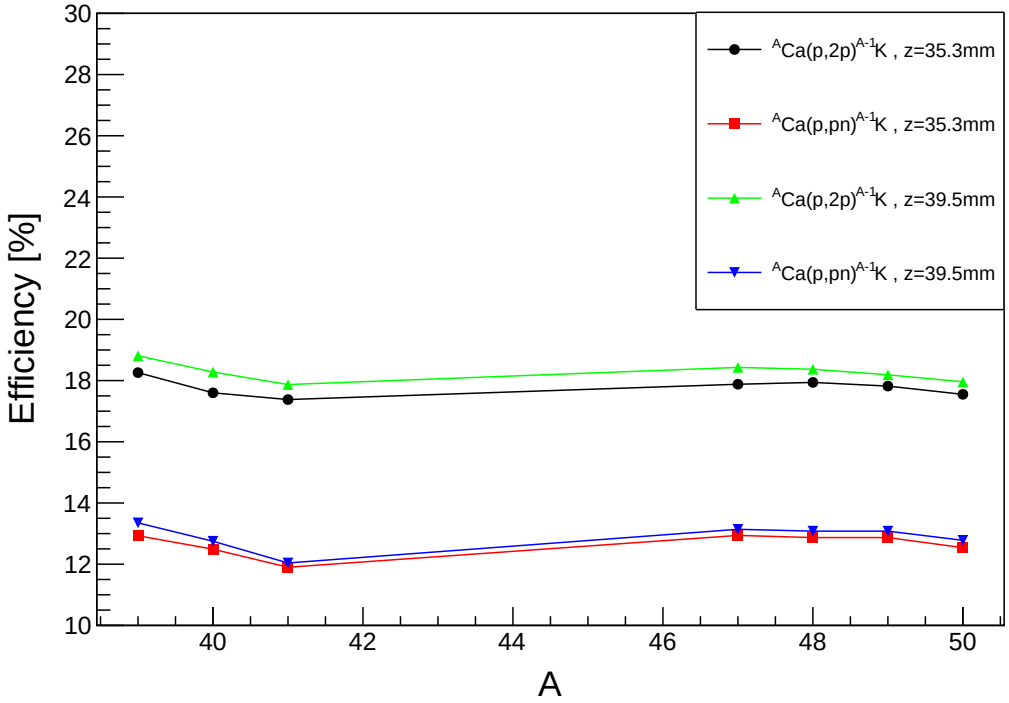

Figure 5.10: Efficiency calculated from simulation for the two possible z positions for both the (p,2p) and (p,pn) reaction for a variety of different Ca isotopes.

As is seen in Figure 5.10 both z position values are consistent for both reaction mechanisms with a deviation of less than 1%. Therefore 39.5 mm has been taken and a systematic error of 1% is considered. This study was also then performed for the modifications to the x and y position of the target for QFS (p,2p). Figure 5.11 shows how the efficiency changes for the reaction channel ^{50}Ca(p,2p)^{49}K.

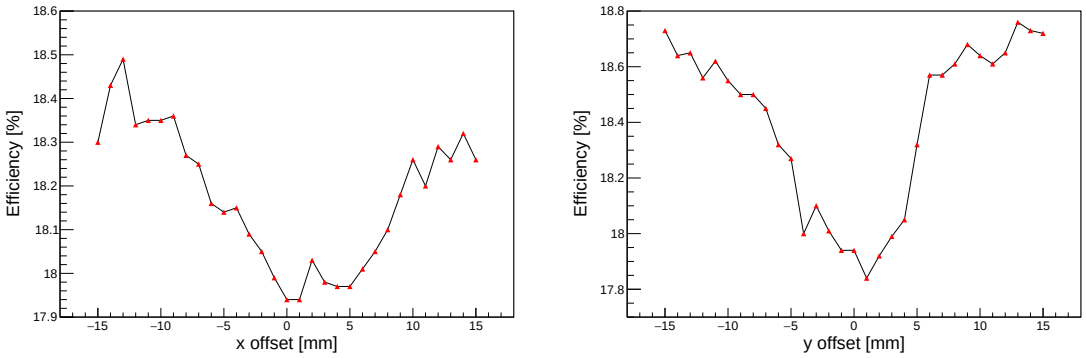

(a) (b)

Figure 5.11: Evolution of the efficiency for ^{50}Ca(p,2p)^{49}K as the x and y position is modified in increments of 1 mm both in the positive and negative direction around the nominal target position.

In 5.11 plot (a) shows the effect on the efficiency by changing the targets x position and plot (b) shows the effect on y. This variation is within ±0.5% for both x and y, therefore we can introduce a systematic error of 0.5% for each axis. The total systematic error derived from the simulation is calculated as the linear sum of individual contributions, resulting in a total of 2%. By averaging values from Figures 5.11, 5.10 a CALIFA (p,2p) detection value is determined to be 18.2% and for (p,pn) 12.7%. The calculated (p,pn) efficiency is notably larger than expected and will be discussed in Chapter 9.

5.3 QFS Reaction Plane

Using the angular information from CALIFA it is also possible to calculate geometrical quantities that describe the reaction kinematics.

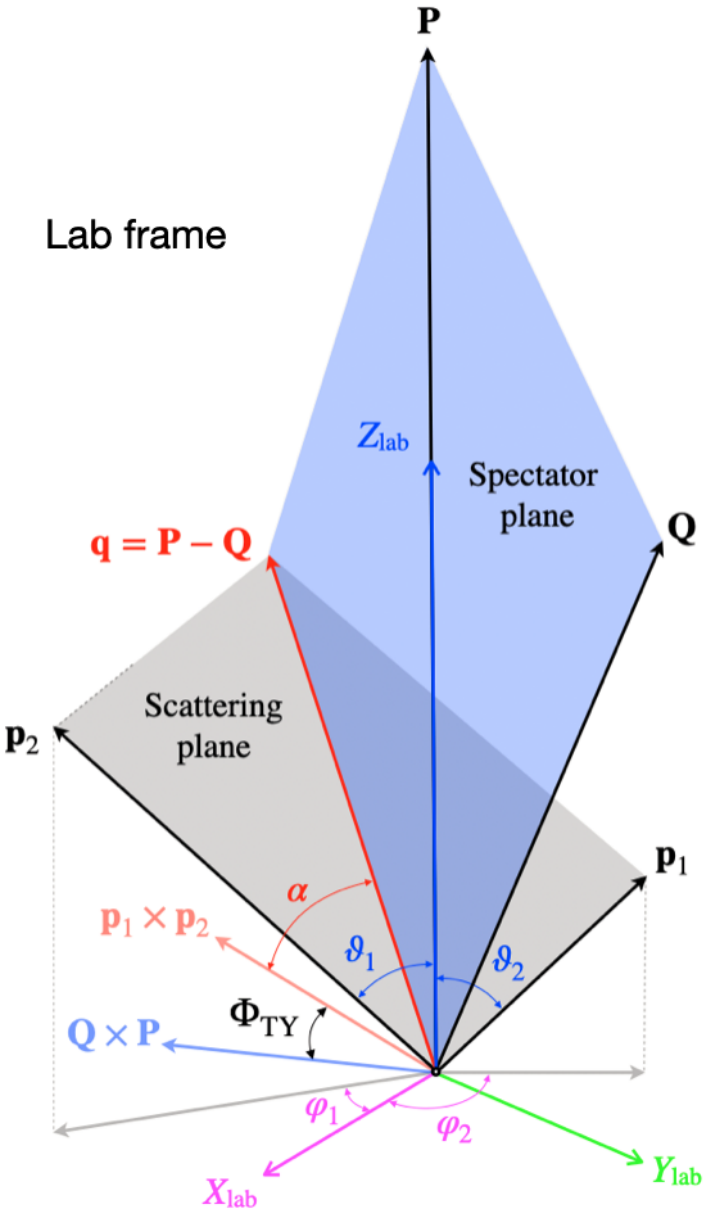

Figure 5.12: Reaction kinematics for a QFS reaction. Plot taken from [50].

Figure 5.12 shows several kinematic quantities constructed from the momentum of the beam particle as well as the scattered proton and knocked out nucleon. The angle between the scattering plane and the spectator plane is calculated using,

$$cos(\alpha) = \frac{\vec{p_1} \times \vec{p_2}}{|\vec{p_1} \times \vec{p_2}|} \cdot \frac{\vec{P} - \vec{Q}}{|\vec{P} - \vec{Q}|} \approx 0. \tag{5.3.2}$$

Here $\tilde{p}_1, \tilde{p}_2$ are the momentum vectors for the knocked out nucleon and scattered proton and $\vec{P}, \vec{Q}$ the parent and daughter nuclei respectively. It is also possible with

fragment analysis to test the Treiman-Yang criterion[51] using,

$$cos(\Phi_{\mathrm{TY}}) = \frac{\vec{p_1} \times \vec{p_2}}{|\vec{p_1} \times \vec{p_2}|} \cdot \frac{\vec{Q} \times \vec{P}}{|\vec{Q} \times \vec{P}|}. \tag{5.3.3}$$

However for simulated data this criterion is not necessary as either the (p,2p) or (p,pn) generator is used, therefore the exact source of all event seeds is known. The opening angle between the scattered nucleon and the knocked out proton is given by,

$$cos(\theta_{\mathrm{OA}}) = \frac{\vec{p_1} \cdot \vec{p_2}}{|\vec{p_1} \cdot \vec{p_2}|}. \tag{5.3.4}$$

Opening angle distributions for the ^{48}Ca(p,2p)^{47}K reaction channel using a variety of internal momentum spread are shown in Figure 5.13.

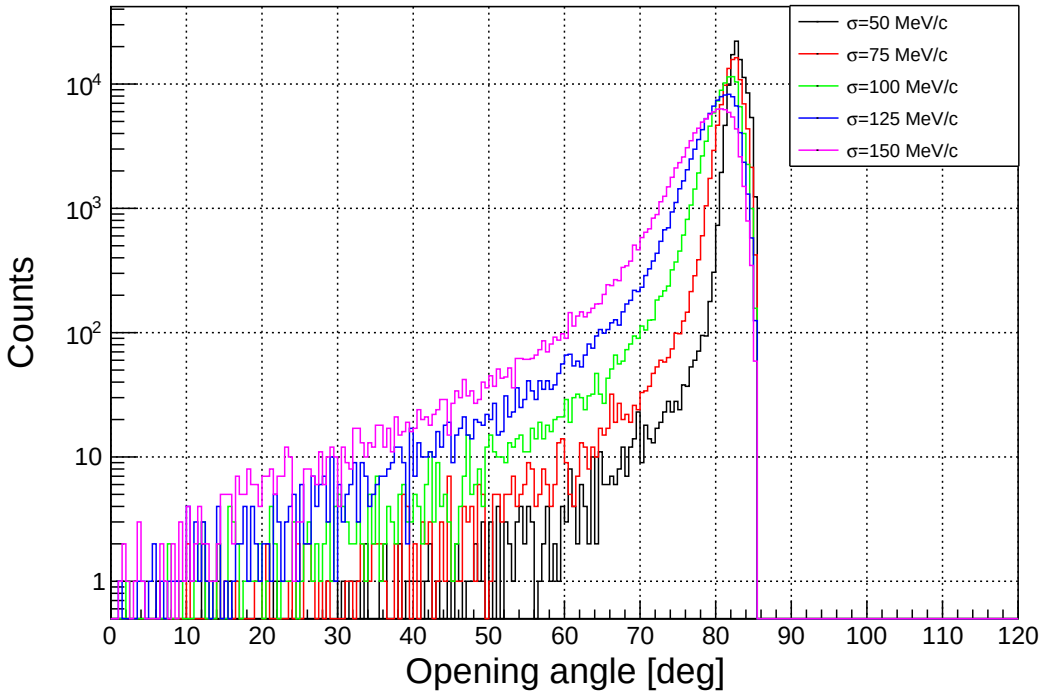

Figure 5.13: Opening angle distributions between the knocked out proton and scattered proton from the (p,2p) event generator for varying momentum spreads.

As previously stated the momentum spread of 120 MeV/c was used for the efficiency studies, however the purpose of Figure 5.13 is to highlight the effect of modifying the internal momentum spread on the opening angle. Figure 5.13 shows that as the internal momentum spread increases, the distribution broadens, and the peak shifts to a lower opening angle.

Chapter 6

Analysis

This chapter focuses on the analysis methods used for the s467 experiment [21]. The first section outlines the tracking procedure after the GLAD magnet for the fragment identification. This is followed by a description of the in beam tracking process for ions and fragments, and the reconstruction of proton momentum using CALIFA. Finally the target thickness and transmission probabilities for the available ions are presented.

6.1 Momentum Reconstruction of the Fragments

An ion transfer matrix was used for the Bρ and A/Q reconstruction after GLAD. This assumes that GLAD behaves as a perfect dipole, affecting only the x-component of the ions position and angle. The translation matrix is given as,

$$\begin{pmatrix} x_{out} \\ \theta_{out} \\ \delta \end{pmatrix} = \begin{pmatrix} a_{xx} & a_{x\theta} & a_{x\delta} \\ a_{\theta x} & a_{\theta\theta} & a_{\theta\delta} \\ 0 & 0 & 1 \end{pmatrix} \begin{pmatrix} x_{in} \\ \theta_{in} \\ \delta \end{pmatrix}. \tag{6.1.1}$$

Equation 6.1.1 contains a matrix of fit parameters a_{ij} where i and j represent the position in the matrix (x, θ or δ). Where x_{in} is the x position measured by MWPC2, x_{out} is the x position measured by MWPC3, θ_{in} the incoming x angle which can be calculated either from the drift angle of TWIM or from the angular reconstruction

between MWPC1 and MWPC2, which is discussed later in this chapter. Using matrix multiplication an equation for the x position after the magnet is given by,

$$x_{out} = a_{xx}x_{in} + a_{x\theta}\theta_{in} + a_{x\delta}\delta. \tag{6.1.2}$$

Here δ is the momentum deviation from the nominal Bρ of GLAD. As there is only the MWPC3 detector for both x and y measurement installed after GLAD only equation 6.1.2 can be assumed to be valid. The magnetic rigidity of the fragment is then reconstructed using,

$$\mathrm{B}\rho = \mathrm{B}\rho_0(1+\delta). \tag{6.1.3}$$

The absolute x position of the MWPC3 detector is made by using a fitting procedure. This modifies equation 6.1.2 to be,

$$x'_{out} = x_{out} - (a_{xx}x_{in} + a_{x\theta}\theta_{in}) = a_{x\delta}\delta \tag{6.1.4}$$

Where x'_{out} is the now modified x position. In Figure 6.1 plot (a) shows the Bρ correlation between the Bρ measured in FRS and the reconstructed fragment Bρ, which uses this modified x position in its calculation. Plot (b) then shows the difference of the two values as a function of the FRS Bρ. Plots (c) and (d) are then slices of plot (b) taken with size $\pm$0.025 Tm in regions 9.0 Tm and 9.1 Tm. Gaussian distributions are fitted to plots (c) and (d) of Figure 6.1 giving resolution of $25.35(7)\times10^{-3}$ Tm and $24.93(7)\times10^{-3}$ respectively.

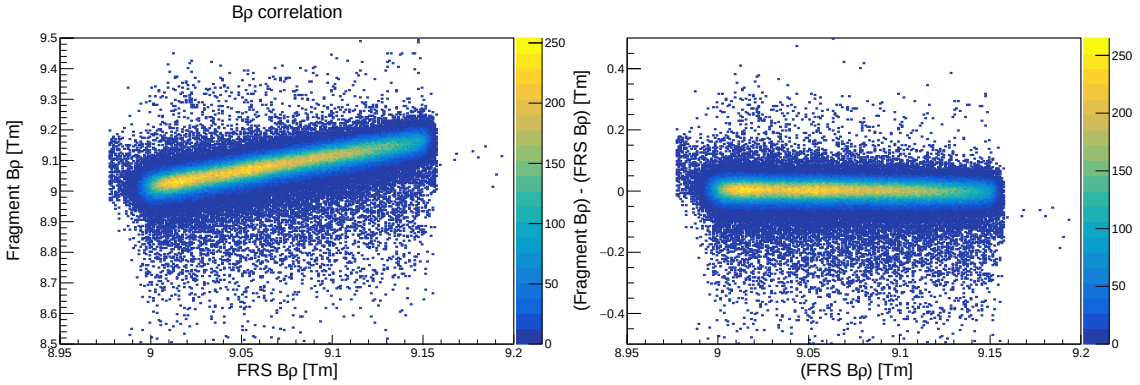

(a) Bρ correlation.

(b) Bρ correlation difference.

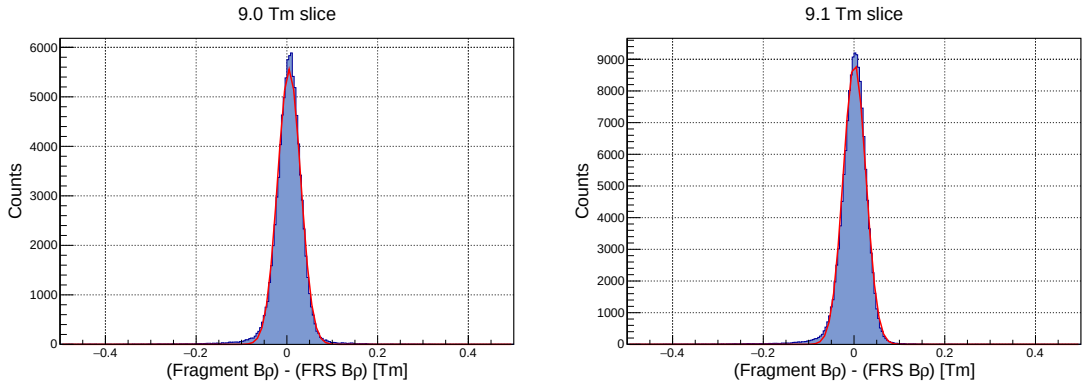

(c) 9 Tm slice of plot (b).

(d) 9.1 Tm slice of plot (b).

Figure 6.1: Correlation of Bρ from FRS and Fragment tracking with modified x position. The empty target ^{50}Ca setting was used. Slices of 9.0 and 9.1 Tm are produced and fitted with Gaussian distributions and a resolution of $25.35(7)\times10^{-3}$ Tm and $24.93(7)\times10^{-3}$ Tm are calculated respectively.

6.2 Beam Momentum Reconstruction

The reconstruction of the beam momentum before and after the target is essential for constructing the kinematics of the reaction. Accurate momentum reconstruction allows for the precise determination of the energy transferred during a reaction. This is crucial for the understanding of the reaction dynamics.

6.2.1 Principles

The MWPC detectors before GLAD can be used to construct both the incoming and outgoing tracks from the target. Figure 6.2 shows a schematic diagram of the track reconstruction algorithm used.

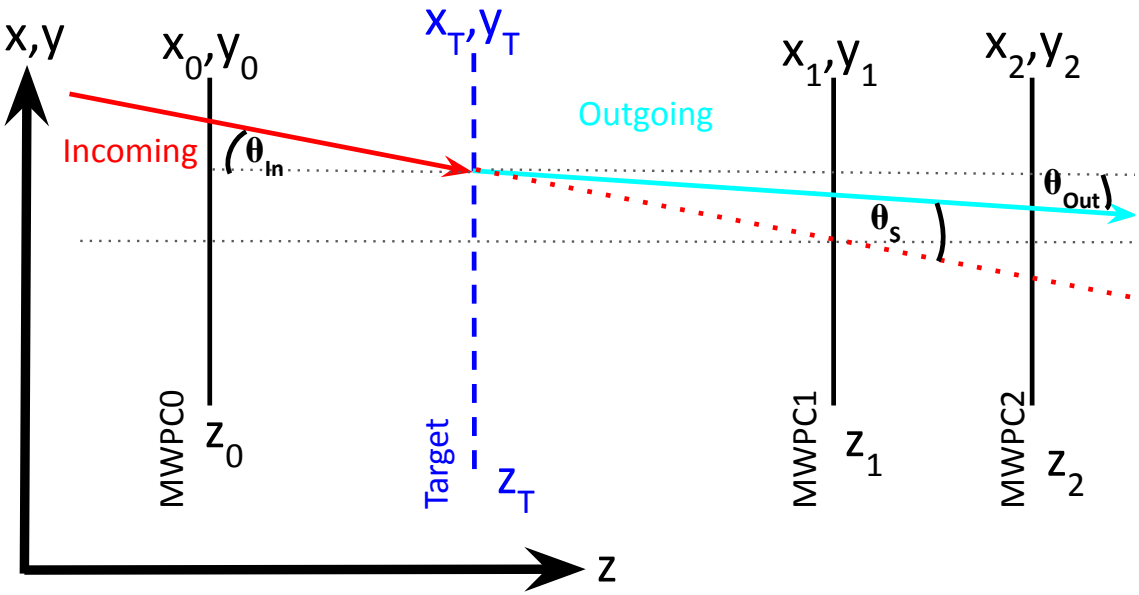

Figure 6.2: Schematic diagram showing how the track reconstruction was performed in either plane xz or yz using the MWPC detectors.

The outgoing track angle can be calculated using MWPC2 and MWPC1,

$$\tan\left(\theta_{\mathrm{Out,x}}\right) = \frac{x_2 - x_1}{z_2 - z_1}, \qquad \tan\left(\theta_{\mathrm{Out,y}}\right) = \frac{y_2 - y_1}{z_2 - z_1}. \tag{6.2.5}$$

The angle of the ion coming from the target is divided into x and y components, $\theta_{\mathrm{Out,x}}$ and $\theta_{\mathrm{Out,y}}$ respectively. Using this information the target position in x and y is reconstructed using the equations,

$$x_T = x_1 - \frac{(x_2 - x_1)\,(z_1 - z_{\mathrm{T}})}{(z_2 - z_1)}, \qquad y_T = x_1 - \frac{(y_2 - y_1)\,(z_1 - z_{\mathrm{T}})}{(z_2 - z_1)}. \tag{6.2.6}$$

Figure 6.3 shows the projected x component distribution for Ca isotopes in the target region for empty target runs. It is clear that the majority of Ca isotopes arrive within the target position. When fitting Gaussian distributions to the points

for each isotope a very small amount of the fit goes outside the target region, however this is deemed negligible and removed in further analysis by applying a target area cut.

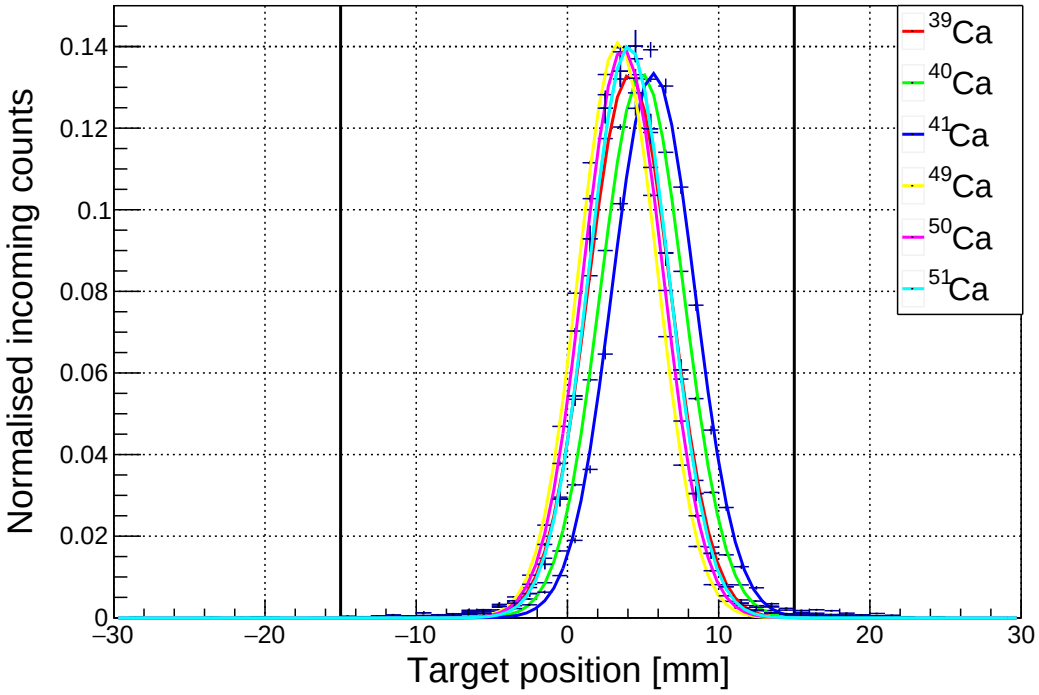

Figure 6.3: The projected x position at the target for various Ca isotopes gated on the unreacted beam condition.

Finally, the angle of the incoming ion can be determined using the projection of the target and data from MWPC0,

$$\tan\left(\theta_{\mathrm{In,x}}\right) = \frac{x_0 - x_{\mathrm{T}}}{z_0 - z_{\mathrm{T}}}, \qquad \tan\left(\theta_{\mathrm{In,y}}\right) = \frac{y_0 - y_{\mathrm{T}}}{z_0 - z_{\mathrm{T}}}. \tag{6.2.7}$$

The momentum magnitude before the target can be calculated using,

$$|\vec{\mathrm{P}}_{\mathrm{In}}| = \gamma_{\mathrm{In}}|\vec{\beta_{\mathrm{In}}}|\mathrm{M}_{\mathrm{In}}. \tag{6.2.8}$$

Where $\vec{\mathrm{P}}_{\mathrm{In}}$ is the magnitude of the incoming ions momentum, $|\vec{\beta_{\mathrm{In}}}|$ is the magnitude of the velocity vector calculated through ToF measurements between S2 and SofSci or S8 and SofSci. The mass of the ion M_{In} is determined from the A/Q value calculated using equation 3.2.1. Similarly the outgoing fragment momentum can be

calculated from the Bρ reconstruction of GLAD,

$$|\vec{P}_{Out}| = \gamma_{Out}|\vec{\beta_{Out}}|M_{Out}. \tag{6.2.9}$$

Where $\vec{P}_{Out}$ is the magnitude of the fragments momentum, $|\vec{\beta_{Out}}|$ is the magnitude of the velocity vector calculated through ToF between SofSci and the SofToFW and the mass of the ion M_{In} calculated from the Bρ reconstruction. The momentum of the scattering plane is given by,

$$P_S = \vec{P}_{In} - \vec{P}_{out}. \tag{6.2.10}$$

This momentum can be decomposed into longitudinal and transverse components respectively using,

$$P_{\parallel S} = \left(P_{S,x}^2 + P_{S,y}^2\right)^{1/2}, \qquad P_{\perp S} = P_{In,z} - P_{Out,z}. \tag{6.2.11}$$

6.2.2 Angular Straggling in the Reaction Targets

The straggling within a target can be estimated using a Gaussian fit around the scattering angle. Figure 6.4 shows the xz plane scattering angle for ^{48}Ca which has a Gaussian fit applied, here the empty target contribution has not been subtracted.

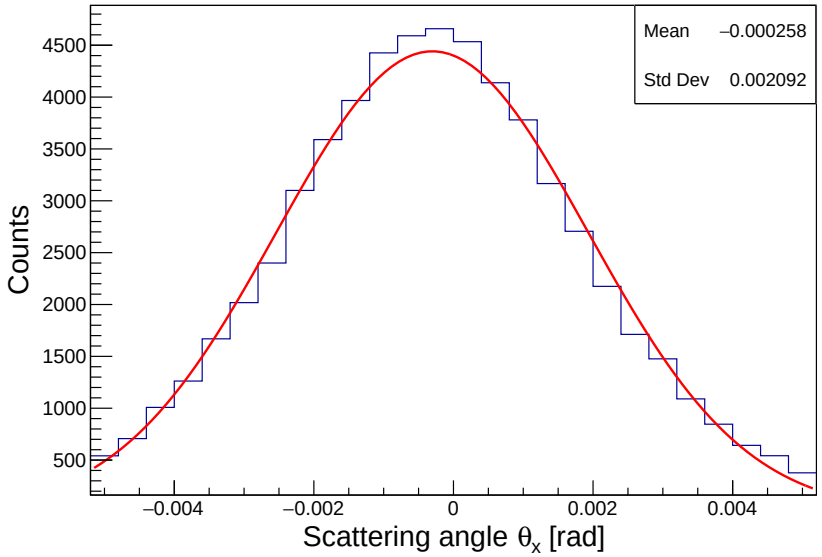

Figure 6.4: Scattering angle x for ^{48}Ca on C target. The straggling from the rest of the detector setup has not yet been subtracted.

This procedure is then done for several Ca isotopes for all three target settings. The empty contribution is then quadratically subtracted to find the straggling in the target. Results for straggling in C and CH_2 are shown in Table 6.1 along with the result calculated using ATIMA [52] for comparison. As can be seen in Table 6.1 the straggling can be calculated reasonably well for the majority of Ca isotopes.

Isotope	Beam energy (MeV/u)	C σ_x (mrad)	ATIMA Cσ_x (mrad)	CH_2 σ_x (mrad)	ATIMA CH_2 σ_x (mrad)
^{38}Ca	448.2	2.0(2)	2.3	2.1(2)	2.4
^{39}Ca	429.2	2.2(2)	2.3	2.4(2)	2.5
^{40}Ca	411.3	2.3(1)	2.3	2.5(1)	2.5
^{47}Ca	541.4	1.6(2)	1.5	1.7(3)	1.6
^{48}Ca	522.9	1.5(1)	1.5	1.6(1)	1.6
^{49}Ca	505.1	1.5(1)	1.5	1.6(1)	1.6

Table 6.1: Angular resolution of beam isotopes after empty run subtraction and their corresponding values predicted from ATIMA for C and CH2 targets.

6.3 QFS Tagging Using CALIFA

For a (p,2p) reaction a homogeneous distribution between protons is assumed. From Figure 5.12 a reaction plane between the scattered and knocked out protons can be seen. It is a reasonable assumption that during a (p,2p) reaction the scattered and knockout protons are measured in different half's of CALIFA. A cut on the azimuthal angle, ϕ also removes the contribution of clusters too close in phase space (these would be events with very low opening angle). For the identification of a proton a cluster of energy larger than 20 MeV is required to lower the chance of cluster misidentification. The effect of these cuts on proton removal events using tracking can be seen in Figure 6.5.

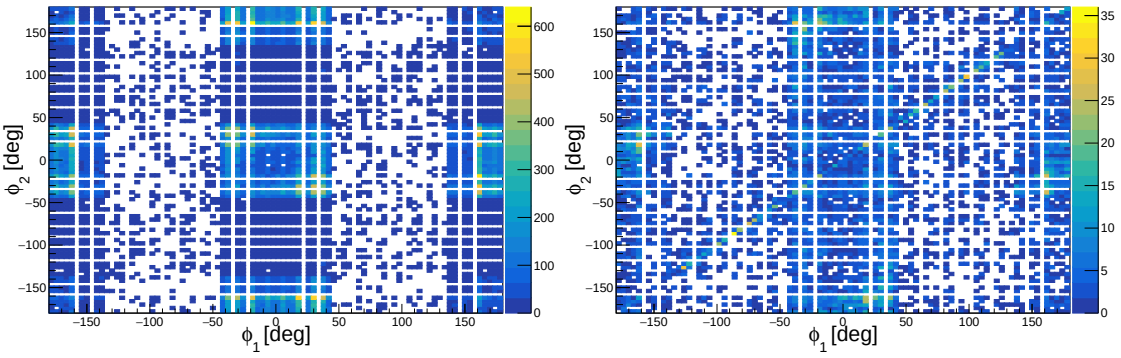

(a) Two 20 MeV cluster cut.

(b) Tracking (p,2p) cut.

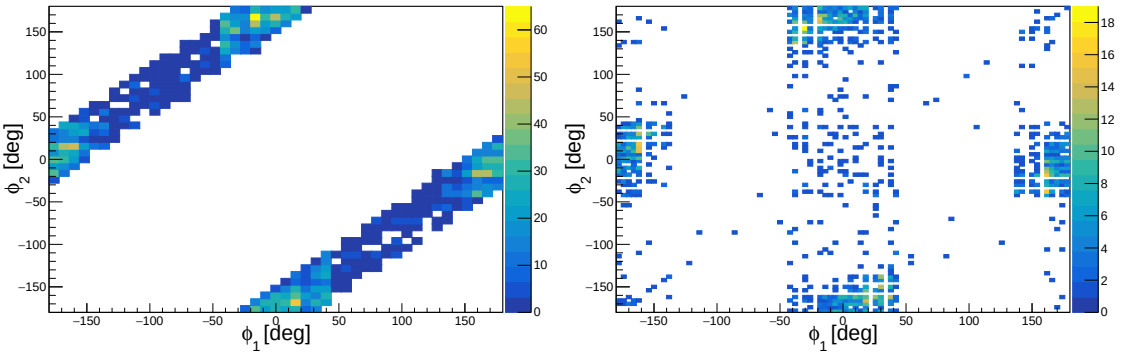

(c) Phi angle cut.

(d) Tracking (p,2p) and 20 MeV cluster cut

Figure 6.5: Effects of the different cuts on CALIFA data for all ^{50}Ca CH_2 target runs.

From Figure 6.5 plot (a) shows the ϕ angular correlation when two 20 MeV or higher clusters are detected, plot (b) shows the cut when searching for (p,2p) events when comparing the charge and mass in for the incoming beam and outgoing fragment. Plot (c) shows the cut when applying equation 5.1.1 with a value of ϕ=30 degrees. Plot (d) is the combination of the cuts in plot (a) and (b). Putting together all the cuts represented in plots (a), (b) and (c) gives the phi correlation shown in Figure 6.6.

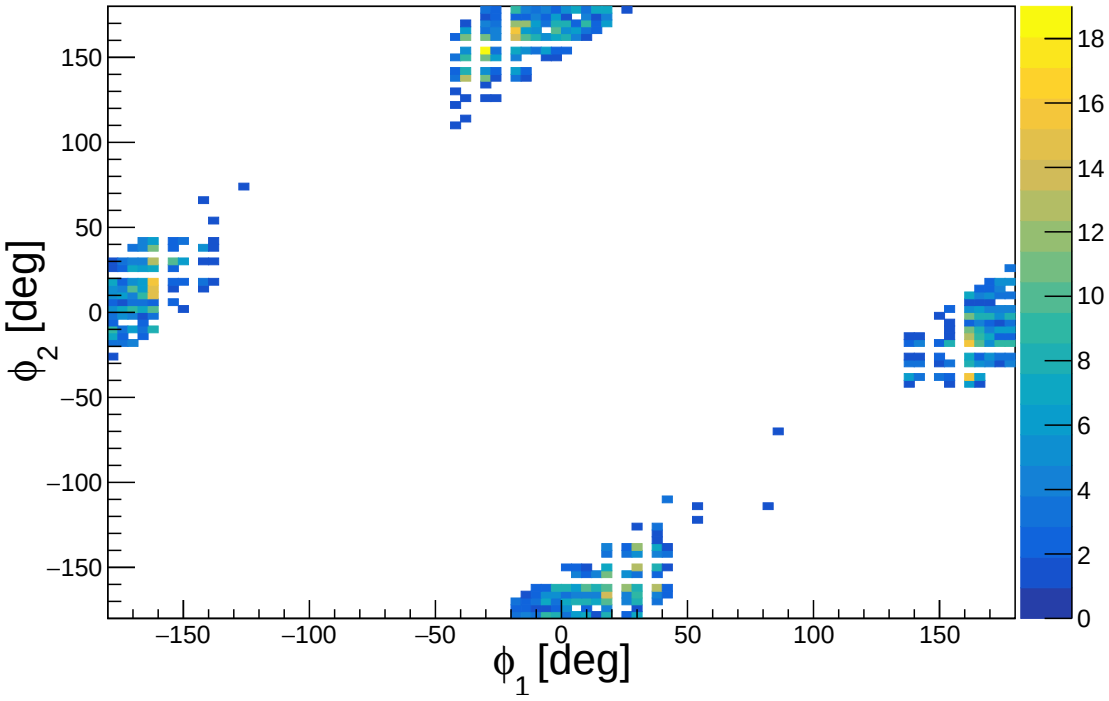

Figure 6.6: Azimuthal angle correlation plot between two clusters for all ^{50}Ca runs with CH_2 target. Several cuts are made here such as: both clusters must have energies larger than 20 MeV, the clusters must be well separated spatially, and the event must be identified as a (p,2p) reaction based on data from the FRS and fragment tracking.

6.3.1 Proton Momentum

At the energy regime of this experiment the majority of protons will be stopped within the volume of CALIFA. Therefore, the total energy of a cluster corresponds to the kinetic energy of the stopped proton. The kinetic energy is then used to determine the magnitude of the momentum of the proton,

$$|q| = (T_k(T_k + 2m_p))^{\frac{1}{2}} . \tag{6.3.12}$$

Here T_k is the kinetic energy of the stopped proton which is equal to the energy of the cluster. Using the cuts described in section 6.3 the momentum of protons from (p,2p) events can be reconstructed. This also has the added assumption that

the vertex is point like and located at the centre of the target. Figure 6.7 shows the reconstructed momentum distributions for all (p,2p) events for the ^{50}Ca runs using a CH_2 target. This is directly comparable to the equivalent simulation plots presented in Figure 5.5.

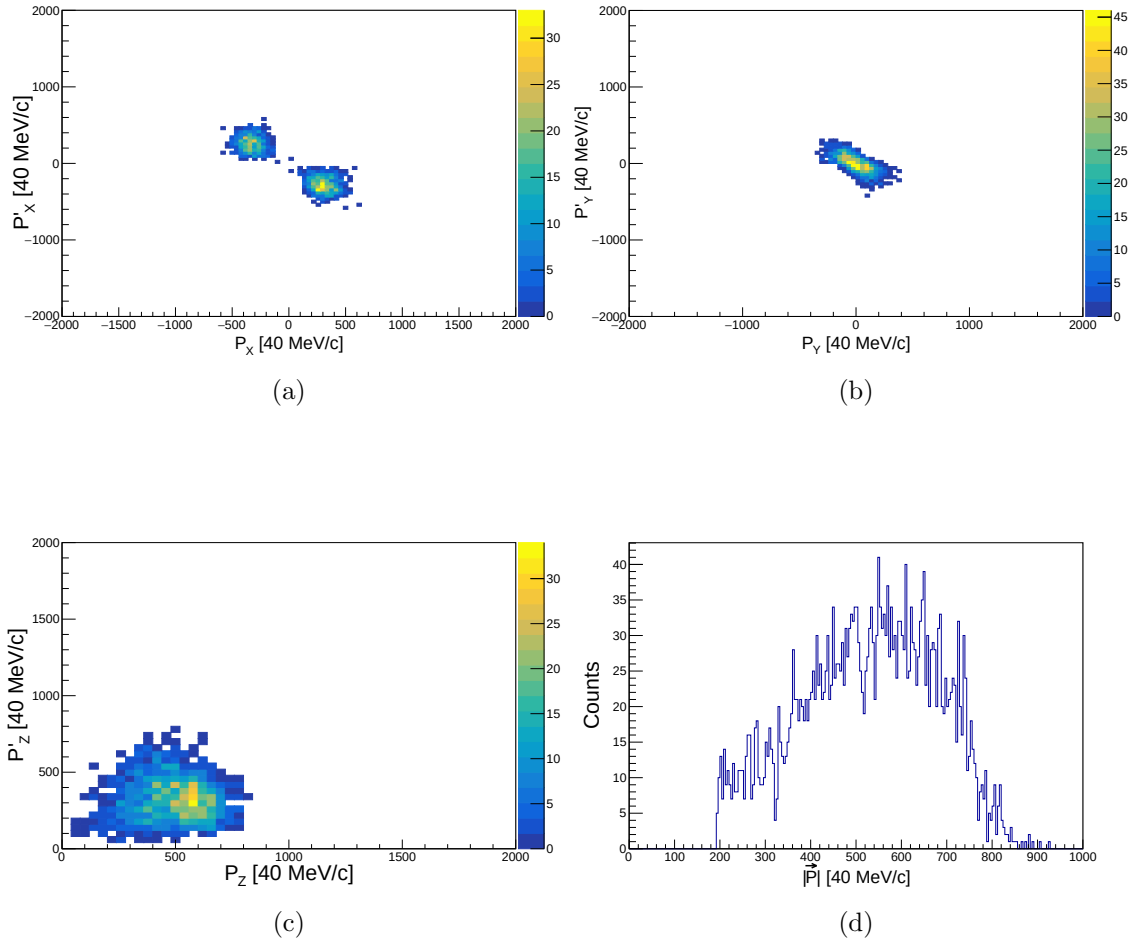

Figure 6.7: Momentum correlations between both protons in (p,2p) events for ^{50}Ca beam setting and CH_2 target. Here no background subtraction is applied and all available (p,2p) candidates are shown.

From Figure 6.7 plots (a), (b) and (c) show the x, y and z momentum correlations between protons. Plot (d) shows the magnitude of the momentum vectors. Using the angular information from each proton the opening angle is calculated using equation 5.3.4. Figure 6.8 shows the opening angle between protons for the ^{40}Ca(p,2p)^{39}K reaction channel using data from only the ^{38}Ca runs on a CH_2 target.

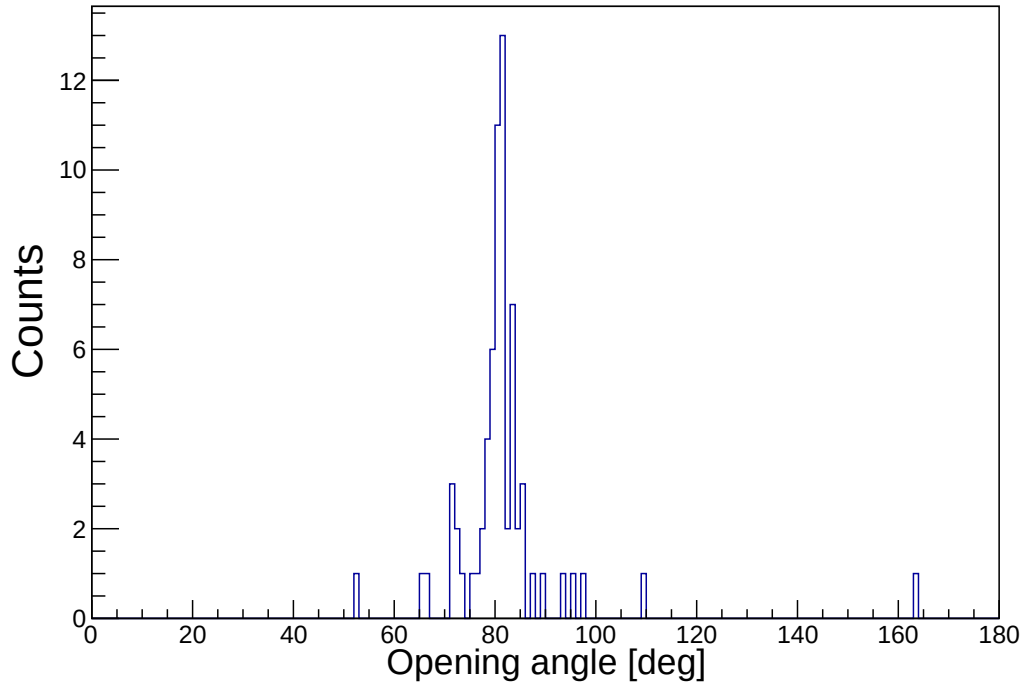

Figure 6.8: Opening angle distribution for the ^{40}Ca(p,2p)^{39}K reaction channel for ^{38}Ca runs on a CH_2 target.

Figure 6.8 shows only the counts for the CH_2 runs. To produce a differential cross section the C and empty target contributions must be subtracted and then the resulting distribution scaled.

6.4 Target Thickness

The number of target centres in both the C and CH_2 have been calculated using two different methods. The first method involved measuring the target thickness with laser measurements and multiplying it by the density value provided by the GSI target lab [53] to estimate the number of scattering centres. The second method utilised energy loss data from the experiment, combined with LISE++ simulations. Table 6.2 presents the results for both targets using these methods.

Name	Thickness from laser (mm)	Density (g/cm^3)	Calculated target centres (cm^{-2})	From energy loss (cm^{-2})
C	10.793	1.84	9.957×10^{22}	9.99×10^{22}
CH_2	24.398	0.94	9.942×10^{22}	1.01×10^{23}

Table 6.2: Number of target centres deduced from thickness measurement with a laser and typical density and ones from energy losses.

It is noted that the number of target centres differs by 0.3% for the C target and 0.7% for the CH_2 target, which represents a very small deviation. Therefore, the value obtained from the laser measurements is used, as it offers higher precision. A systematic uncertainty of 1% is then considered to compensate for this deviation.

6.5 Ion Transmission Through GLAD

PID plots are essential for the selection of reaction channels. Figure 6.9 shows the PID plots for the ^{38}Ca runs. Plots (a), (c) and (e) are the FRS PID plots for empty, C, and CH_2 targets. In red are the cuts used to select each incoming isotope. Plots (b), (d) and (f) are the fragment PID produced when selecting ^{40}Ca.

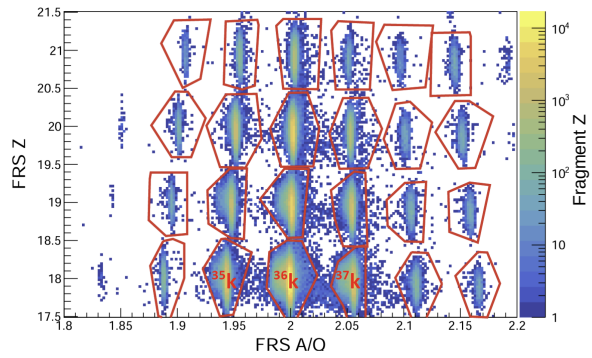

(a) Empty target FRS PID.

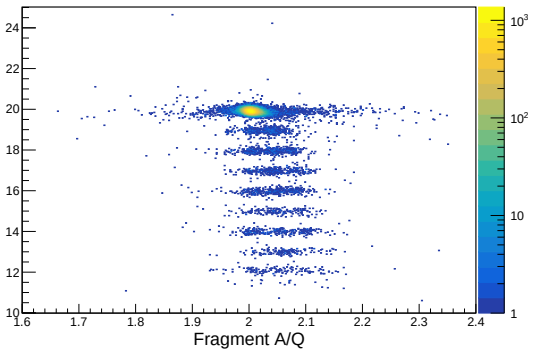

(b) Empty target ^{40}Ca Fragment PID.

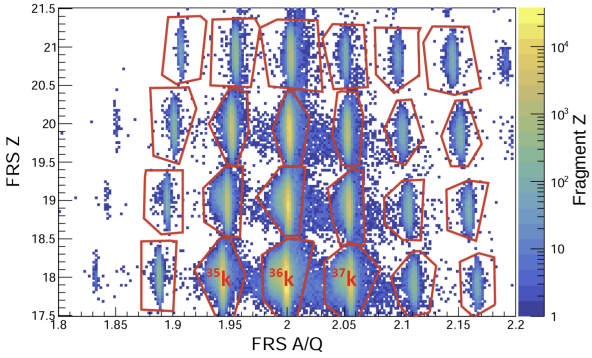

(c) C target FRS PID.

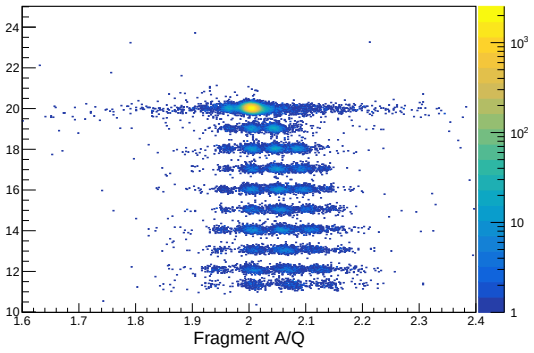

(d) C target ^{40}Ca Fragment PID.

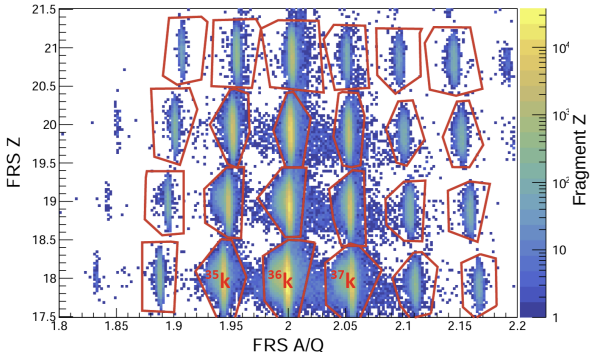

(e) CH_2 target FRS PID.

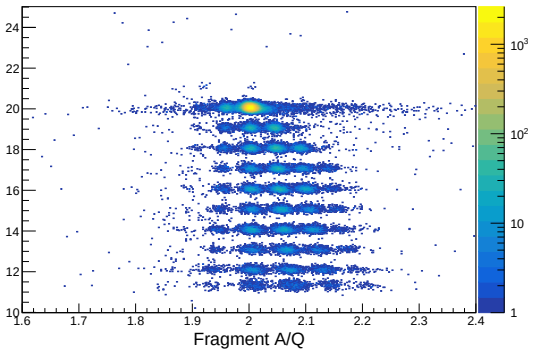

(f) CH_2 target ^{40}Ca Fragment PID.

Figure 6.9: Plots (a), (c) and (e) show the FRS PID plots for the empty, C, and CH_2 targets, respectively, while plots (b), (d) and (f) display the corresponding Fragment PID plots when selecting ^{40}Ca.

Figure 6.9 clearly shows that the isotopes within the FRS PID plots are well separated, such that there is little ambiguity in the selection of the incoming particles. From the ^{40}Ca fragment PID it is clear that the charge changing reaction channels are well resolved, however the one neutron removal channel is less well defined. The number of entries within a cut region gives the number of counts corresponding to the selected cut. By selecting the unreacted channel in the fragment PID for a given ion in the FRS PID the transmission can be calculated for a specific target setting,

$$t_{\text{target}} = \frac{U_{\text{target}}}{I_{\text{target}}}. \tag{6.5.13}$$

As in Chapter 2.4 the symbols U_{target} and I_{target} are defined as the unreacted and incoming beam current on a target for a selected isotope. The uncertainty for the beam transmission is calculated using the formula,

$$\Delta t_{\text{target}} = t_{\text{target}} \left(\left(\frac{\Delta I_{\text{target}}}{I_{\text{target}}} \right)^2 + \left(\frac{\Delta U_{\text{target}}}{U_{\text{target}}} \right)^2 \right)^{\frac{1}{2}} \tag{6.5.14}$$

The transmission has been calculated for all isotopes with high statistics for each target setting and are presented in Tables 6.3,6.4,6.5 and 6.6. These efficiencies are also represented in Figure 6.9 as a function of the mass number of the isotopes for each target setting. The empty target efficiency has a noticeably significant fluctuation in values. This is unexpected, as there are no apparent issues with geometrical acceptance, and all isotopes used in the transmission calculations have lifetimes much longer than the ToF between SofSci and SofToFW. Therefore an average empty efficiency value is calculated for each isotopic chain. In Figure 6.9 the black circles represent the calculated empty transmission, while the pink triangles indicate the corresponding average empty transmission. The red squares represent the transmission probabilities for the C target, while the blue triangles correspond to the transmission probabilities for the CH_2 target.

	^{35}Ar	^{36}Ar	^{37}Ar	^{42}Ar	^{43}Ar	^{44}Ar	^{45}Ar	^{46}Ar
t_{empty} [%]	91.1(5)	92.0(2)	91.8(5)	91.6(8)	91.3(2)	91.1(2)	90.7(4)	89.5(11)
t_{C} [%]	78.9(3)	78.7(1)	78.70(3)	79.0(5)	79.3(1)	79.0(1)	78.5(2)	78.1(7)
t_{CH_2} [%]	72.2(3)	72.0(1)	71.2(3)	70.8(4)	70.7(1)	70.4(1)	70.2(2)	69.7(6)

Table 6.3: Transmission probabilities for the Ar isotopic chain. The mean empty efficiency is calculated to be 91.1(2)%.

	^{37}K	^{38}K	^{39}K	^{45}K	^{46}K	^{47}K	^{48}K
t_{empty} [%]	92.2(8)	92.5(4)	92.5(7)	91.6(3)	91.0(2)	91.0(2)	91.0(7)
t_{C} [%]	78.6(5)	78.5(3)	77.7(4)	79.3(2)	79.0(1)	78.7(1)	77.3(4)
t_{CH_2} [%]	71.3(5)	70.9(2)	70.3(4)	70.5(2)	70.2(1)	69.7(1)	68.7(4)

Table 6.4: Transmission probabilities for the K isotopic chain. The mean empty efficiency is calculated to be 91.6(2)%.

	^{39}Ca	^{40}Ca	^{41}Ca	^{47}Ca	^{48}Ca	^{49}Ca	^{50}Ca
t_{empty} [%]	92.7(7)	93.0(4)	91.7(10)	91.1(9)	90.9(3)	90.7(3)	90.7(6)
t_{C} [%]	78.1(5)	78.1(3)	77.0(7)	79.1(5)	78.7(2)	78.0(2)	77.4(3)
t_{CH_2} [%]	69.9(4)	69.8(2)	69.2(6)	69.4(5)	69.6(2)	68.7(2)	68.1(3)

Table 6.5: Transmission probabilities for the Ca isotopic chain. The mean empty efficiency is calculated to be 91.6(2)%.

	^{42}Sc	^{50}Sc	^{51}Sc	^{52}Sc	^{53}Sc
t_{empty} [%]	92.0(10)	91.1(6)	90.7(3)	90.9(4)	90.6(8)
t_{C} [%]	77.0(7)	78.2(4)	77.8(2)	77.1(2)	76.3(5)
t_{CH_2} [%]	69.0(6)	69.1(3)	68.5(2)	67.9(2)	66.7(5)

Table 6.6: Transmission probabilities for the Sc isotopic chain. The mean empty efficiency is calculated to be 91.1(3)%.

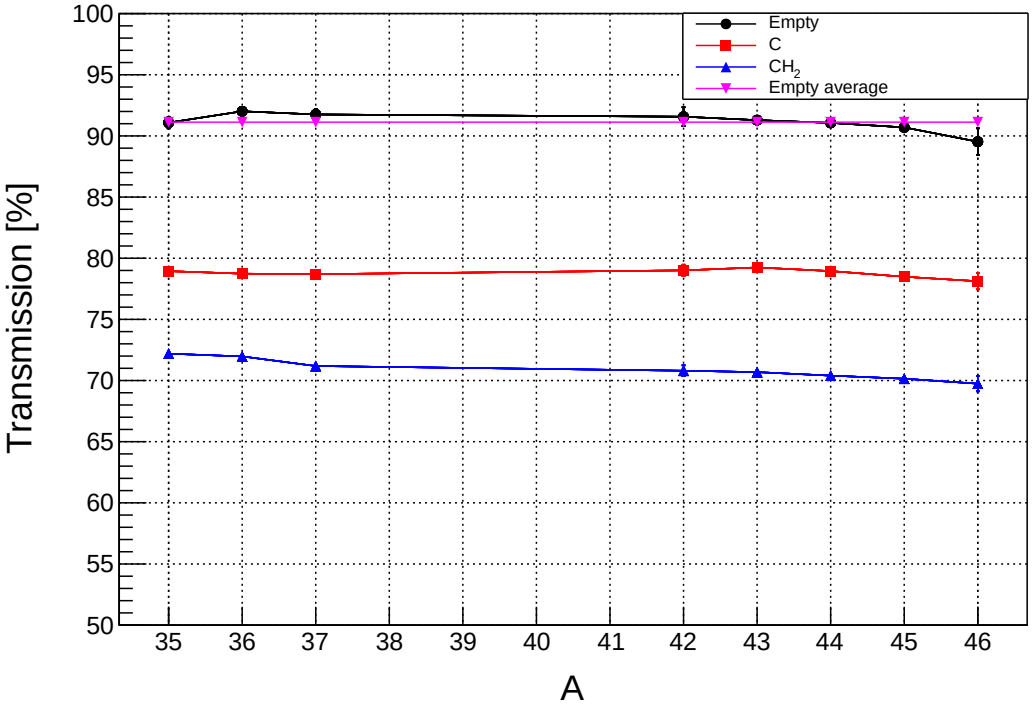

(a) Transmission probabilities for Ar isotopes.

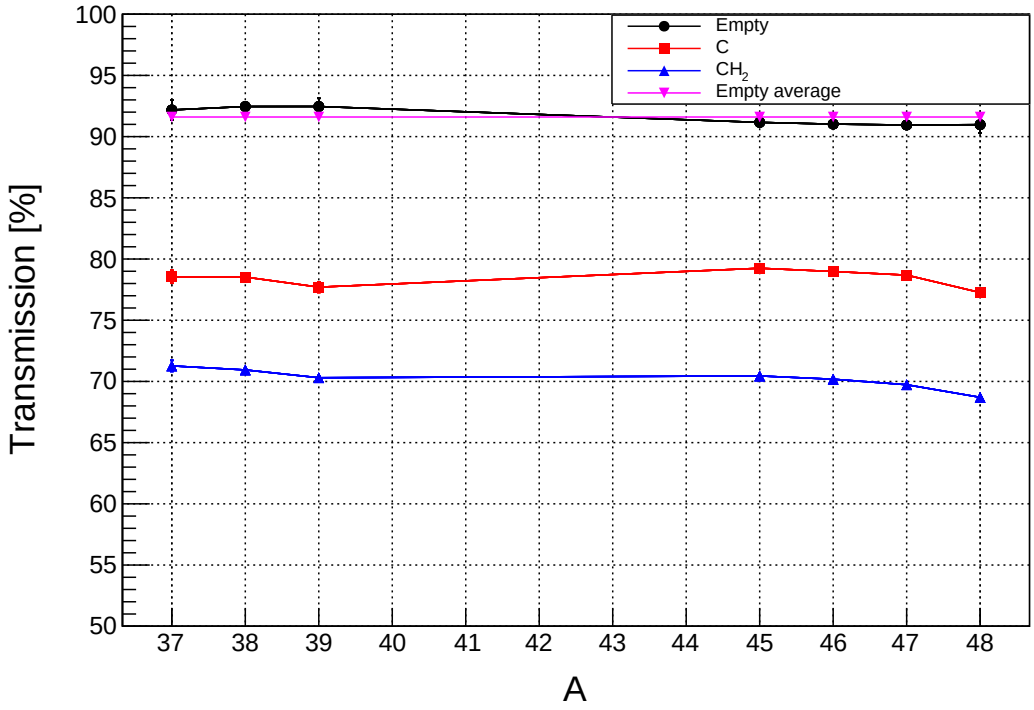

(b) Transmission probabilities for K isotopes.

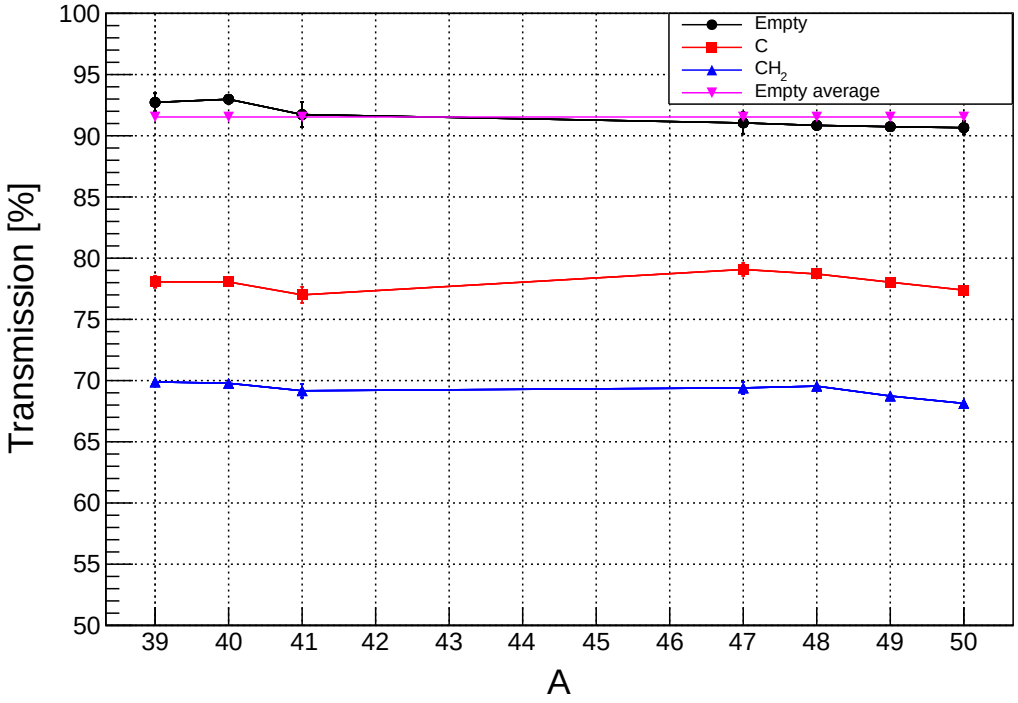

(c) Transmission probabilities for Ca isotopes.

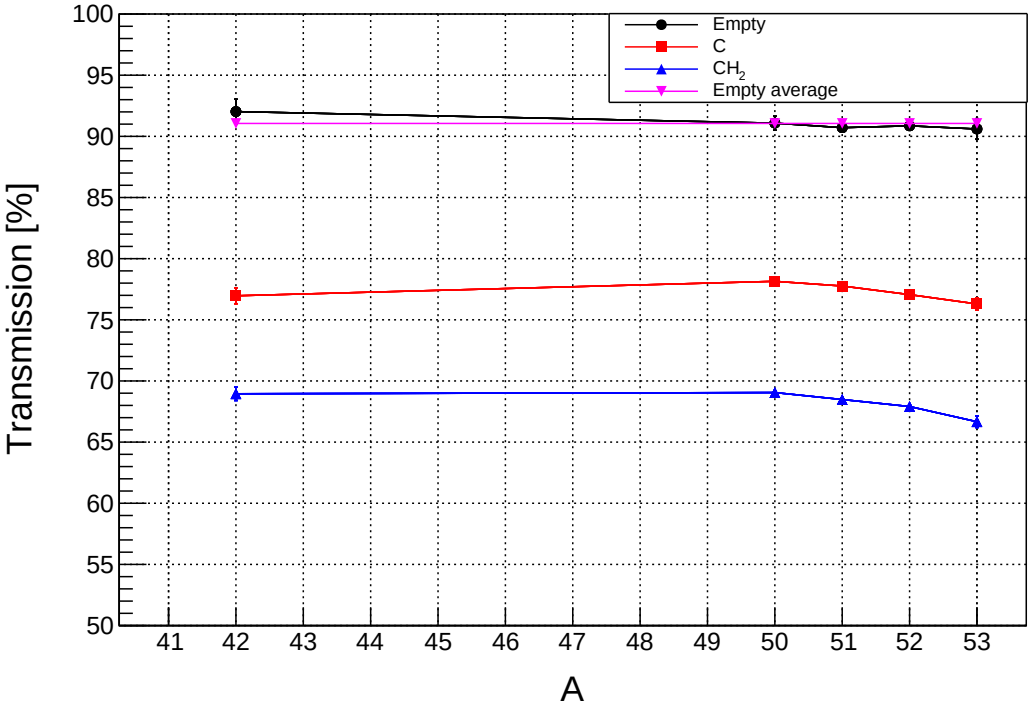

(d) Transmission probabilities for Sc isotopes.

Figure 6.9: Transmission probabilities for isotopic chains in the Ca mass region for C, CH_2 and empty targets. The pink line represents the average empty target transmission.

Chapter 7

Results

In this experiment both C and CH_2 targets were used. For C targets, absorption effects are stronger which concentrates the reactions towards the periphery [54]. While for the CH_2 target the hydrogen allows for the removal of more deeply bound nucleons [54]. Interaction cross sections have been calculated for both target settings and then subtracted to find the hydrogen contribution. One proton removal cross sections have also been calculated for isotopes in the Ca mass region for C and CH_2 targets using the the average empty target transmission. These cross sections have then been subtracted to find the one proton removal cross section for the scattering of hydrogen. One neutron removal cross sections have not been included due to limitations in the fragment PID when separating the unreacted beam from this channel. However, QFS (p,pn) cross sections for Ca isotopes are presented, as the additional condition required by CALIFA for (p,pn) tagging provides a much clearer resolution when selecting the one neutron removal channel in the fragment PID. QFS (p,2p) cross sections have been calculated for the Ca isotopic chain, and the (p,2p) results have been compared to SP theoretical cross sections provided by Carlos Bertulani.

7.1 Interaction Cross Sections

Equation 2.4.47 is used to calculate the interaction cross sections for C and CH_2 targets using the average empty transmission efficiency. These cross sections are

presented in Tables 7.1, 7.2, 7.3 and 7.4.

	^{35}Ar	^{36}Ar	^{37}Ar	^{42}Ar	^{43}Ar	^{44}Ar	^{45}Ar	^{46}Ar
$\sigma_{\text{Interaction}}$(C) [barn]	1.40(5)	1.47(3)	1.47(5)	1.43(6)	1.40(3)	1.44(3)	1.50(4)	1.55(9)
$\sigma_{\text{Interaction}}(CH_2)$ [barn]	2.36(4)	2.40(3)	2.51(4)	2.56(7)	2.58(3)	2.62(3)	2.66(4)	2.72(9)
$\sigma_{\text{Interaction}}$(H) [barn]	0.48(3)	0.46(2)	0.52(3)	0.57(5)	0.59(2)	0.59(2)	0.58(3)	0.58(6)

Table 7.1: Interaction cross sections for the Ar isotopic chain.

	^{37}K	^{38}K	^{39}K	^{45}K	^{46}K	^{47}K	^{48}K
$\sigma_{\text{Interaction}}$(C) [barn]	1.54(7)	1.55(4)	1.65(6)	1.46(3)	1.49(3)	1.53(3)	1.71(6)
$\sigma_{\text{Interaction}}(CH_2)$ [barn]	2.55(7)	2.60(4)	2.69(6)	2.67(3)	2.70(3)	2.77(3)	2.92(6)
$\sigma_{\text{Interaction}}$(H) [barn]	0.50(5)	0.52(3)	0.52(4)	0.61(2)	0.61(2)	0.62(2)	0.61(3)

Table 7.2: Interaction cross sections for the K isotopic chain.

	^{39}Ca	^{40}Ca	^{41}Ca	^{47}Ca	^{48}Ca	^{49}Ca	^{50}Ca
$\sigma_{\text{Interaction}}$(C) [barn]	1.60(7)	1.60(4)	1.74(9)	1.47(7)	1.52(4)	1.60(3)	1.69(5)
$\sigma_{\text{Interaction}}(CH_2)$ [barn]	2.74(7)	2.76(4)	2.84(9)	2.81(8)	2.79(4)	2.91(4)	3.00(5)
$\sigma_{\text{Interaction}}$(H) [barn]	0.57(5)	0.58(3)	0.55(6)	0.67(5)	0.63(3)	0.65(2.5)	0.66(4)

Table 7.3: Interaction cross sections for the Ca isotopic chain.

	^{42}Sc	^{50}Sc	^{51}Sc	^{52}Sc	^{53}Sc
$\sigma_{\text{Interaction}}$(C) [barn]	1.69(9)	1.54(6)	1.58(4)	1.68(4)	1.78(7)
$\sigma_{\text{Interaction}}CH_2$ [barn]	2.82(9)	2.81(6)	2.89(4)	2.98(5)	3.17(8)
$\sigma_{\text{Interaction}}$(H) [barn]	0.57(6)	0.64(4)	0.65(3)	0.65(3)	0.70(5)

Table 7.4: Interaction cross sections for the Sc isotopic chain.

The interaction cross section for the scattering on hydrogen is calculated using,

$$\sigma_{\text{Interaction}}(\text{H}) = \frac{1}{2}\left(\sigma_{\text{Interaction}}(\text{CH}_2) - \sigma_{\text{Interaction}}(\text{C})\right). \tag{7.1.1}$$

The corresponding error is propagated to be,

$$\Delta\sigma_{\text{Interaction}}(\text{H}) = \frac{1}{2}\left((\Delta\sigma_{\text{Interaction}}(\text{CH}_2))^2 + (\Delta\sigma_{\text{Interaction}}(\text{C}))^2\right)^{\frac{1}{2}}. \tag{7.1.2}$$

Using the Kox parametrization [55] the interaction cross section for scattering on hydrogen for Ar, K, Ca and Sc isotopes have been calculated and are presented

along with the corresponding experimental results from Tables 7.1, 7.2, 7.3 and 7.4. This is shown in Figure 7.1 where red points indicate experimental results and black points show interaction cross sections estimated by the Kox parametrization.

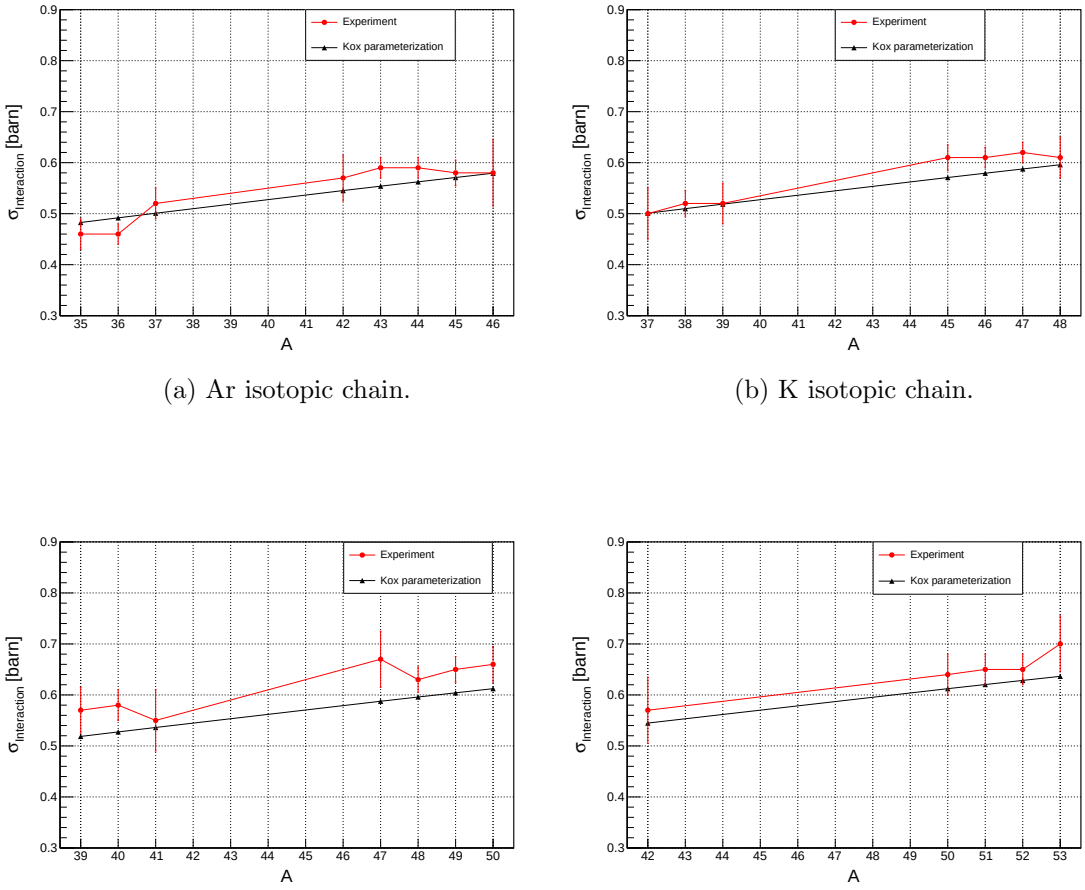

(a) Ar isotopic chain.

(b) K isotopic chain.

(c) Ca isotopic chain.

(d) Sc isotopic chain.

Figure 7.1: Interaction cross sections from experimental data (red) with statistical error bars shown and calculated cross section from the Kox parametrization (black).

As can be seen in Figure 7.1 the experimental data follows the expected $A^{1/3}$ trend as the nucleus size increases. The Kox parametrization also captures well the overall trend, however it lacks the specific nuclear structure of each isotope.

7.2 One Proton Removal Cross Sections

The inclusive one proton removal reactions that lead to a bound A-1 daughter nucleus are extracted for the Ar, K, Ca and Sc isotopic chains. Cross sections are presented in Tables 7.5,7.6,7.7 and 7.8 for scattering on C and CH_2 and the subtracted H target. Equation 2.4.55 is used to calculate the one proton removal cross section for the CH_2 and C targets. The efficiency term ϵ of equation 2.4.55 is taken to be,

$$\epsilon = \frac{\epsilon_{\text{empty}} + t_{\text{target}}}{2.}. \tag{7.2.3}$$

Where ϵ_{empty} is the empty target average and t_{target} the transmission probability for an incoming ion. The one proton removal cross section induced by scattering off of hydrogen is calculated using,

$$\sigma_{-1p}(\text{H}) = \frac{1}{2}\left(\sigma_{-1p}(\text{CH}_2) - \sigma_{-1p}(\text{C})\right). \tag{7.2.4}$$

The corresponding error is propagated to be,

$$\Delta\sigma_{-1\text{p}}(\text{H}) = \frac{1}{2}\left((\Delta\sigma_{-1\text{p}}(\text{CH}_2))^2 + (\Delta\sigma_{-1\text{p}}(\text{C}))^2\right)^{\frac{1}{2}}. \tag{7.2.5}$$

	^{35}Ar	^{36}Ar	^{37}Ar	^{42}Ar	^{43}Ar	^{44}Ar	^{45}Ar
σ_{-1p}(C)[mbarn]	83(3)	78(1)	66(3)	49(4)	27(1)	27(1)	18(1)
σ_{-1p}(CH_2)[mbarn]	136(3)	141(2)	115(3)	76(5)	49(1)	51(1)	39(2)
σ_{-1p}(H) [mbarn]	26(2)	32(1)	24(2)	14(3)	11(1)	12(1)	11(2)

Table 7.5: Ar one proton removal cross sections.

	^{37}K	^{38}K	^{39}K	^{45}K	^{46}K	^{47}K
σ_{-1p}(C) [mbarn]	101(5)	82(2)	95(4)	33(1)	20(1)	20(1)
σ_{-1p}(CH_2) [mbarn]	166(6)	146(3)	147(5)	52(2)	34(1)	37(1)
σ_{-1p}(H) [mbarn]	33(4)	32(2)	26(3)	10(1)	7(1)	8(1)

Table 7.6: K one proton removal cross sections.

	^{39}Ca	^{40}Ca	^{41}Ca	^{48}Ca	^{49}Ca	^{50}Ca
σ_{-1p}(C) [mbarn]	81(4)	89(2)	81(6)	38(1)	24(1)	27(2)
σ_{-1p}(CH_2)[mbarn]	142(5)	156(3)	152(8)	69(2)	45(1)	42(2)
σ_{-1p}(H) [mbarn]	31(3)	34(3)	35(7)	15(1)	10(1)	8(1)

Table 7.7: Ca one proton removal cross sections.

	^{50}Sc	^{51}Sc	^{52}Sc
σ_{-1p}(C) [mbarn]	29(2)	20(1)	7(1)
σ_{-1p}(CH_2)[mbarn]	47(3)	36(1)	13(1)
σ_{-1p}(H) [mbarn]	9(2)	8(1)	3(1)

Table 7.8: Sc one proton removal cross sections.

The values in Tables 7.5,7.6,7.7 and 7.8 are also then presented in Figure 7.2 as a function of mass number A.

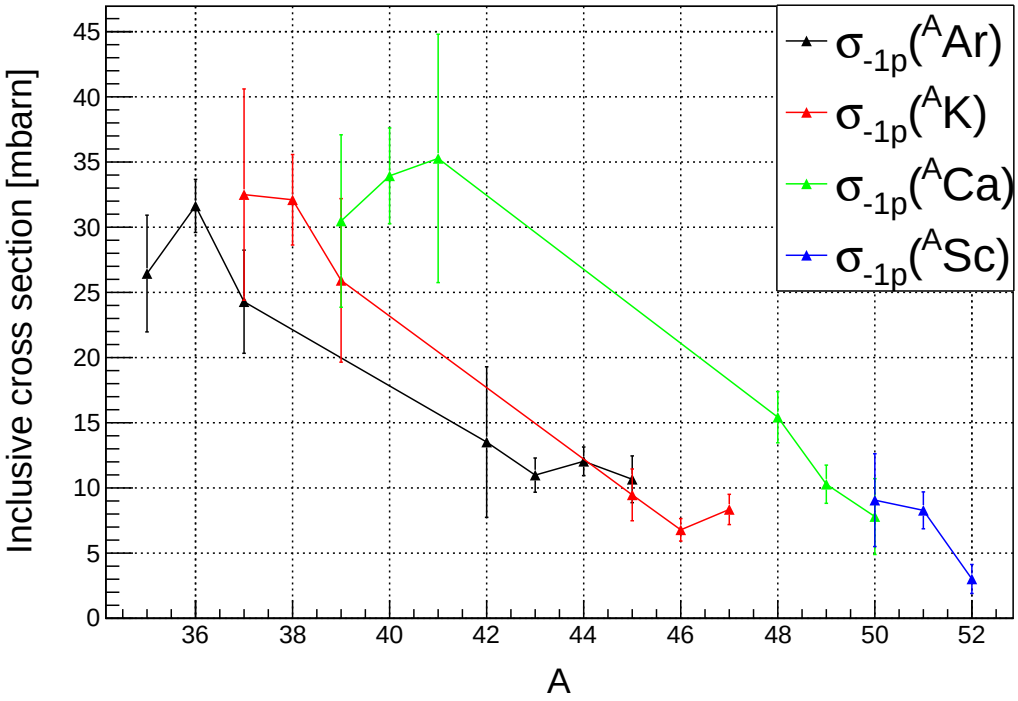

Figure 7.2: Inclusive one-proton removal cross sections to a bound A-1 daughter system for various isotopes in the Ca mass region.

The overall trend in Figure 7.2 is well expected as the protons are more and more deeply bound as one moves towards the more neutron rich nuclei. Being more deeply bound means that their separation energy is larger and the proton's wavefunction is more concentrated in the interior of the nucleus. Additionally, the excess neutrons are expected to enhance the absorption of the scattered proton, potentially leading to secondary reactions and an unbound daughter nucleus. Since the cross-section measurement requires the A-1 system to remain bound, such events are excluded.

Which could lead to an underestimation of the total cross-section and impact the interpretation of reaction mechanisms in neutron-rich systems. While in many cases the error bars are relatively too large to allow for a more detailed nuclear structure discussion, there are a few clear cases which require further consideration. For example, one proton removal cross sections for ^{51}Sc is at least a factor two larger than that of ^{52}Sc. This cross sections is very sensitive to the Z=20 shell gap, which in this mass region is 5.5 MeV and relatively constant [4]. The large difference between the two isotopes can be attributed to their specific proton-separation thresholds: 4.8 MeV for ^{51}Ca compared to 6.3 MeV for ^{50}Ca. In the case of ^{51}Ca, only weakly bound protons near the separation threshold contribute to the cross-section (which requires a bound daughter system). In contrast, for ^{50}Ca, contributions from more deeply bound protons are also present, leading to a higher cross-section.

7.3 QFS (p,2p) Cross Sections

Conditions described in Chapter 5 and 6 for the tagging of protons of CALIFA are used and corresponding FRS PID and Fragment PID are produced. Cuts are then made to the PID plots such that the number of: one proton removal, incoming beam and unreacted beam events can be counted. Using equation 2.4.55 the QFS (p,2p) cross section can be calculated where the efficiency is given by,

$$\epsilon = \frac{\epsilon_{\mathrm{CALIFA}}(p,2p)\,(\epsilon_{\mathrm{empty}} + t_{\mathrm{target}})}{2.}. \tag{7.3.6}$$

Here $\epsilon_{\mathrm{CALIFA}}(p,2p)$ is the geometrical efficiency of CALIFA for a (p,2p) reaction which has been calculated through simulation to be 18.2%. Values for the cross sections for the Ar, K and Ca isotopic chains are presented in Tables 7.9, 7.10 and 7.11 respectively. For each target setting, the reconstructed opening angle of protons measured by CALIFA is plotted against the corresponding count values. These plots are then processed by subtracting the contributions from the carbon and empty runs. The resulting data is scaled to represent the differential cross section as a function of the opening angle. Figure 7.3 shows (p,2p) opening angle distributions for four different Ca isotopes. In blue is the experimental data and in red is the scaled distribution from simulation.

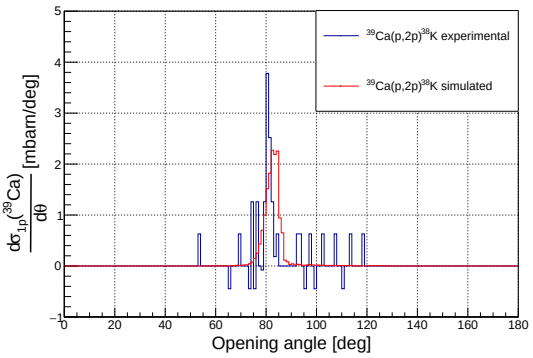

(a) ^{39}Ca(p,2p)^{38}K reaction channel.

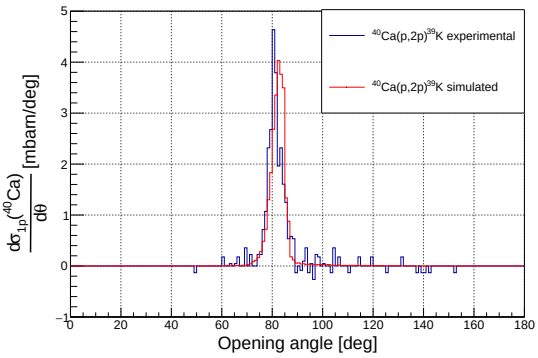

(b) ^{40}Ca(p,2p)^{39}K reaction channel.

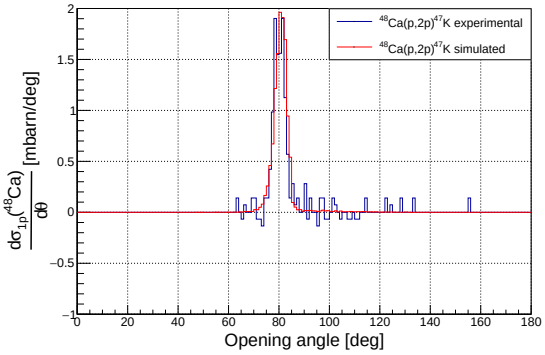

(c) ^{48}Ca(p,2p)^{47}K reaction channel.

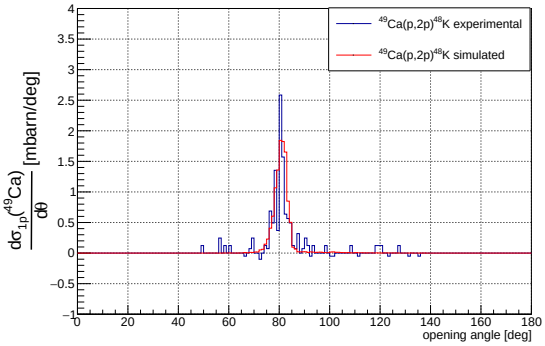

(d) ^{49}Ca(p,2p)^{48}K reaction channel.

Figure 7.3: Experimental QFS (p,2p) cross sections for Ca isotopes (blue) and the equivalent simulation used (red).

	^{35}Ar	^{36}Ar	^{37}Ar	^{43}Ar	^{44}Ar	^{45}Ar
σ(p,2p)$_{\text{exp}}$ [mbarn]	15±2	22±1	17±2	12±1	12±1	9± 1

Table 7.9: QFS (p,2p) cross sections for Ar isotopes.

	^{37}K	^{38}K	^{39}K	^{45}K	^{46}K	^{47}K
σ(p,2p)$_{\text{exp}}$ [mbarn]	20±4	23±2	25±4	11±1	9±1	9±1

Table 7.10: QFS (p,2p) cross sections for K isotopes.

From Table 7.6 neutron rich isotopes such as ^{46}K and ^{47}K have slightly larger cross sections than that of one proton removal (1 mbarn larger). This is originating

from the CALIFA efficiency used in the calculation of these cross sections overcompensating, therefore the systematic error to account for this is required which is discussed in section 7.5. Table 7.11 shows the experimental results of QFS (p,2p) of Ca isotopes. Theoretical single particle cross sections for the *sd* shell have been calculated using the Eikonal model.

	^{39}Ca	^{40}Ca	^{41}Ca	^{48}Ca	^{49}Ca	^{50}Ca
$\sigma(p,2p)_{exp}$ [mbarn]	19±3	29±2	25±5	14±1	12±1	14±3
$\sigma\left(1d\frac{5}{2}\right)_{sp}$ [mbarn]	2.942	2.564	2.369	2.130	1.993	1.867
$\sigma\left(2s\frac{1}{2}\right)_{sp}$ [mbarn]	3.313	2.820	2.594	2.285	2.127	1.981
$\sigma\left(1d\frac{3}{2}\right)_{sp}$ [mbarn]	2.700	2.361	2.180	1.951	1.828	1.714
$\sigma(p,2p)_{\mathrm{th}}$ [mbarn]	35.077	30.469	28.123	25.151	23.525	22.018
R	0.5±0.1	0.9±0.1	0.9±0.2	0.6±0.1	0.5±0.1	0.6±0.1
S_p^{proj} [MeV]	5.771	8.328	8.891	15.801	16.305	17.267
S_n^{proj} [MeV]	13.295	15.635	8.362	9.951	5.146	6.361
S_p^{frag} [MeV]	5.142	6.381	7.582	13.229	14.206	14.546
S_n^{frag} [MeV]	12.071	13.077	7.799	8.369	4.643	5.398

Table 7.11: Ca QFS (p,2p) cross sections with theoretical single particle cross sections and the resulting total theoretical cross section. Values for proton and neutron separation energies for both projectile and fragment nuclei taken from [48].

By applying equation 2.1.23 to the single particle cross sections assuming that protons are only removed from the *sd* shell and that the occupation of each orbital is the maximum predicted by the IPM, total theoretical cross sections are calculated and presented in Table 7.11. Shells below *sd* such as *pf* are not considered as protons removed from such a deeply bound state would leave the nucleus in a highly excited state and are assumed to be unbound. Reduction factors are then calculated using equation 1.0.1 and presented in Figure 7.4 as a function of nuclear asymmetry δ,

$$\delta = \frac{\mathrm{N}-\mathrm{Z}}{\mathrm{N}+\mathrm{Z}} = \frac{\mathrm{N}-\mathrm{Z}}{\mathrm{A}}. \tag{7.3.7}$$

Where N is the number of neutrons, Z is the number of protons and A is the mass number.

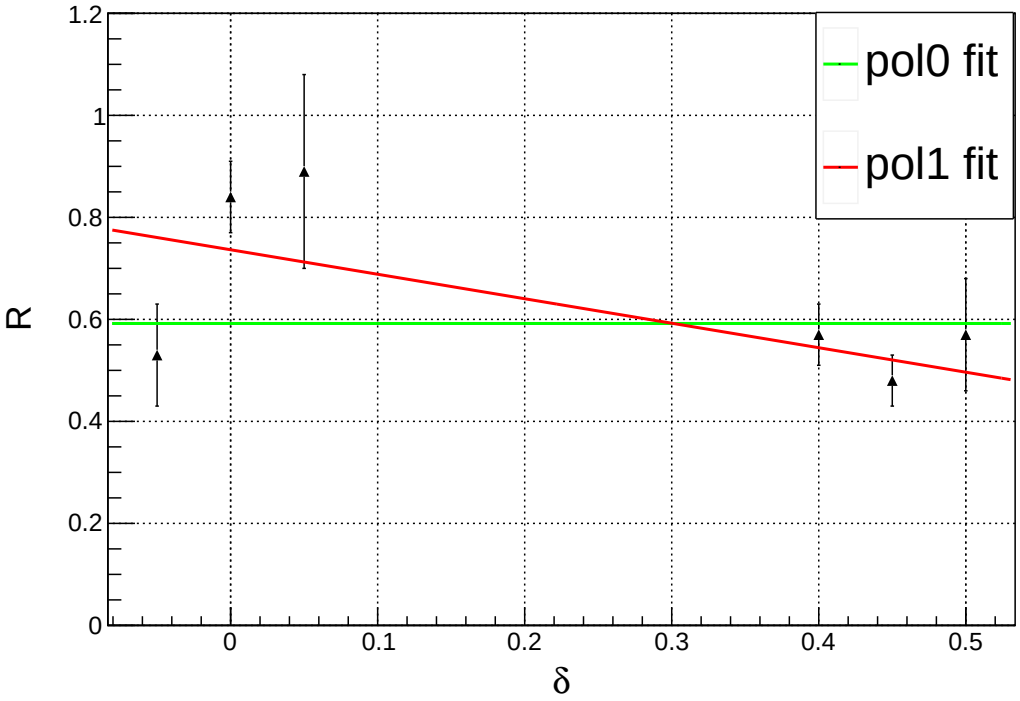

Figure 7.4: Reduction factor R for QFS (p,2p) reactions of Ca as a function of nuclear asymmetry, δ (black points). Here only statistical errors are included.

From Figure 7.4 preliminary calculated reduction factors show a very weak correlation with nuclear asymmetry, which is consistent with previous results for QFS using light nuclei [14].

7.3.1 Momentum Distributions

Using information from tracking it is possible to calculate the momentum distributions in both the x and y direction of the scattering plane. This can then be compared to the available theoretically calculated single particle x-transverse momentum distributions provided by Carlos Bertulani. Figure 7.5 shows the *sd* shell single particle transverse momentum distributions for the ^{40}Ca(p,2p)^{39}K reaction channel. This distribution is the same in both x and y therefore when comparing to experimental data the x distribution is used due to the higher position resolution from the MWPC.

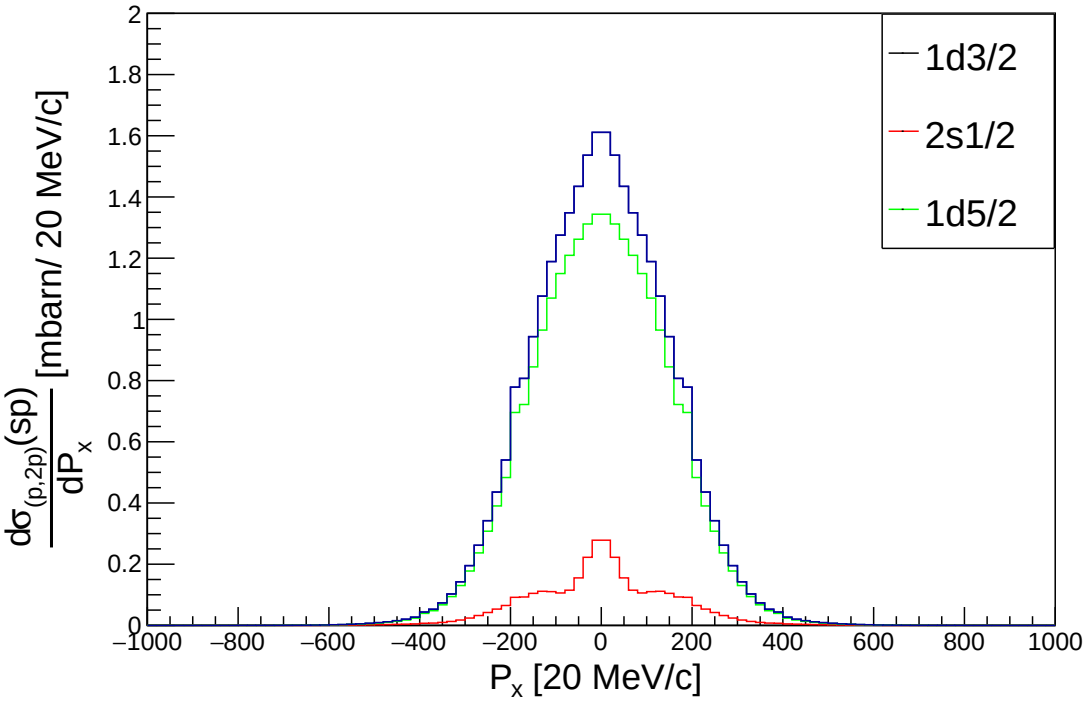

Figure 7.5: Theoretical SP transverse momentum distributions for the ^{40}Ca(p,2p)^{39}K reaction channel. Each orbital from the *sd* shell is scaled by considering the IPM.

Figure 7.6 shows the sum of the single particle transverse momentum distributions for the ^{40}Ca(p,2p)^{39}K reaction channel,

$$\frac{d\sigma}{d\mathrm{P}_x} = \sum_i \frac{d\sigma^i_{sp}}{d\mathrm{P}_i}(2S_i + 1). \tag{7.3.8}$$

Where each SP state has been scaled by the maximum spectroscopic factor, S_i when applying the IPM. In pink is the experimentally calculated distribution and in black the theoretical calculated distribution. The theoretical distribution has been folded with a Gaussian distribution with momentum spread of 60 mbarn MeV/c to reflect the resolution of the MWPC.

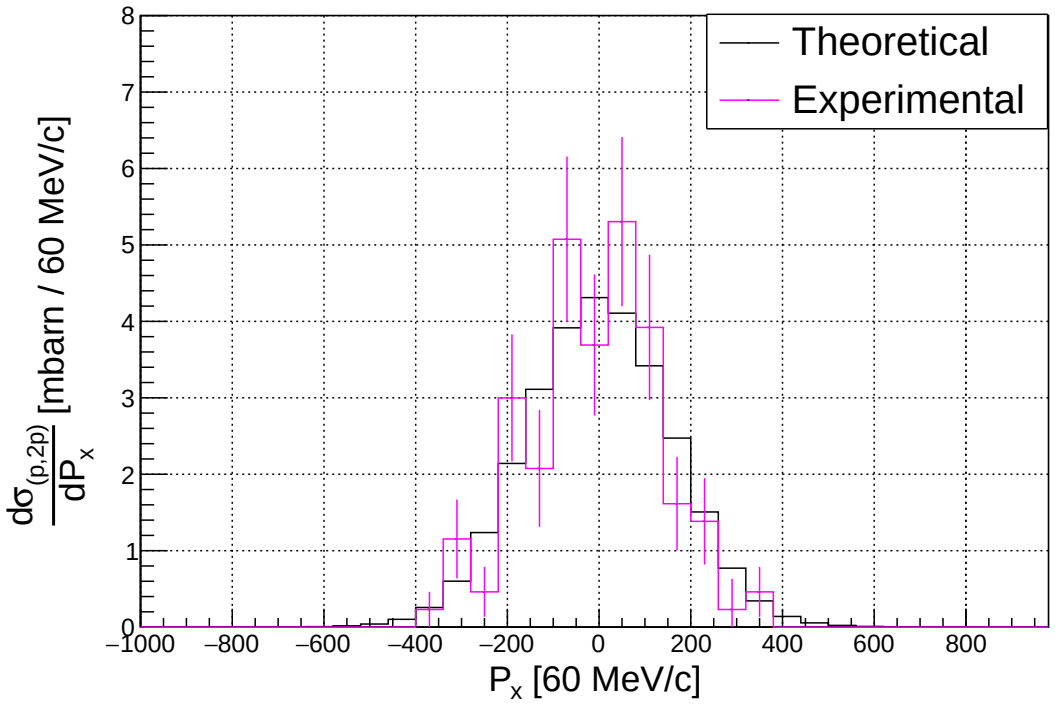

Figure 7.6: Distributions from Figure 7.5 for the ^{40}Ca(p,2p)^{39}K reaction channel are summed and compared to experimental data.

Theoretically calculated SP distributions were also available for the ^{48}Ca(p,2p)^{47}K reaction channel and are presented in Figure 7.7.

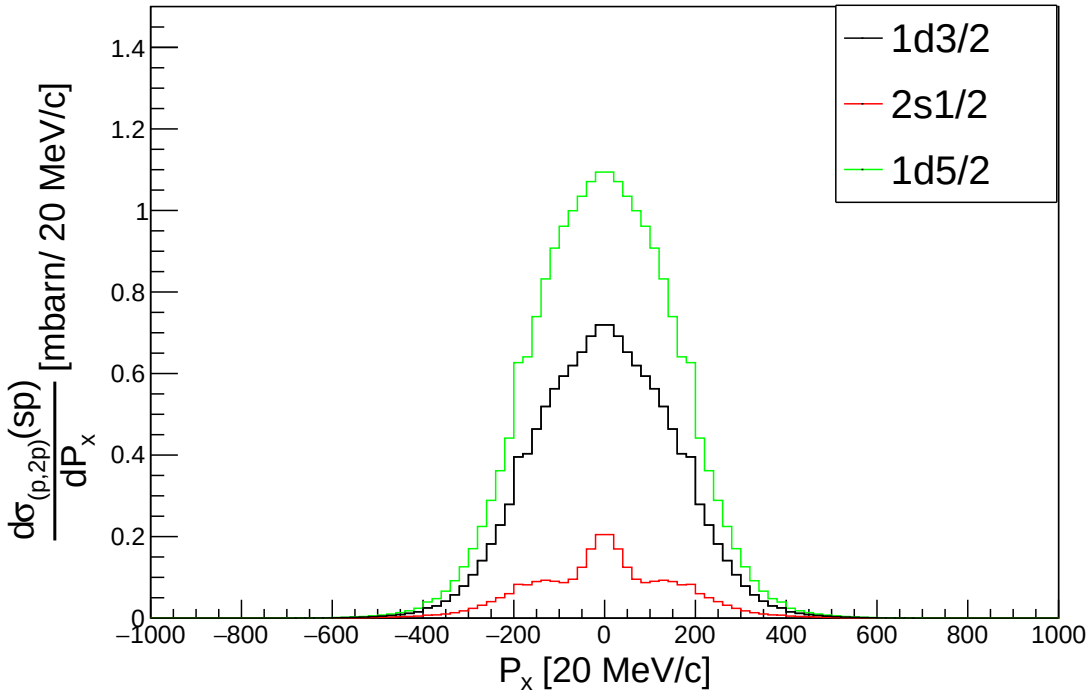

Figure 7.7: Theoretical SP transverse momentum distributions for the ^{48}Ca(p,2p)^{47}K reaction channel. Each orbital from the *sd* shell is scaled by considering the IPM.

Each distribution in Figure 7.7 is summed by considering the IPM and is show in Figure 7.7. The experimental distribution is shown in pink and the theoretically calculated distribution in black.

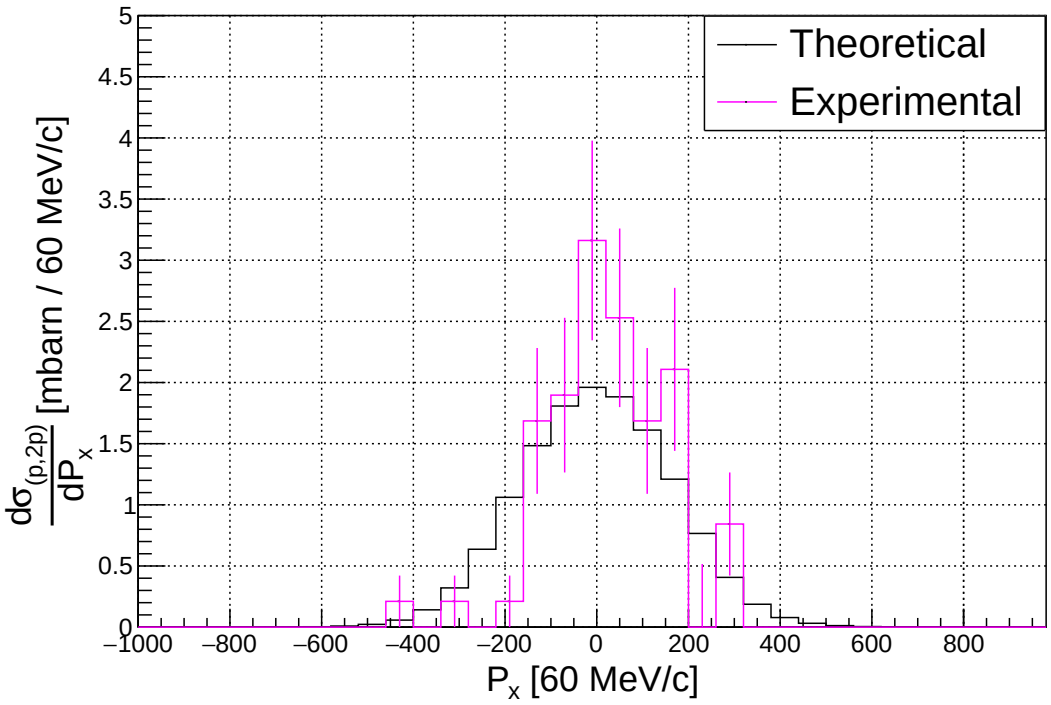

Figure 7.8: Distributions from Figure 7.7 for the ^{48}Ca(p,2p)^{47}K reaction channel are summed and compared to experimental data.

For all other (p,2p) reaction channels theoretical calculations were not available at this time, however, the momentum spread of the transverse momentum distributions are presented in Tables 7.12, 7.13 and 7.14 along with the values for ^{40}Ca and ^{48}Ca.

	^{35}Ar	^{36}Ar	^{37}Ar	^{42}Ar	^{43}Ar	^{44}Ar	^{45}Ar
$\sigma(P_X)$ [60 MeV/c]	128(12)	142(5)	136(13)	103(20)	135(9)	144(8)	123(15)

Table 7.12: Momentum spread for the x-transverse component for Ar isotopes.

	^{37}K	^{38}K	^{39}K	^{45}K	^{46}K	^{47}K
$\sigma(P_X)$ [60 MeV/c]	108(16)	129(8)	133(13)	130(12)	124(8)	142(11)

Table 7.13: Momentum spread for the x-transverse component for K isotopes.

	^{39}Ca	^{40}Ca	^{41}Ca	^{48}Ca	^{49}Ca	^{50}Ca
$\sigma(P_X)$ [60 MeV/c]	163(22)	142(8)	124(19)	136(10)	133(10)	98(13)

Table 7.14: Momentum spread for the x-transverse component for Ca isotopes.

The distributions that the momentum spread is calculated from is show in Figures 7.9,7.10 and 7.11 for the Ar, K and Ca nuclei respectively.

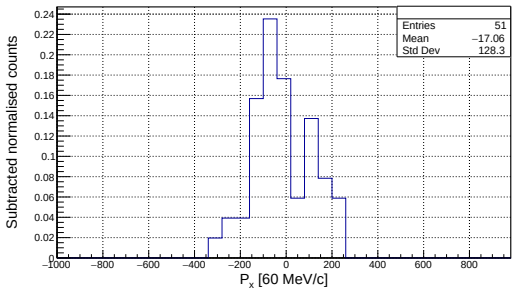

(a) ^{35}Ar(p,2p)^{34}Cl.

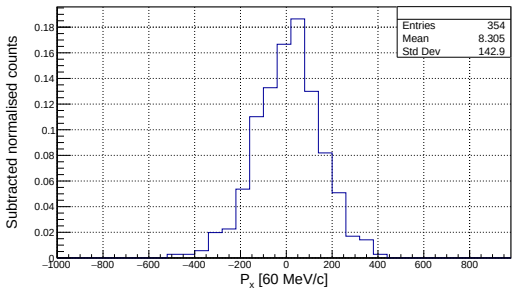

(b) ^{36}Ar(p,2p)^{35}Cl.

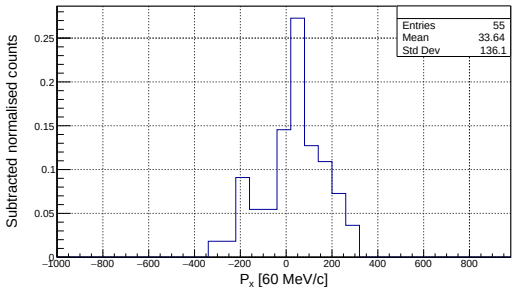

(c) ^{37}Ar(p,2p)^{36}Cl.

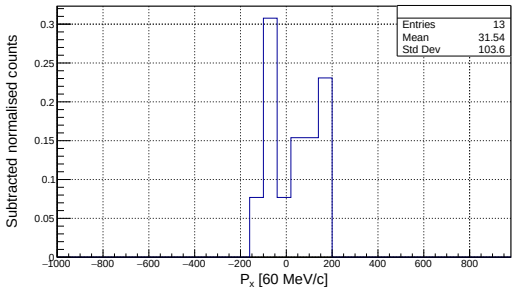

(d) ^{42}Ar(p,2p)^{41}Cl.

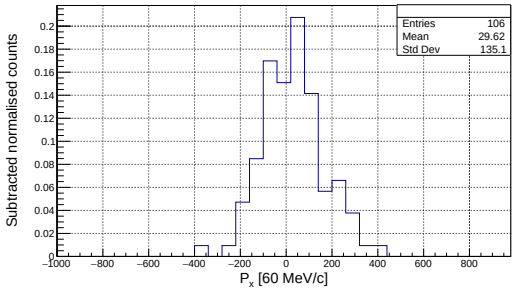

(e) ^{43}Ar(p,2p)^{42}Cl.

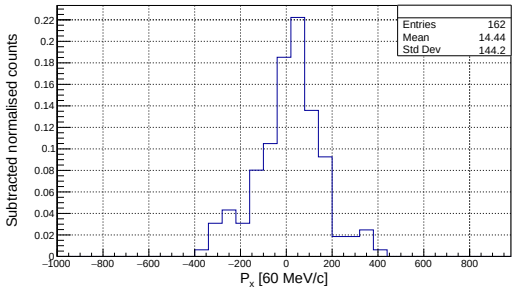

(f) ^{44}Ar(p,2p)^{43}Cl.

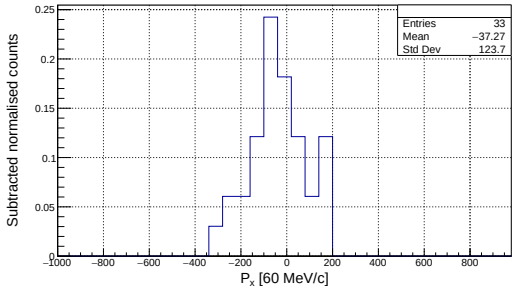

(g) ^{45}Ar(p,2p)^{44}Cl.

Figure 7.9: P$_x$ momentum distributions for (p,2p) reactions of Ar isotopes.

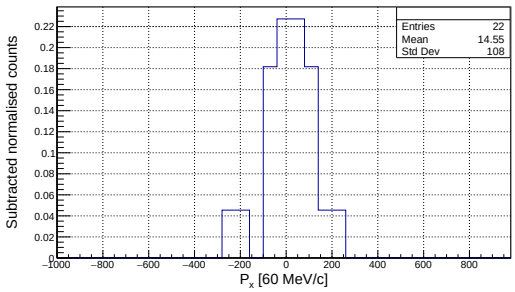

(a) ^{37}K(p,2p)^{36}Ar.

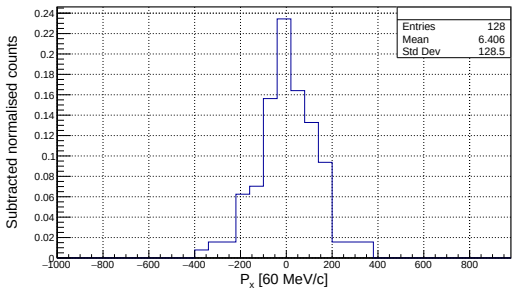

(b) ^{38}K(p,2p)^{37}Ar.

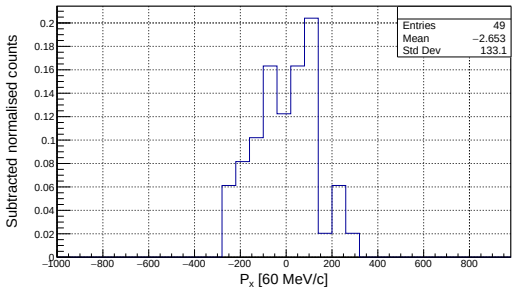

(c) ^{39}K(p,2p)^{38}Ar.

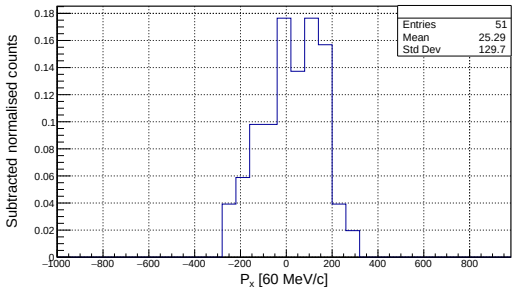

(d) ^{45}K(p,2p)^{44}Ar.

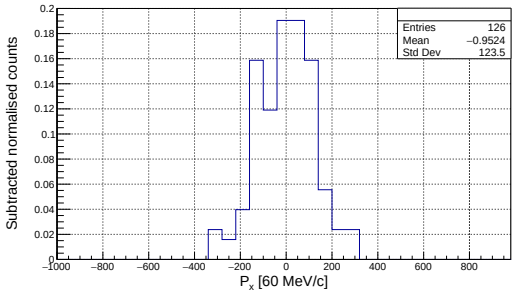

(e) ^{46}K(p,2p)^{45}Ar.

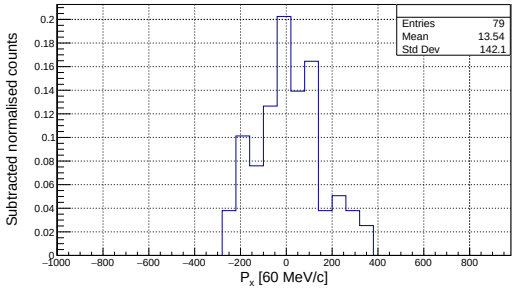

(f) ^{47}K(p,2p)^{46}Ar.

Figure 7.10: P_x momentum distributions for (p,2p) reactions of K isotopes.

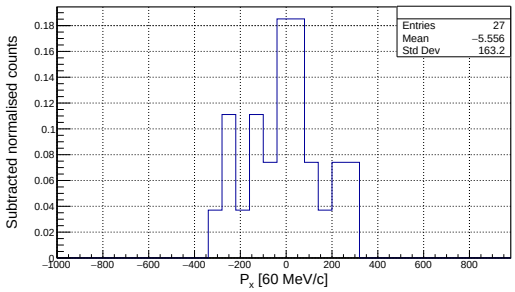

(a) ^{39}Ca(p,2p)^{38}K.

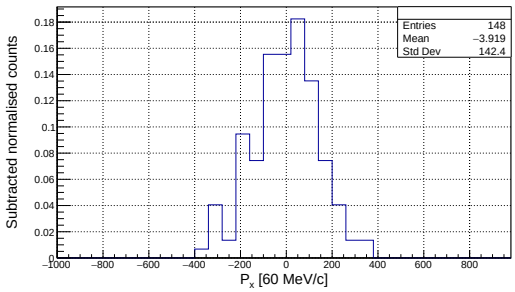

(b) ^{40}Ca(p,2p)^{39}K.

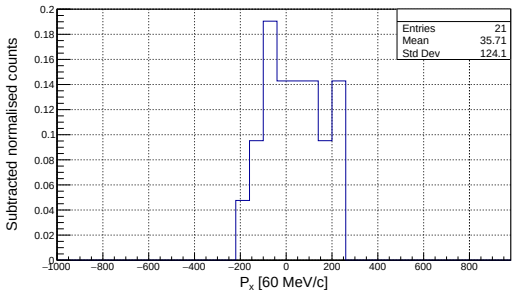

(c) ^{41}Ca(p,2p)^{40}K.

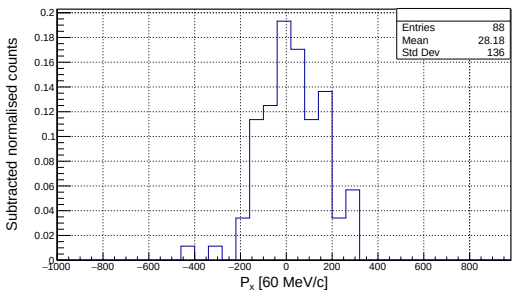

(d) ^{48}Ca(p,2p)^{47}K.

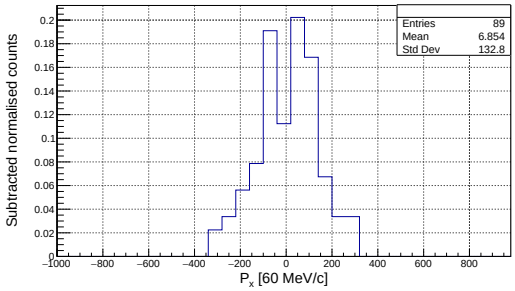

(e) ^{49}Ca(p,2p)^{48}K.

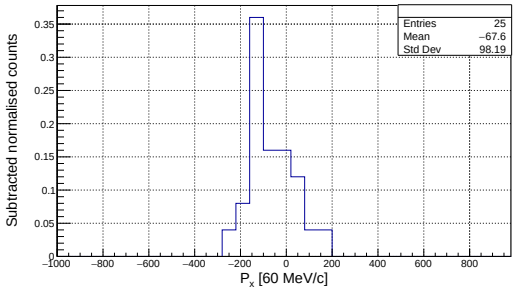

(f) ^{50}Ca(p,2p)^{49}K.

Figure 7.11: P$_x$ momentum distributions for (p,2p) reactions of Ca isotopes.

Figure 7.12 shows the results from Tables 7.12, 7.13 and 7.14 as a function of mass number.

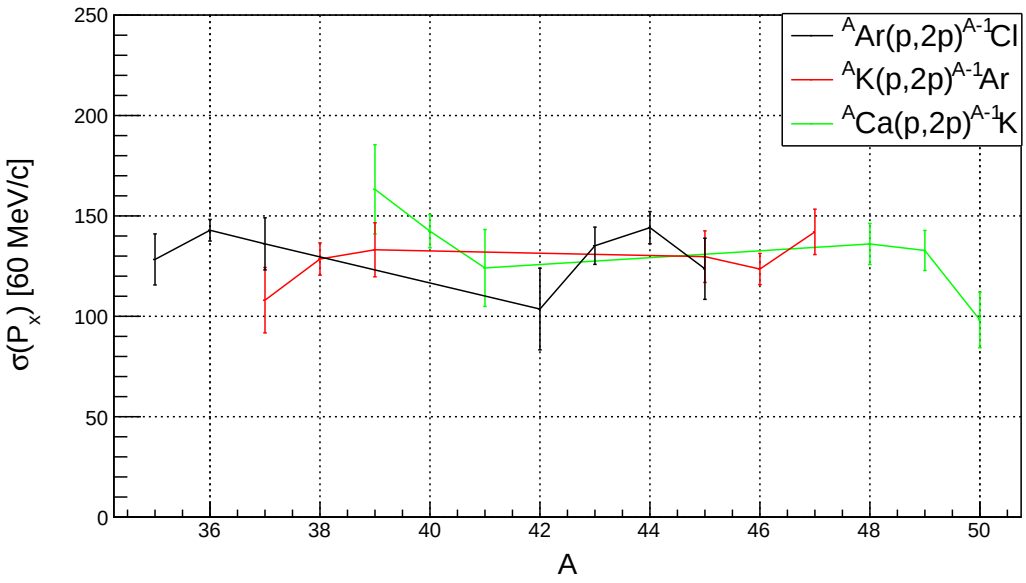

Figure 7.12: Transverse momentum spread for QFS (p,2p) reactions.

From Figure 7.12 a weakly decreasing trend is seen for the Ca isotopic chain, all other chains show a very constant correlation. In chapter 5, a value of 120 MeV/c was estimated for the simulation studies. This value was extrapolated from fits performed using ^{48}Ca and as can be seen, this value aligns well with what has been calculated experimentally.

7.4 QFS (p,pn) Cross Sections

Using conditions described in Chapter 5 and 6 cuts involving CALIFA are applied and PID plots are produced. The incoming and unreacted beam are counted, as well as the one-neutron removal channel, which now has sufficient resolution to be counted. The reconstruction is made more complex as the interactions of neutrons within CALIFA is not completely defined. Among the various models developed in Geant4 is the QGSP BERT EMV, which is suitable for simulations of protons, neutrons, pions and kanos below 10 GeV. This model was used for the simulation of neutron interaction within CALIFA and the resulting (p,pn) efficiency. Cross sections are calculated using equation 2.4.55 where $R_{reaction}$ is the number of (p,pn) events counted in the fragment PID. The CALIFA efficiency for (p,pn) detection,

$\epsilon_{\mathrm{CALIFA}}(p,pn)$, was calculated in Chapter 5 to be 12.7%. This efficiency is higher than expected, however, it has been used for preliminary calculations. The QFS (p,pn) cross sections is calculated using equation 2.4.55 with an efficiency of,

$$\epsilon = \frac{\epsilon_{\mathrm{CALIFA}}(p,pn)\,(\epsilon_{\mathrm{empty}} + t_{\mathrm{target}})}{2.}. \tag{7.4.9}$$

Preliminary QFS (p,pn) cross sections for the Ca isotopic chain have been calculated and are presented in Table 7.15.

	^{40}Ca	^{48}Ca	^{49}Ca	^{50}Ca
σ(p,pn)$_{\mathrm{exp}}$ [mbarn]	9±2	13±2	16±2	14±3

Table 7.15: QFS (p,pn) cross sections for Ca isotopes. .

It is noted that values in Table 7.15 are lower than expected due to this larger than expected efficiency calculation, however the expected increasing correlation with mass number is present. Opening angle distributions have also been produced for reaction channels with available statistics and shown in Figure 7.13.

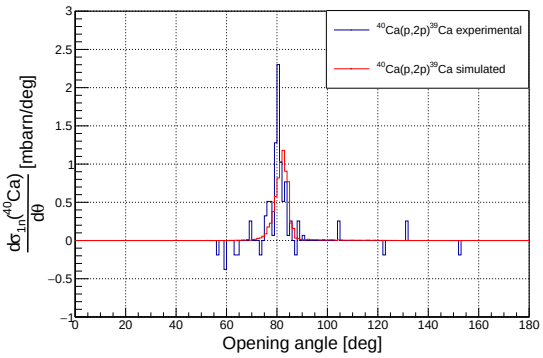

(a) ^{40}Ca(p,pn)^{39}Ca reaction channel.

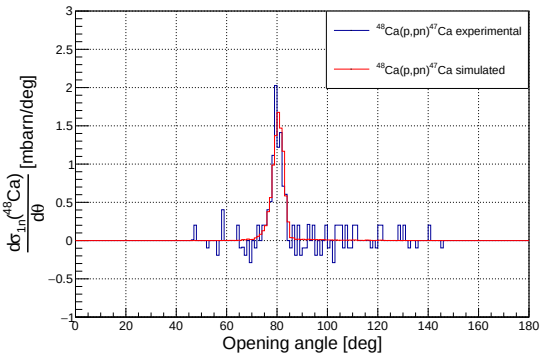

(b) ^{48}Ca(p,pn)^{47}Ca reaction channel.

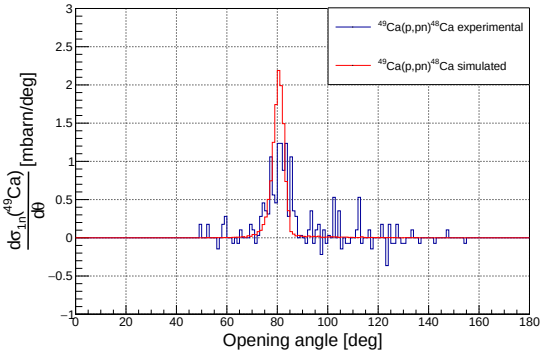

(c) ^{49}Ca(p,pn)^{48}Ca reaction channel.

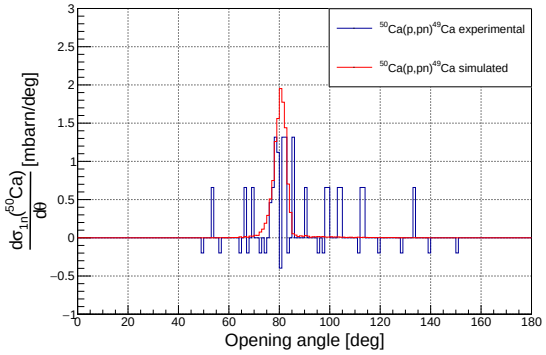

(d) ^{50}Ca(p,pn)^{49}Ca reaction channel.

Figure 7.13: Experimental QFS (p,pn) cross sections for Ca isotopes (blue) and the equivalent simulation used (red).

From Figure 7.13 the opening angles have a consistent peak position. Due to the low statistics and uncertainty with the simulated neutrons efficiency the peak height is not consistent for all distributions such as plot (c) and plot (d). This highlights the importance of further studying the neutron detection efficiency of CALIFA for more accurate (p,pn) event reconstructions.

7.5 Discussion

Interaction cross sections in the Ca mass region have been calculated using C, CH_2 and empty targets with beam energies of 400-500 AMeV using inverse kinematics. Mass identification of both the incoming ions and outgoing fragments was achieved

with a suitable resolution for transmission studies. The number of scattering centres in each target was calculated using two different methods and was within 1% of each other; therefore, a systematic error of 1% can be considered. The inconsistent transmissions observed in the ^{38}Ca empty target runs was remedied by applying an empty run average. In doing this a systematic error of 2.5% is considered for both C and CH_2 cross sections. When subtracting the C contribution from the CH_2 target the error from the empty target effectively cancels out, therefore a smaller systematic error of 1% is more reasonable for H cross sections. Calculated interaction cross sections on hydrogen are consistent with values obtained from the Kox parametrization as seen in Figure 7.1. Inclusive one proton removal cross sections in the Ca mass region have been calculated. As seen in Figure 7.2, as nuclear asymmetry increases the one proton removal cross section decreases. This is because as the neutron number increases the neutron separation energy decreases such that when a proton is removed the resulting daughter nuclei is more likely to be in an unbound state such that further reactions occur. This also happens as the knocked out proton is from a deeper state as the neutron number increases, therefore the resulting fragment is left in a highly excited state. Exclusive cross sections could not be calculated due to the limited efficiency of CALIFA. Preliminary QFS cross section for both (p,2p) and (p,pn) have also been calculated for the Ca isotopic chain. In using CALIFA to tag protons and neutrons simulations were required to reconstruct the efficiency of using this method. This was calculated to be $\epsilon_{\mathrm{CALIFA}}(p,2p)$=18.1% and $\epsilon_{\mathrm{CALIFA}}(p,pn)$=12.7% for the QFS (p,2p) and (p,pn) reaction mechanisms respectively. This method has limitations as the efficiency is very much dependent on where the beam hits the target and the location of the target and the Geant4 physics list used. This then appears to have overcompensated slightly as some (p,2p) cross sections such as ^{44}K and ^{45}K have larger QFS (p,2p) cross sections than one proton removal cross sections. A further systematic error of 2.0% is considered (1% for z, 0.5% for x and 0.5% for y). The aim of this experiment was to produce a kinetically complete measurement to study QFS reactions, however at the time of writing this thesis the neutron analysis from NeuLAND (Neu Large Area Neutron Detector) was not completed and there was no access to a recoil tracker around the target.

In the proposal for the experiment a silicon tracker utilizing Double-sided Silicon Strip Detector (DSSD) called Alpha Magnetic Spectrometer (AMS) was planned, however issues with the vacuum chamber meant this was not possible. Even with this limitation the angular resolution of CALIFA (approximately 2 degrees) was sufficient for reconstructing the opening angle between two high energy hits. Angular distributions produced from simulation, match well with experimental distributions for both (p,2p) and (p,pn) reaction channels. For proton rich nuclei the calculated QFS cross section is consistently lower than the one proton removal cross section. For neutron rich nuclei the values remain consistent with that of one proton removal cross sections. Momentum distributions for the P_x component of the QFS (p,2p) reaction channels were obtained showing a loosely decreasing correlation. Due to lack of statistics and the limited position resolution the y-transverse momentum distributions have not been included, but from the kinematics both components should be equal. It is also noted that the value of internal momentum spread of 120 MeV/c used in simulation is consistent with the experimentally measured momentum widths of neutron rich Ca isotopes. SP theoretical momentum distribution for the ^{40}Ca(p,2p)^{39}K and ^{48}Ca(p,2p)^{47}K reaction channel for the *sd* shell have been provided by Carlos Bertulani. Upon summing these distributions using the upper limit of the IPM for each shell it is clear that the ^{40}Ca distribution matches well with experiment. For the ^{48}Ca reaction channel the experimental x-transverse momentum distribution is narrower than the summed theoretical distribution, therefore a higher S wave and lower D wave component is expected. Preliminary reduction factor for QFS (p,2p) reactions for Ca isotopes have been calculated and compared to summed SP theoretical cross sections using the upper limit of the IPM. This shows a very weak correlation with nuclear asymmetry.

Chapter 8

Research and Development

With the move to FAIR (Facility for Antiproton and Ion Research), new upgraded detectors are required. The overview of the planned FAIR site can be seen in Figure 8.1, where the NUSTAR (NUclear STructure, Astrophysics and Reactions) collaborations cave is highlighted.

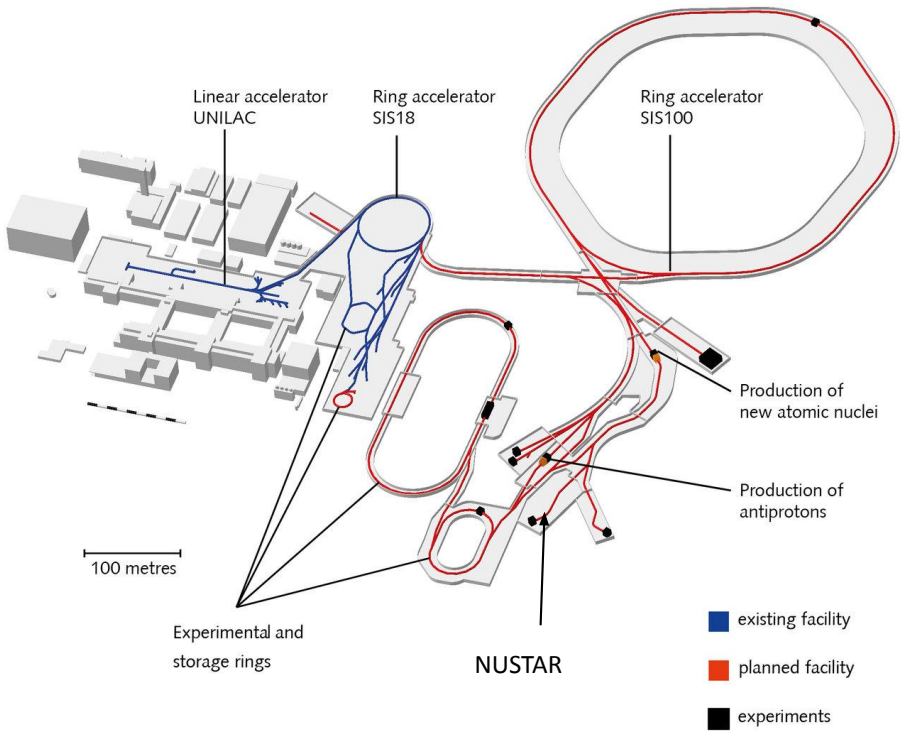

Figure 8.1: Overview of the planned FAIR facility[56]. The NUSTAR cave will host the R^3B setup.

The upgraded R^3B setup will be located in this cave. Several of the detectors for the setup have been mentioned already in the previous chapters such as NeuLAND and CALIFA, the Target Recoil Tracker (TRT) is still under development. Historically, AMS detectors were used for this purpose. These were DSSD with active area of 72×40 mm^2 and 0.3 mm thick. These detectors are no longer suitable due to age and no available upgrades, subsequently a replacement is needed. The goal of the new recoil tracker is to be able to measure from 50-1500 MeV protons while also producing a very accurate vertex reconstruction. It must also have a large angular coverage for a greater geometrical acceptance and to allow for full angular reconstruction. The new detector will be comprised of ALPIDE (ALice PIxel Detector) which will be covered in more detail in the following chapter. The production of the new TRT is split into several stages. Figure 8.2 shows the design for the stage one setup inside the target chamber (grey) and surrounded by CALIFA (red).

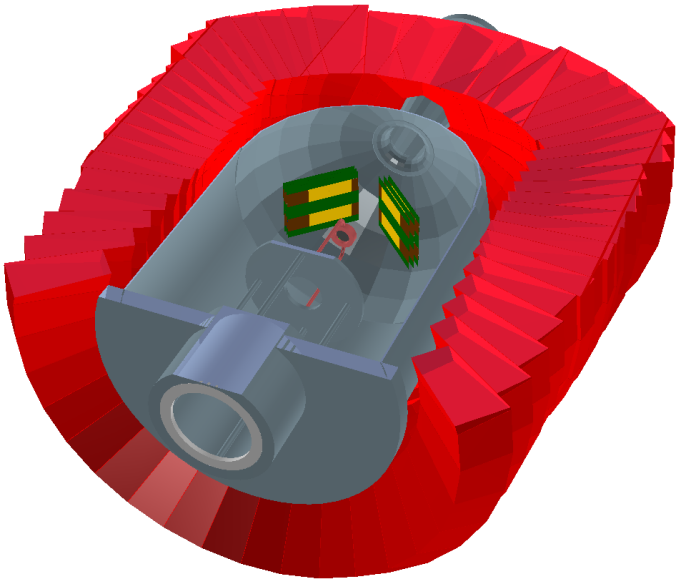

Figure 8.2: The stage one design for the TRT consisting of three planes on the Messel side and 3 planes on the Wixhausen side of the target chamber. Each plane then contains three Flexible Printed Circuit boards (FPCs) with six ALPIDEs per FPC. This covers an active area of approximately 9×9 cm^2 per side.

This setup will be the interim until the barrel design is finalised and produced. Figure 8.3 shows the current barrel design (green) placed inside the target chamber.

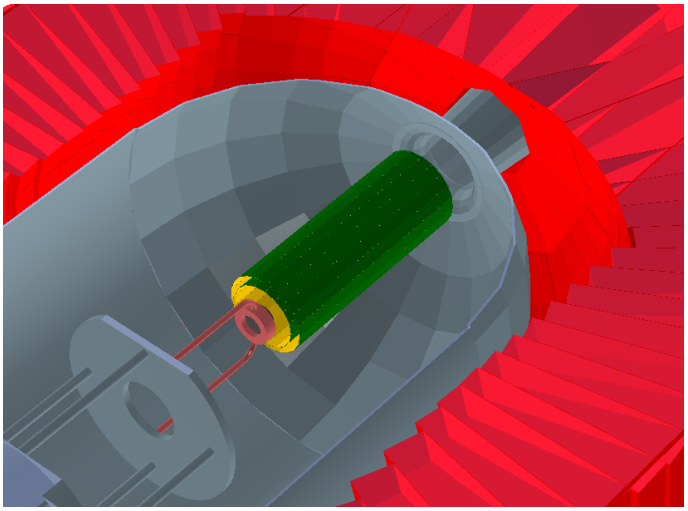

Figure 8.3: The stage two design consists of 54 staves arranged in 3 barrels. Each stave has 9 ALPIDE sensors. Each stave is then 9 cm long.

In the next part of this chapter we will discuss the currently used interim detector and its successor.

8.1 FOOT

FOOT (FragmentatiOn Of Target) detectors are a temporary replacement to the AMS detectors during the phase 0 experiments. They are Single-sided Silicon Strip Detectors (SSSD) with a strip pitch of 50 μm each strip has 2 corresponding floating strips making a total pitch of 150 μm. There are 64 of these strips per Application-Specific Integrated Circuit (ASIC) and 10 ASICs per detector making a total of 640 channels per detector. The corresponding active area is approximately 100 cm^2 from the square geometry and two of these detectors are required to produce an x and y measurement.

Figure 8.4: Front side of the first R3B FOOT detector. Here all 10 ASICs are visible each connected to 64 strips.

Measuring purely the output signal from each detector a pedestal measurement can be taken which is shown in plots (a) and (b) of Figure 8.5. By fitting a Gaussian distribution to each strip in plots (a) and (b) a value for the Full Width Half Maximum (FWHM) can be calculated which is shown in plots (c) and (d).

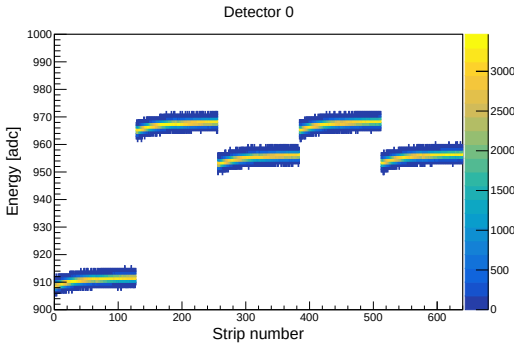

(a) Detector 0 pedestal.

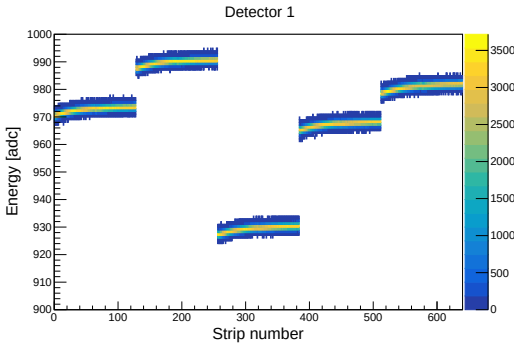

(b) Detector 1 pedestal.

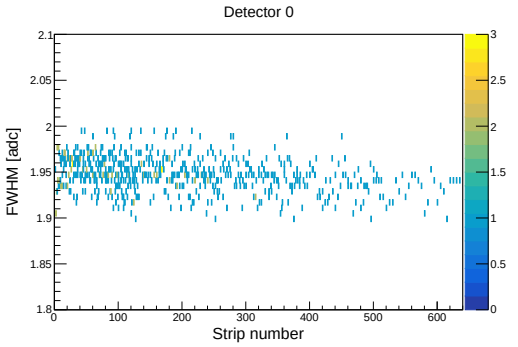

(c) Detector 0 FWHM.

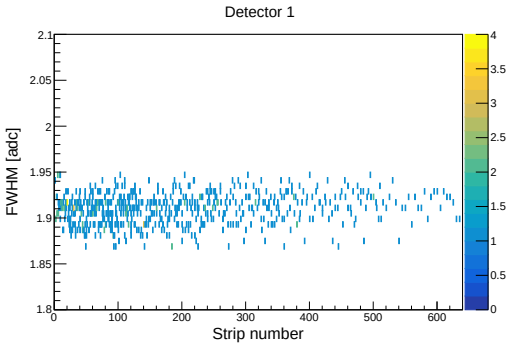

(d) Detector 1 FWHM.

Figure 8.5: First time pedestal measurements taken with two FOOT detectors and there corresponding FWHM per channel.

This baseline can then be subtracted strip by strip for each detector and any value recorded in the future above this can be considered as a potential hit. Limitations of this system are that the readout unit was limited to less than 5 kHz and that no direct measurement of energy was possible.

8.2 ALPIDE Detectors at GSI for R3B

The final design as shown in Figure 8.3 will be a barrel detector made up of Monolithic Active Pixel Sensors (MAPs) namely the ALPIDE created for the ALICE experiment at CERN produced by TowerJazz [57]. Individual sensors contain pixels measuring 26.88×29.24 μm^2 in an array of 1024×512. A full sensor has an active area including periphery of 3.0×1.5 cm^2. The silicon wafer is 50 μm thick which

altogether gives the sensor a high position resolution, but currently there is no direct way of measuring the energy deposited by a charged particle. They have a high radiation tolerance and are also ideal for in beam detectors. The final design should have a combined angular resolution of $\sigma_{angle} < 2$ mrad. It should also have a sub mm spatial resolution of the z component of the vertex. The angular coverage of the barrel should complement the surround CALIFA detector so 10–90 degrees in theta and 2π in phi. Currently, there is no exact requirement for timing resolution. It has been shown that ALPIDE can achieve a event timing resolution of 2–4 μs. This corresponds to a maximum trigger rate of 25–50 kHz event rate [58]. This is far higher than what is currently achievable by the AMS and FOOT detectors and within the requirements of the collaboration.

8.2.1 Readout Scheme and Data Acquisition

Each pixel within an ALPIDE sensor contains its own amplifier and shaper connected to a comparator and multi-event buffer capable of storing up to 3 hits. A global threshold for each sensor can be applied such that each detector will have a similar response to a charge particle passing through it. The readout is arranged in a "snaking" pattern down double columns of size 2×512 pixels. 16 double columns are connected to a priority encoder making 32 regions per sensor. The purpose of the priority encoder is to index the region of the sensor the hit is from. One readout cycle corresponds to a trigger being received and each region being strobed. This process should then be repeated until all buffers are empty, however if externally triggered this is not necessarily the case.

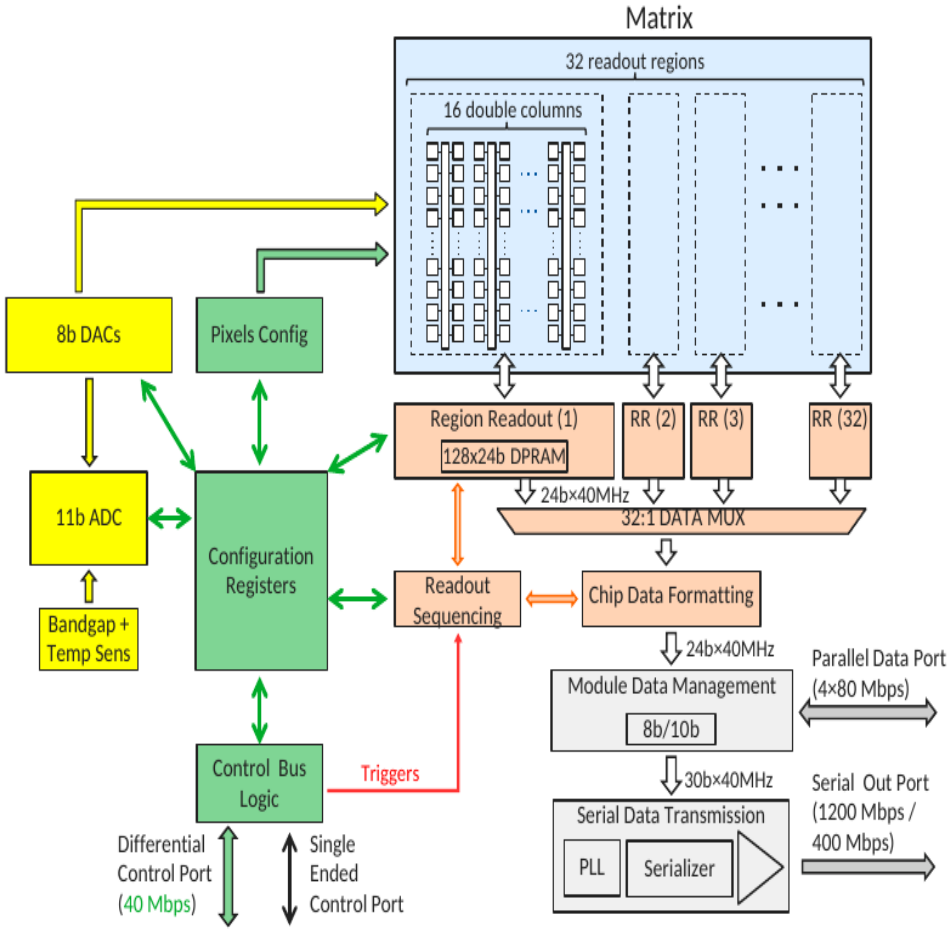

Figure 8.6: Diagram of a single ALPIDE sensor consisting of 1024×512 pixels arranged into 32 double columns with each column being 16 pixels wide.

The ALPIDE is read out via a MOSIAC (MOdular System for Acquisition Interface and Control). The MOSAIC is a VME-8U module developed by INFN Bari [59]. Each MOSAIC has 10 receivers with each receiver capable of reading out 1 sensor, however tests at GSI have only read out 6 at the time of this thesis. Each receiver is capable of a bandwidth up to 1.2 Gbps. A SAMTEC firefly cable is connected to the HI speed Input/output (I/O) seen in Figure 8.7. Each cable has 9 differential pairs for data, one differential pair for clock and one differential pair for control. The data is then processed and shipped over the gigabit ethernet to a switch which then connects to a 10 Gbps ethernet card on the DAQ pc. Each MOSAIC contains 4 Nuclear Instrumentation Module (NIM) I/O ports. Solder pads on the MOSAIC

board can be configured to set whether the NIM is an input or an output. Modifications to the firmware have also been made for signal processing. The current configuration used by GSI is NIM 0 being used to receive a time stamp delivered by the 6.25 MHz RATA clock protocol [60] and generated by an GSI EXPLODER3 with modified firmware [61]. NIM 2 is configured to receive another external trigger. NIM 3 is configured to send out the busy signal which can be used in further TRLO [62].

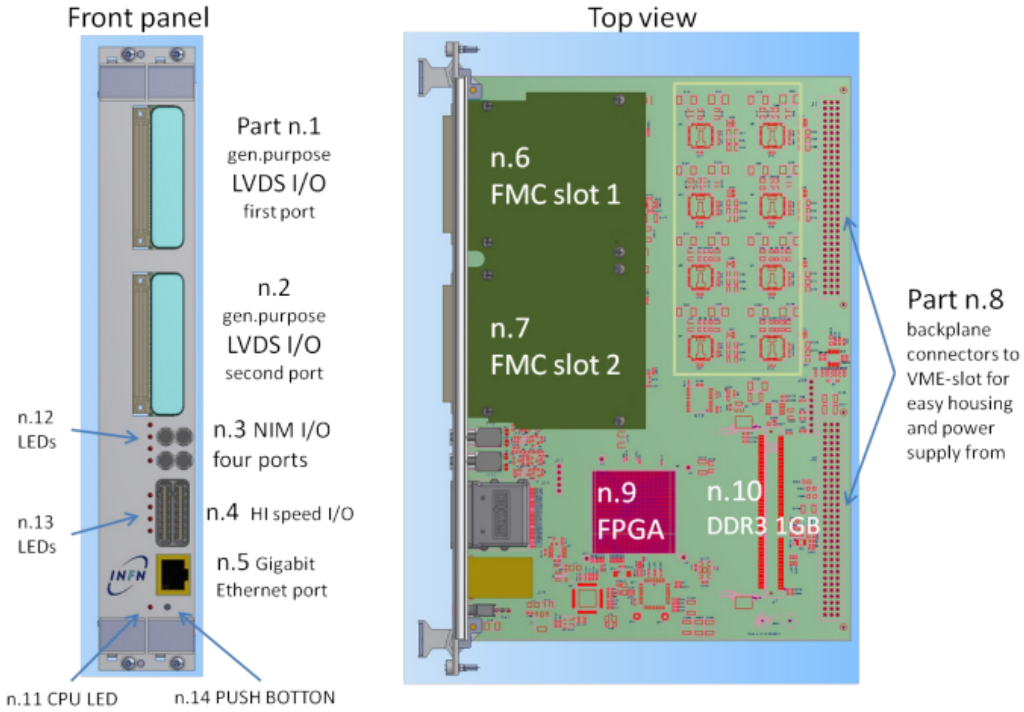

Figure 8.7: Schematic of the MOSAIC FPGA used for the readout of the ALPIDE.

8.2.2 Test Experiments

Several test beams have been performed using these sensors with the aim to improve our understanding of how to run the detectors and to build analysis tools for the data that is produced. The first such data produced was a measurement using a Single Carrier Card (SCC) and a ^{55}Fe beta source. A hit map of the data is shown in Figure 8.8

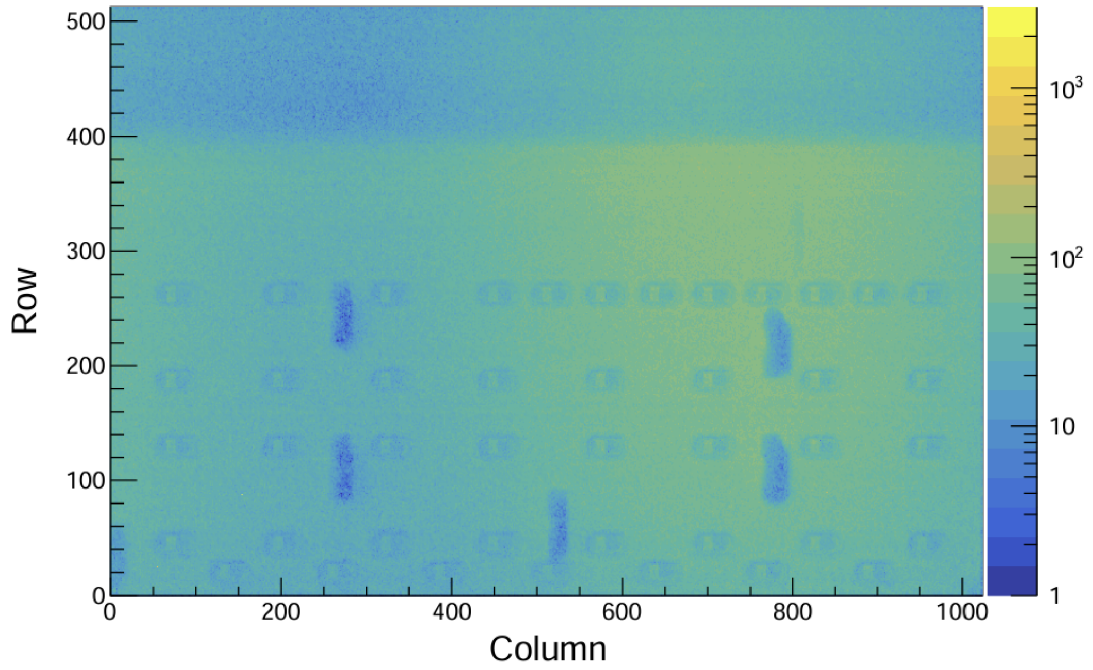

Figure 8.8: ^{55}Fe beta source measurement using a SCC. Intensity changes in the rows 400–512 correspond mylar foil covering the top part of the sensor. Bonding pads are visible in rows 0–280.

The first in beam test conducted by R^{3}B using SCC was performed on November 2021 at the COMPASS beam line. This work was in collaboration with COMPASS [63] (now AMBER [64]) with the joint aim of understanding and using ALPIDE. Our setup consisted of four SCC used in standalone mode read out by four MOSAIC FPGA. At this time no timestamp or trigger information was available so only hit maps were available as seen in Figure 8.9.

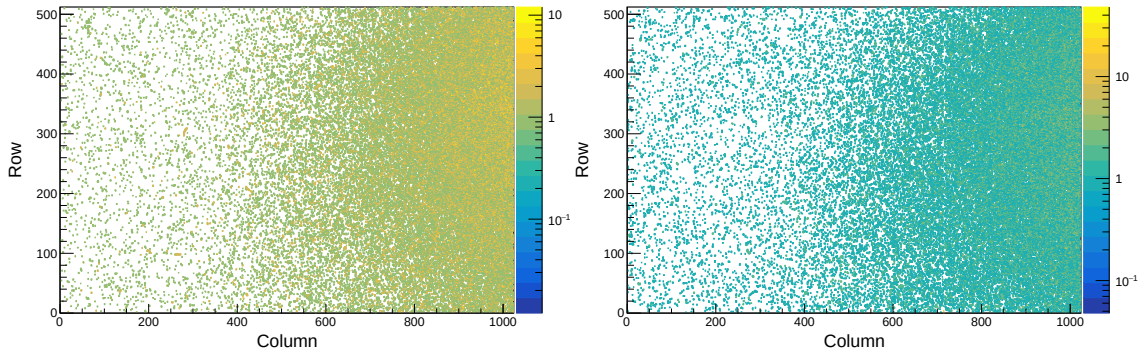

(a) Detector 0 hit map.

(b) Detector 1 hit map.

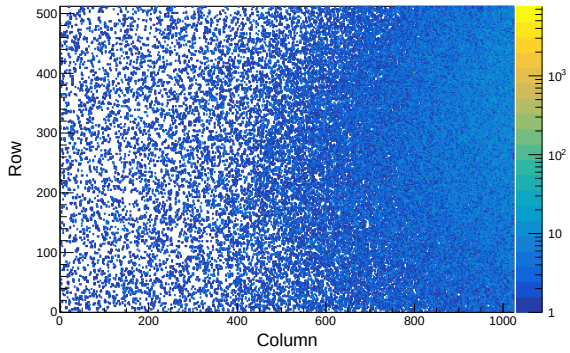

(c) Detector 2 hit map.

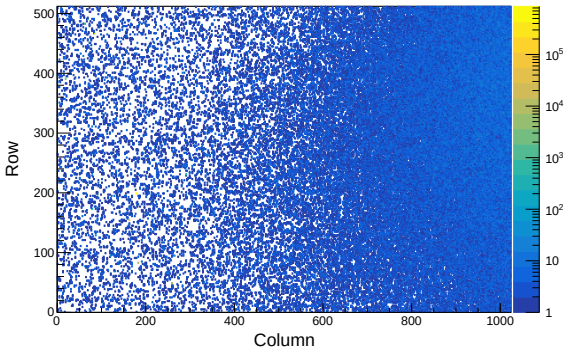

(d) Detector 3 hit map.

Figure 8.9: Hit maps for all four SCC. Plot (a) and (b) have all noisy pixels removed and plot (c) and (d) have no noisy pixels removed to highlight the need for pixel masking.

Plots (a) and (b) of Figure 8.9 have had all noisy pixels removed after analysis. Plots (c) and (d) have not had any pixels removed this is to highlight the importance of pixel masking to stop data saturation. After this beam time it was critical that pixel masking and synchronisation between detectors was made. This was done by updating the DAQ by adding time stamping and adding to the exisiting software to access the pixel masking registers. These features were then tested at Forschungszentrum Jülich. Unfortunately, at the time of the test beam only one sensor was available. Before the beam time the masking functionality was tested as can be seen in Figure 8.10.

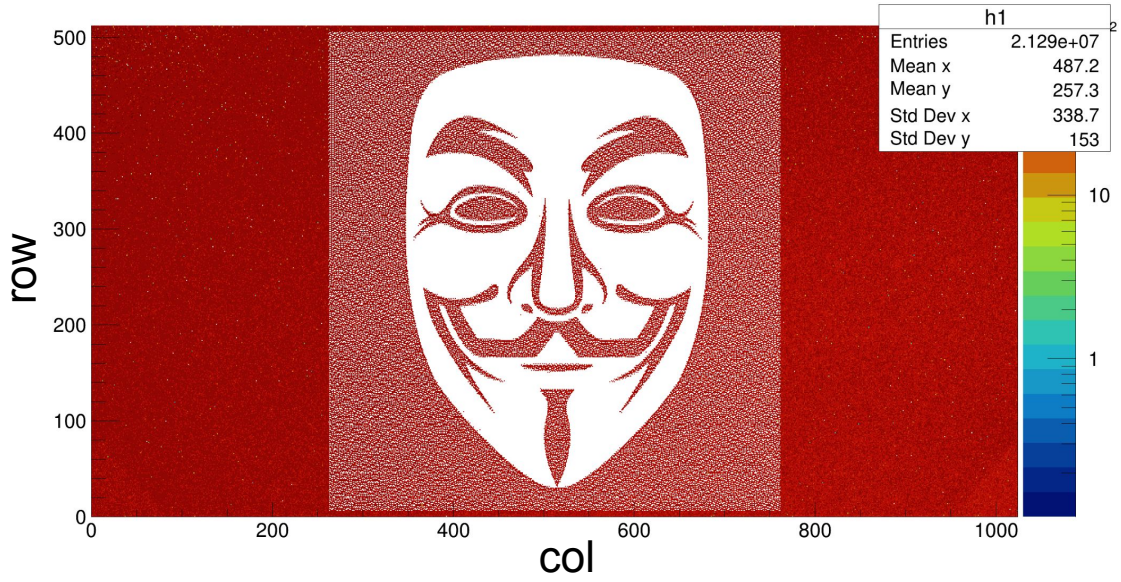

Figure 8.10: A mask was applied to a SCC and the threshold was reduced to the lowest possible value, such that all unmasked pixels return a hit.

After this another beam test was performed with the AMBER collaboration during November 2022 using a muon beam at 160 GeV/c. The detectors also ran parasitically as part of the final COMPASS runs with protons at energies of 200 GeV.

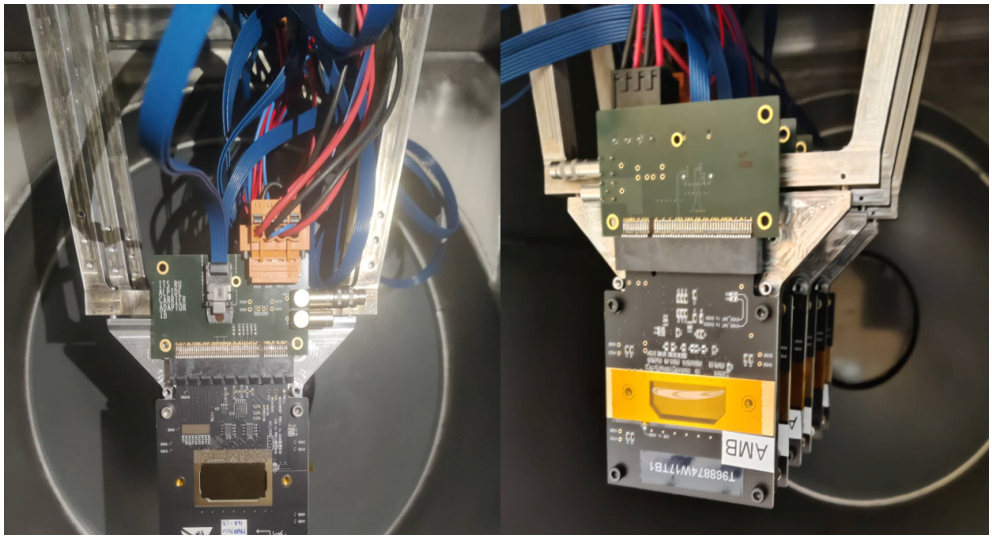

Figure 8.11: The left image shows the back of the SCC telescope and the right the front with respect to the beam. The detectors are placed inside the unified tracking station chamber provided by the AMBER collaboration.

A start trigger was provided from a plastic scintillator detector from AMBER. This trigger was then sent to the MOSAICS provided it did not fall into a dead time window of 40 μs. This was done using the custom trloii [62] firmware on a VULOM4B [38]. If this dead time was lowered, either data saturation would occur or triggers would come while the MOSAIC was busy which would cause the DAQ to crash. This can be optimized by supplying the busy signal over NIM3 to the VULOM4B, however, this was not functional at the time of the experiment. Algorithms for clustering and tracking were produced. For this analysis, cluster size larger than 3 pixels and less than 10 pixels were selected and clusters in all sensors must be present for a track reconstruction. Figure 8.12 shows the tracks reconstruction from all six SCC.

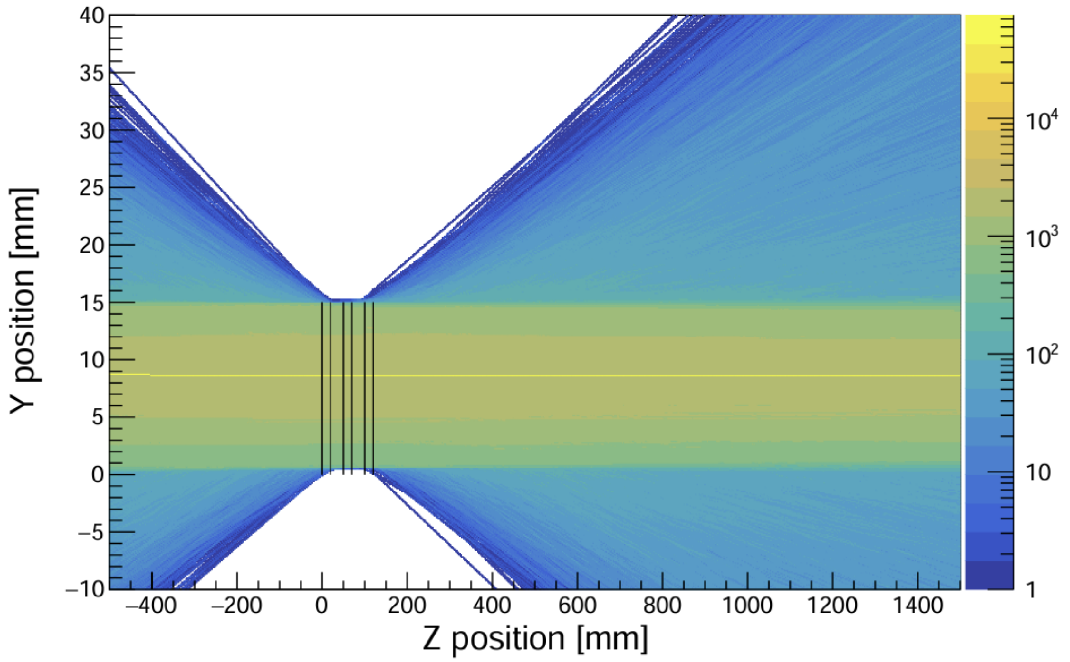

Figure 8.12: Track reconstruction in yz plane from the six SCC cards where the black vertical lines show the position of the sensors.

To calculate the resolution the same track reconstruction is produced with just five SCC and then compared to the position in the sixth detector. This difference between these two positions is plotted in Figure 8.13.

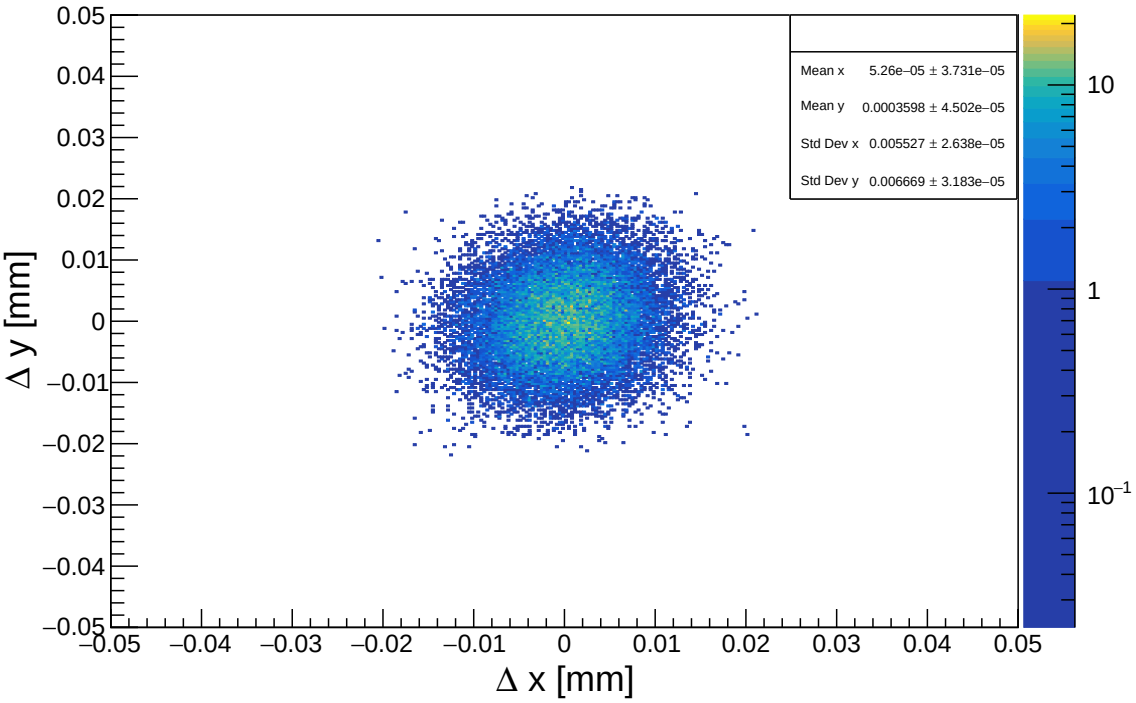

Figure 8.13: The difference between the track reconstructed by five SCC's and the position in the sixth detector.

The value of the resolution is then given by the standard deviations in plot. The x position resolution is 8.13 σ_x=5.53(3) μm and the y position resolution is σ_y=6.67(3) μm, which is in reasonable agreement with the 5 μm measurement provided by ALICE [57]. Further tests at varying intensity were also performed. Figure 8.14 shows that increasing the beam intensity did not change the mean cluster size measured.

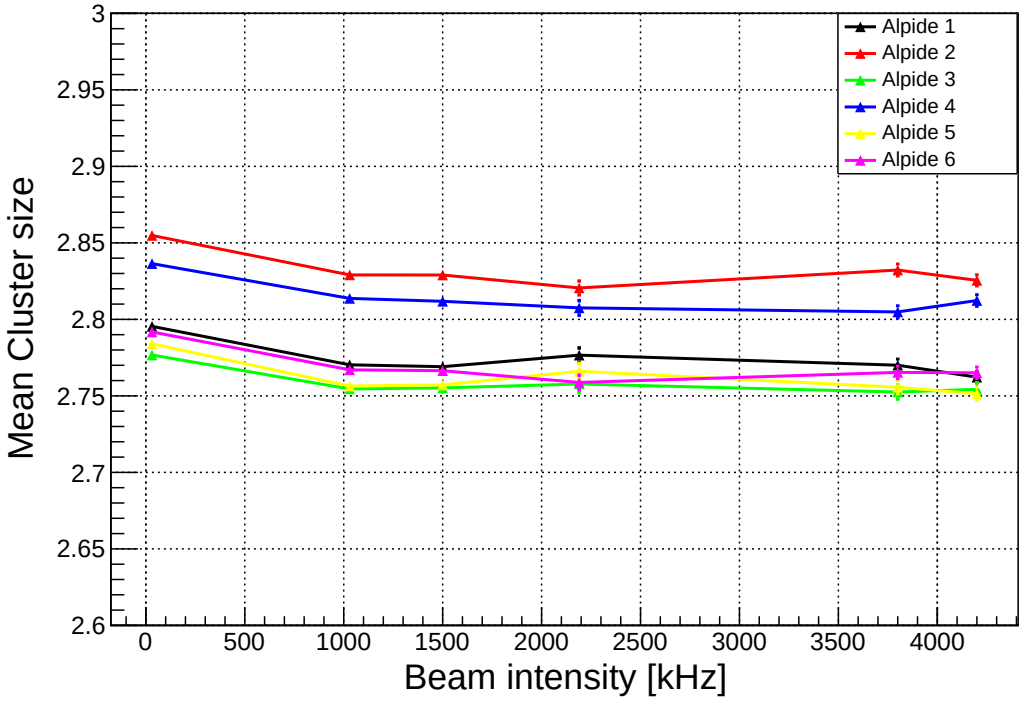

Figure 8.14: Mean cluster size for each beam intensity for each SCC.

This shows that the analysis framework was capable of handling multiple hits in a single sensor per trigger.

8.3 Future Developments

To progress this work larger arrays of sensors are needed to increase the active area. Based on the technology developed by the LIMADOU experiment [65], a prototype FPC (Flexible Printed Circuit board) was designed containing 3×2 sensors.

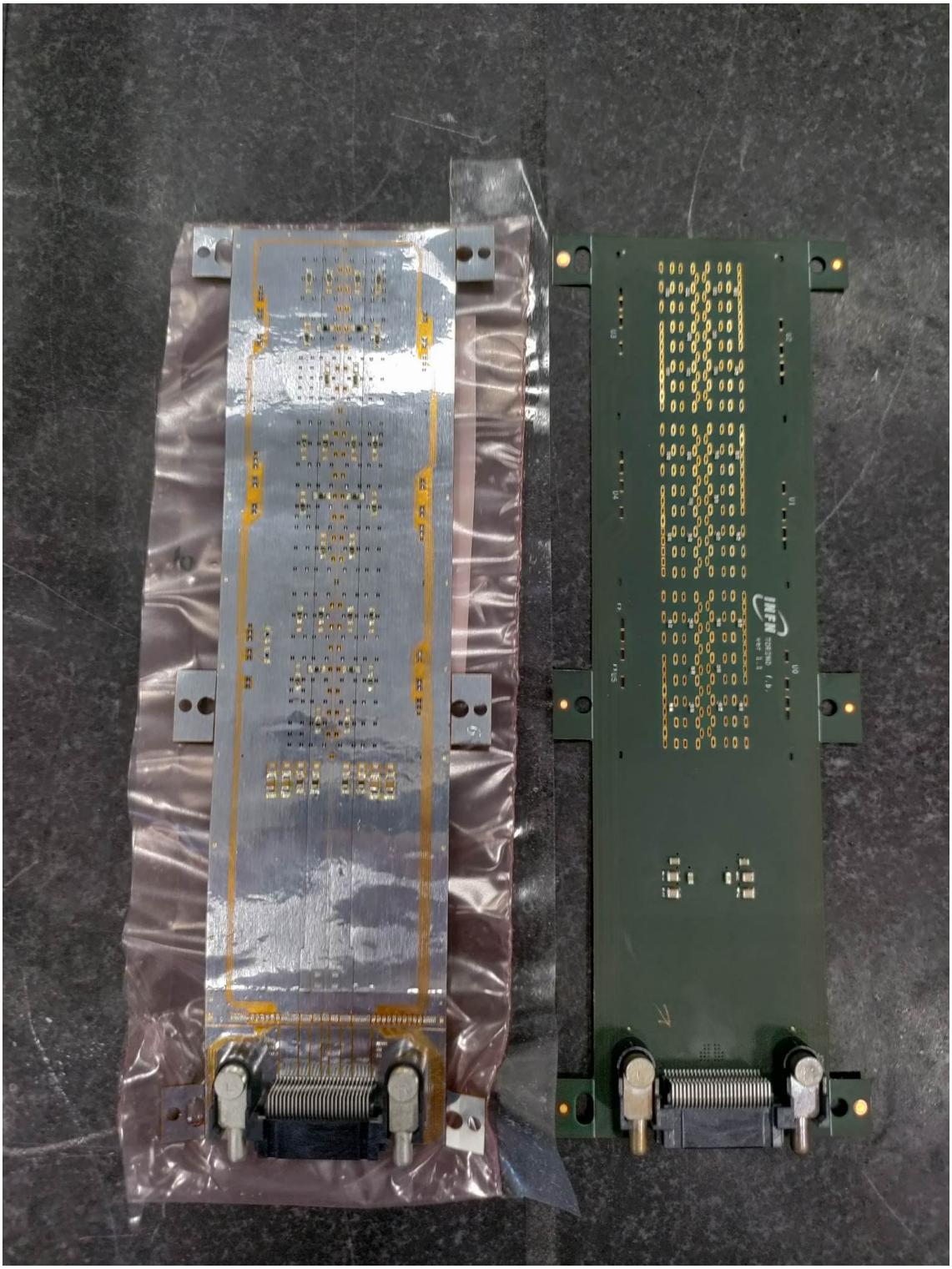

Figure 8.15: On the left is a FPC made of Al and on the right a FPC made of Cu.

The left FPC was made of Al and was very flexible, this caused issue with the

existing LIMADOU mounting and vacuum jigs. The right FPC was made of Cu just like the LIMADOU FPC resulting in the existing LIMADOU jigs working. Issues with the gluing of the sensors caused problems when it came to the bonding of the sensors, resulting in only partial populated sensors being produced. The detectors were assembled in the Istituto Nazionale di Ricerca Metrologica in Turin. A Coordinate Measuring Machine (CMM) is used to place the sensors on a teflon bed as seen in Figure 8.16.

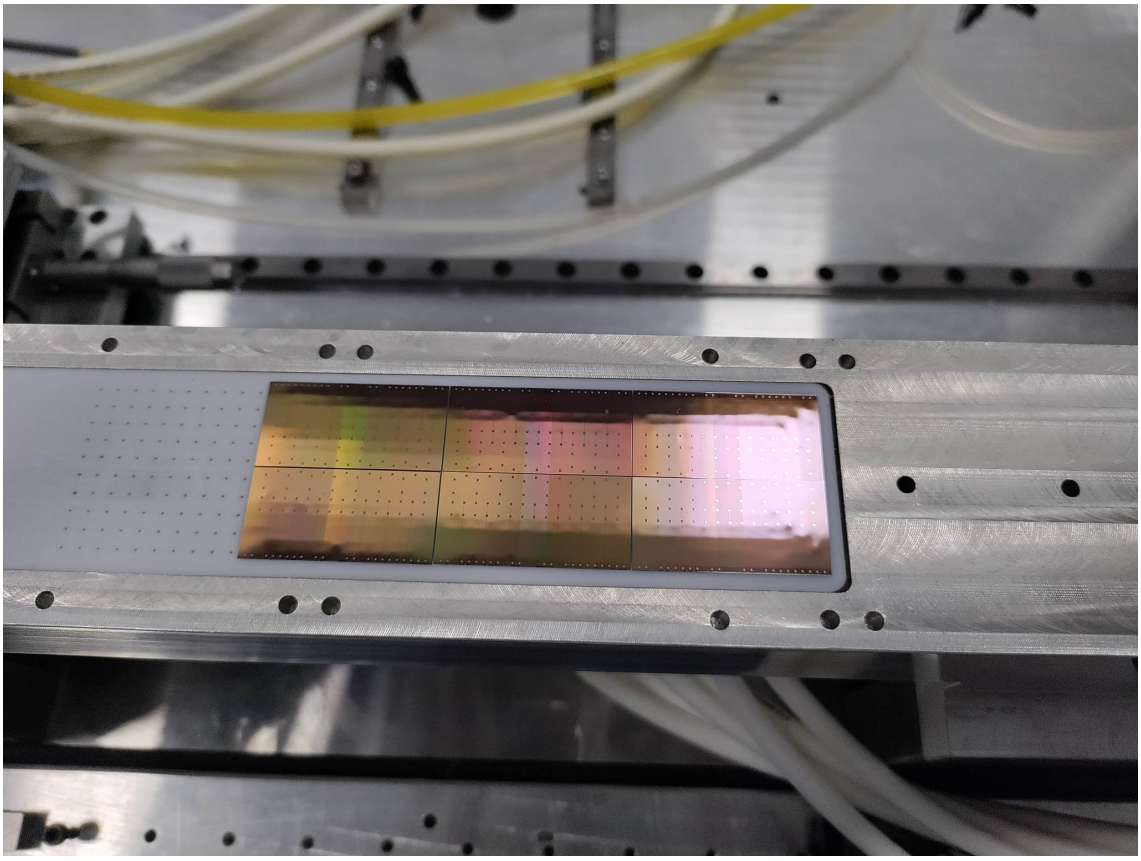

Figure 8.16: Six ALPIDE chips held on a vacuum teflon bed. The orientation of the sensors is such that the periphery of the chip is placed closest to the edge of the jig.

Then Araldite 2011 glue is applied to an FPC using a mask and then placed on top of the six sensors. The FPC's were then taken back to GSI for bonding. Three FPC are then glued to a carbon cooling plate to form the stage one detector. These detectors were then used in experiments during March 2024. Figure 8.17 shows the combination of two FPC forming a plane mounted with four FOOT detectors.

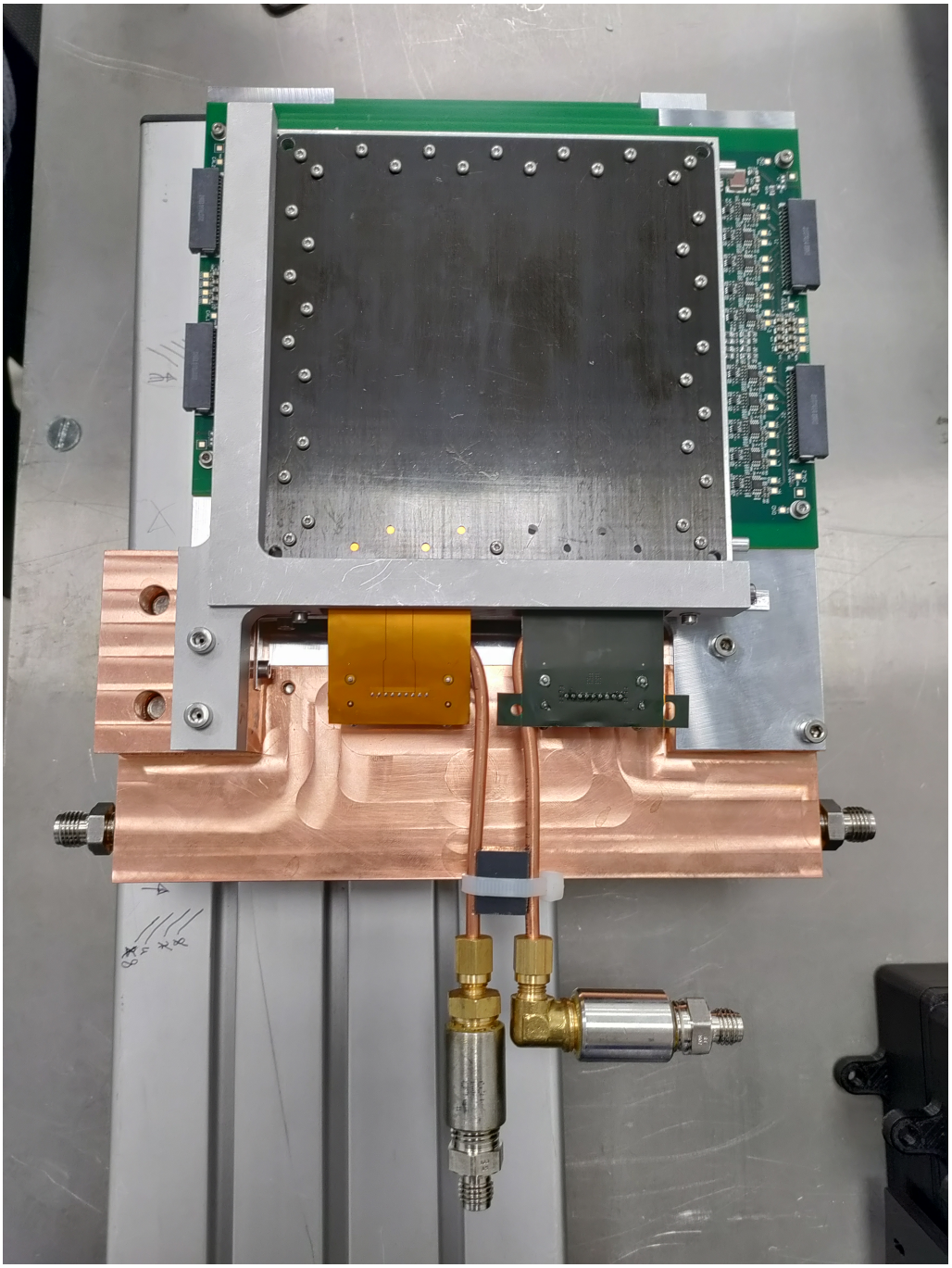

Figure 8.17: A plane of the silicon tracking detectors used in the s091 and s118 R^3B experimental campaigns, consisting of two x and two y FOOT detectors and two partially completed FPC.

The FPC have a different style SAMTEC connector to that used with SCC and require a converter board.

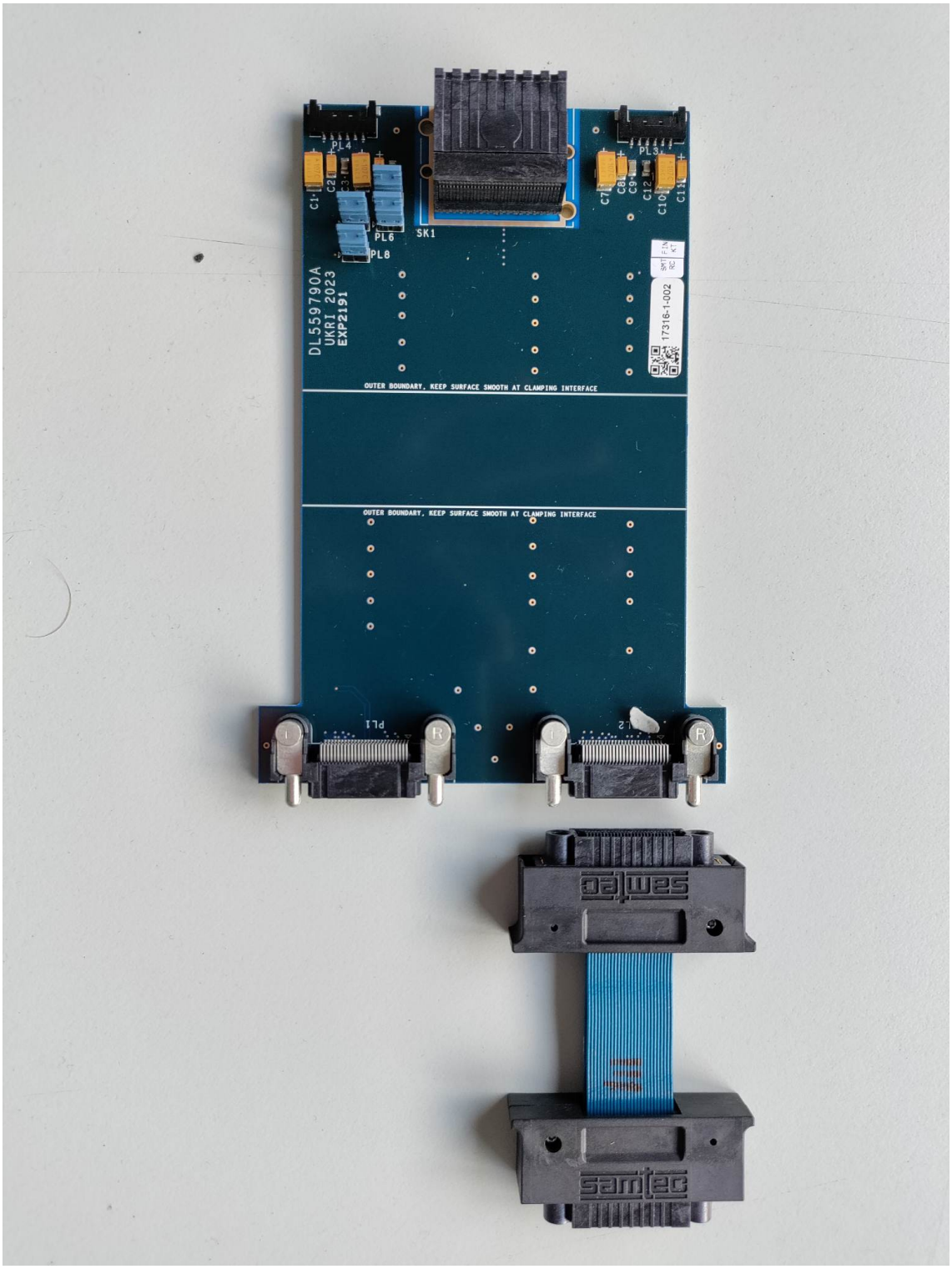

Figure 8.18: FPC vacuum feedthrough designed by Daresbury laboratories.

The s091 experiment performed in March 2024 involved elastic scattering of deuterons and tritons on a LH_2 target at varying energies.

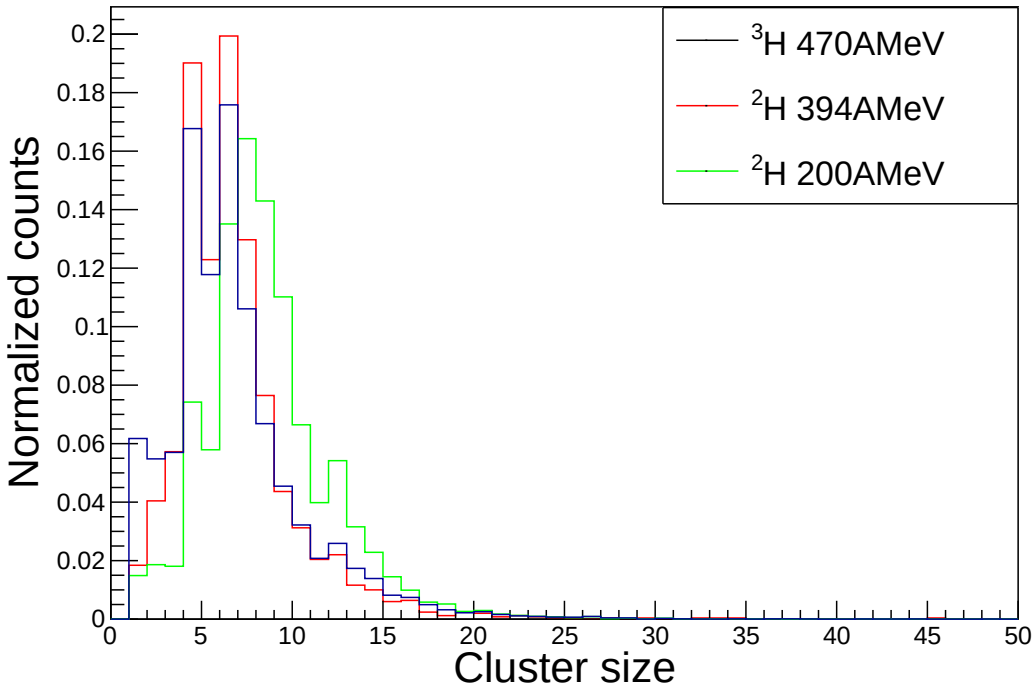

Figure 8.19: Cluster size distributions for each run setting of the s091 experiment.

When comparing the deuteron runs in Figure 8.19 the shape and mean cluster size of the distribution is different. This implies there is an energy dependence on cluster size. Due to limited statistics and FOOT analysis not being completed at the time of this thesis an in depth study is still not available.

Chapter 9

Conclusion and outlook

In this thesis new experimental results for: interaction, one proton removal, QFS (p,2p) and QFS (p,pn) cross sections have been obtained for a variety of isotopes in the A=40–48 Ca mass region. The calculated interaction cross sections on hydrogen exhibit a good correlation with the predictions derived from the Kox parametrization. Inclusive one proton removal cross sections in the Ca mass region have been measured, showing a consistent decreasing trend across all isotopic chains as neutron number increases. This is consistent with predictions from reaction and nuclear structure theory. Preliminary QFS (p,2p) cross sections for the Ca isotopic chain have been calculated and compared to available theoretical cross sections calculated using the IPM. To improve these calculations detailed nuclear structure models in place of the IPM could be used. This would allow for a more precise comparison of reduction factors extracted from other reaction studies. The reduction factors that have been calculated show a weakly decreasing correlation as a function of nuclear asymmetry. Extracting inclusive one-neutron cross sections was not possible at this time due to challenges in separating the unreacted beam component from the one-neutron removal channel. This issue was resolved when calculating the QFS (p,pn) by applying (p,pn) tagging conditions in CALIFA. Experimental QFS (p,pn) cross sections for Ca are presented showing an increasing trend with nuclear asymmetry. These values are not final and show a surprisingly high CALIFA (p,pn) efficiency. To improve on them further studies on different Geant4 models on the neutron reconstruction in CALIFA should be performed. The inclusion of the NeuLAND

analysis would also benefit this study for separating the neutron evaporation channel. Exclusive cross sections could not be extracted due to limitations in statistics and resolution from CALIFA, as well as the absence of a recoil tracker around the target region. Without a tracker it is not possible to perform vertexing studies, so all reactions are assumed to come from the centre of the target making the reconstruction of correlated nucleon pairs challenging. Research and development has been conducted and presented for the first time showing the development for the new recoil tracker for the R^3B collaboration. This includes advancements made in the DAQ, along with the successful measurement of the ALPIDE, x position resolution of σ_x=5.53(3) μm and the y position resolution is σ_y=6.67(3) μm using a SCC telescope. Tests using prototype stage 1 detectors have now been performed and preliminary analysis has been shown. Correlations between cluster size and energy deposition of different particles has been shown. To improve on our understanding of this relation, more beam time dedicated to the measurement of heavy ions with stage one detectors is required.

Bibliography

[1] Maria Goeppert Mayer. "On Closed Shells in Nuclei. II". In: *Phys. Rev.* 75 (12 June 1949), pp. 1969–1970. DOI: 10.1103/PhysRev.75.1969. URL: https://link.aps.org/doi/10.1103/PhysRev.75.1969.

[2] M.Mayer and J.Jensen. *Elementary theory of nuclear shell structure*. 1955.

[3] W. Pauli. "Über den Zusammenhang des Abschlusses der Elektronengruppen im Atom mit der Komplexstruktur der Spektren". In: *Zeitschrift für Physik* 31 (1925), pp. 765–783. DOI: 10.1007/BF02980631.

[4] O. Sorlin and M.-G. Porquet. "Nuclear magic numbers: New features far from stability". In: *Progress in Particle and Nuclear Physics* 61.2 (2008), pp. 602–673. ISSN: 0146-6410. DOI: https://doi.org/10.1016/j.ppnp.2008.05.001. URL: https://www.sciencedirect.com/science/article/pii/S0146641008000380.

[5] B. H. Wildenthal and W. Chung. "Collapse of the conventional shell-model ordering in the very-neutron-rich isotopes of Na and Mg". In: *Phys. Rev. C* 22 (5 Nov. 1980), pp. 2260–2262. DOI: 10.1103/PhysRevC.22.2260. URL: https://link.aps.org/doi/10.1103/PhysRevC.22.2260.

[6] T. Aumann et al. "Quenching of single-particle strength from direct reactions with stable and rare-isotope beams". In: *Progress in Particle and Nuclear Physics* 118 (2021), p. 103847. ISSN: 0146-6410. DOI: https://doi.org/10.1016/j.ppnp.2021.103847. URL: https://www.sciencedirect.com/science/article/pii/S0146641021000016.

[7] GERHARD JACOB and TH. A. J. MARIS. "Quasi-Free Scattering and Nuclear Structure". In: *Rev. Mod. Phys.* 38 (1 Jan. 1966), pp. 121–142. DOI: 10.1103/RevModPhys.38.121. URL: https://link.aps.org/doi/10.1103/RevModPhys.38.121.

[8] A. Gade et al. "Reduction of spectroscopic strength: Weakly-bound and strongly-bound single-particle states studied using one-nucleon knockout reactions". In: *Phys. Rev. C* 77 (4 Apr. 2008), p. 044306. DOI: 10.1103/PhysRevC.77.044306. URL: https://link.aps.org/doi/10.1103/PhysRevC.77.044306.

[9] J. A. Tostevin and A. Gade. "Updated systematics of intermediate-energy single-nucleon removal cross sections". In: *Phys. Rev. C* 103 (5 May 2021), p. 054610. DOI: 10.1103/PhysRevC.103.054610. URL: https://link.aps.org/doi/10.1103/PhysRevC.103.054610.

[10] B. P. Kay, J. P. Schiffer, and S. J. Freeman. "Quenching of Cross Sections in Nucleon Transfer Reactions". In: *Phys. Rev. Lett.* 111 (4 July 2013), p. 042502. DOI: 10.1103/PhysRevLett.111.042502. URL: https://link.aps.org/doi/10.1103/PhysRevLett.111.042502.

[11] Stefanos Paschalis. "Relativistic One-Nucleon Removal Reactions". PhD thesis. University of Liverpool, 2008.

[12] F. Wamers. "Quasi-Free-Scattering and One-Proton-Removal Reactions with the Proton-dripline Nucleus 17Ne at Relativistiv Beam Energies: Dissertation". PhD thesis. Technische Universität Darmstadt, Institut für Kernphysik, 2011.

[13] Valerii Panin, T. Aumann, and Carlos Bertulani. "Quasi-free scattering in inverse kinematics as a tool to unveil the structure of nuclei: A tribute to Mahir S. Hussein". In: *The European Physical Journal A* 57 (Mar. 2021). DOI: 10.1140/epja/s10050-021-00416-9.

[14] L. Atar et al. "Quasifree (p, $2p$) Reactions on Oxygen Isotopes: Observation of Isospin Independence of the Reduced Single-Particle Strength". In: *Phys. Rev. Lett.* 120 (5 2018), p. 052501. DOI: 10.1103/PhysRevLett.120.052501. URL: https://link.aps.org/doi/10.1103/PhysRevLett.120.052501.

[15] A.Bohr and B.R. Mottelson. "A.Bohr and B.R. Mottelson: Nuclear Structure, Vol. 1, W.A. Benjamin, Inc., New York, 1969". In: 1969. URL: https://api.semanticscholar.org/CorpusID:91881923.

[16] WE Brittin and LC Dunham. *High Energy Collision Theory*. 1959.

[17] Carlos A. Bertulani and Angela Bonaccorso. "Direct Nuclear Reactions". In: *Handbook of Nuclear Physics*. Ed. by Isao Tanihata, Hiroshi Toki, and Toshitaka Kajino. Singapore: Springer Nature Singapore, 2023, pp. 1415–1449. ISBN: 978-981-19-6345-2. DOI: 10.1007/978-981-19-6345-2_3. URL: https://doi.org/10.1007/978-981-19-6345-2_3.

[18] Tomohiro Uesaka. "On the kinematics of (p, pX) knockout reactions in normal and inverse kinematics". In: *Progress of Theoretical and Experimental Physics* (Jan. 2024), ptae013. ISSN: 2050-3911. DOI: 10.1093/ptep/ptae013. eprint: https://academic.oup.com/ptep/advance-article-pdf/doi/10.1093/ptep/ptae013/56346903/ptae013.pdf. URL: https://doi.org/10.1093/ptep/ptae013.

[19] I. Tanihata et al. "Measurements of Interaction Cross Sections and Nuclear Radii in the Light *p*-Shell Region". In: *Phys. Rev. Lett.* 55 (24 Dec. 1985), pp. 2676–2679. DOI: 10.1103/PhysRevLett.55.2676. URL: https://link.aps.org/doi/10.1103/PhysRevLett.55.2676.

[20] Nobuyuki Kobayashi. "Spectroscopy of neutron-rich nuclei via the inclusive breakup reactions". PhD thesis. Tokyo Institute of Technology, 2013. URL: https://cir.nii.ac.jp/crid/1110001310285368960.

[21] M. Petri S. Paschalis. *Single-particle structure of neutron-rich Ca isotopes: shell evolution along Z=20*. s467 experimental proposal.

[22] P. Spädtke et al. "Ion source development at GSI". In: *Review of Scientific Instruments* 69.2 (Feb. 1998), pp. 1079–1081. ISSN: 0034-6748. DOI: 10.1063/1.1148638. eprint: https://pubs.aip.org/aip/rsi/article-pdf/69/2/1079/19172644/1079_1_online.pdf. URL: https://doi.org/10.1063/1.1148638.

[23] W. Barth et al. "Upgrade program of the high current heavy ion UNILAC as an injector for FAIR". In: *Nuclear Instruments and Methods in Physics Research Section A: Accelerators, Spectrometers, Detectors and Associated Equipment* 577.1 (2007). Proceedings of the 16th International Symposium on Heavy Ion Inertial Fusion, pp. 211–214. ISSN: 0168-9002. DOI: https://doi.org/10.1016/j.nima.2007.02.054. URL: https://www.sciencedirect.com/science/article/pii/S0168900207003518.

[24] "SIS18 operation and recent development". In: *JACoW* IPAC2023 (2023), TUPA163. DOI: 10.18429/JACoW-IPAC2023-TUPA163.

[25] H. Geissel et al. "The GSI projectile fragment separator (FRS): a versatile magnetic system for relativistic heavy ions". In: *Nuclear Instruments and Methods in Physics Research Section B: Beam Interactions with Materials and Atoms* 70.1 (1992), pp. 286–297. ISSN: 0168-583X. DOI: https://doi.org/10.1016/0168-583X(92)95944-M. URL: https://www.sciencedirect.com/science/article/pii/0168583X9295944M.

[26] https://www.hamamatsu.com/content/dam/hamamatsu-photonics/sites/documents/99_SALES_LIBRARY/etd/High_energy_PMT_TPMZ0003E.pdf.

[27] https://www.gsi.de/fileadmin/EE/Module/Dokumente/VFTX_Manual_2_0.pdf.

[28] https://www.igus.co.uk/info/drive-technology-dryve-motor-control-system.

[29] Bernd Voss. "A low-mass Multi-Sampling Ionization chamber for fission studies". In: *2011 IEEE Nuclear Science Symposium Conference Record*. 2011, pp. 1767–1770. DOI: 10.1109/NSSMIC.2011.6154679.

[30] D. Cortina-Gil et al. "CALIFA, a Dedicated Calorimeter for the R3B/FAIR". In: *Nuclear Data Sheets* 120 (2014), pp. 99–101. ISSN: 0090-3752. DOI: https://doi.org/10.1016/j.nds.2014.07.017. URL: https://www.sciencedirect.com/science/article/pii/S0090375214004694.

[31] Ben Pietras et al. "First testing of the CALIFA Barrel Demonstrator". In: *Nuclear Instruments and Methods in Physics Research Section A Accelerators Spectrometers Detectors and Associated Equipment* 814 (Apr. 2016), pp. 56–65. DOI: 10.1016/j.nima.2016.01.032.

[32] P Cabanelas et al. "Commissioning of the CALIFA Barrel Calorimeter of the R3B Experiment at FAIR". In: *Journal of Physics: Conference Series* 1667.1 (Oct. 2020), p. 012006. ISSN: 1742-6596. DOI: 10.1088/1742-6596/1667/1/012006. URL: http://dx.doi.org/10.1088/1742-6596/1667/1/012006.

[33] https://www.gsi.de/work/forschung/nustarenna/nustarenna_divisions/kernreaktionen/r3b_project_group/glad.

[34] Bernard Gastineau et al. "Design Status of the R3B-GLAD Magnet: Large Acceptance Superconducting Dipole With Active Shielding, Graded Coils, Large Forces and Indirect Cooling by Thermosiphon". In: *Applied Superconductivity, IEEE Transactions on* 18 (July 2008), pp. 407–410. DOI: 10.1109/TASC.2008.922529.

[35] W. Trautmann. "Experiments at GSI with ALADIN and INDRA". In: *International Workshop on Multifragmentation and Related Topics (IWM 2001)*. Feb. 2002.

[36] A. Bail et al. "Time of flight measurement on the SOFIA experiment". In: *2011 2nd International Conference on Advancements in Nuclear Instrumentation, Measurement Methods and their Applications*. 2011, pp. 1–4. DOI: 10.1109/ANIMMA.2011.6172842.

[37] K. Boretzky et al. "NeuLAND: The high-resolution neutron time-of-flight spectrometer for R3B at FAIR". In: *Nuclear Instruments and Methods in Physics Research Section A: Accelerators, Spectrometers, Detectors and Associated Equipment* 1014 (2021), p. 165701. ISSN: 0168-9002. DOI: https://doi.org/10.1016/j.nima.2021.165701. URL: https://www.sciencedirect.com/science/article/pii/S0168900221006860.

[38] https://www.gsi.de/fileadmin/EE/Module/VULOM/vulom4B_3.pdf.

[39] H.G. Essel and N. Kurz. "The general purpose data acquisition system MBS". In: *IEEE Transactions on Nuclear Science* 47.2 (2000), pp. 337–339. DOI: 10.1109/23.846176.

[40] https://fy.chalmers.se/~f96hajo/drasi/doc/README.html.

[41] Rene Brun et al. *root-project/root: v6.18/02*. Version v6-18-02. June 2020. DOI: 10.5281/zenodo.3895860. URL: https://doi.org/10.5281/zenodo.3895860.

[42] https://fy.chalmers.se/~f96hajo/ucesb/.

[43] Denis Bertini. "R3BRoot, simulation and analysis framework for the R3B experiment at FAIR". In: *Journal of Physics: Conference Series* 331.3 (Dec. 2011), p. 032036. DOI: 10.1088/1742-6596/331/3/032036. URL: https://dx.doi.org/10.1088/1742-6596/331/3/032036.

[44] Dmytro Kresan et al. "Event Reconstruction and Analysis in the R3BRoot Framework". In: *J. Phys. Conf. Ser.* 523 (2014). Ed. by Jianxiong Wang, p. 012034. DOI: 10.1088/1742-6596/523/1/012034.

[45] https://fairroot.gsi.de/.

[46] D. Bazin et al. "The program LISE: a simulation of fragment separators". In: *Nuclear Instruments and Methods in Physics Research Section A: Accelerators, Spectrometers, Detectors and Associated Equipment* 482 (Apr. 2002), pp. 307–327. DOI: 10.1016/S0168-9002(01)01504-2.

[47] L. Chulkov et al. "Quasi-free scattering with 6,8He beams". In: *Nuclear Physics A* 759 (Sept. 2005), pp. 43–63. DOI: 10.1016/j.nuclphysa.2005.05.148.

[48] Meng Wang et al. "The AME 2020 atomic mass evaluation (II). Tables, graphs and references*". In: *Chinese Physics C* 45.3 (Mar. 2021), p. 030003. DOI: 10.1088/1674-1137/abddaf. URL: https://dx.doi.org/10.1088/1674-1137/abddaf.

[49] S. Agostinelli et al. "GEANT4–a simulation toolkit". In: *Nucl. Instrum. Meth. A* 506 (2003), pp. 250–303. DOI: 10.1016/S0168-9002(03)01368-8.

[50] Valerii Panin. private communications.

[51] S. B. Treiman and C. N. Yang. "Tests of the Single-Pion Exchange Model". In: *Phys. Rev. Lett.* 8 (3 Feb. 1962), pp. 140–141. DOI: 10.1103/PhysRevLett.8.140. URL: https://link.aps.org/doi/10.1103/PhysRevLett.8.140.

[52] URL: https://web-docs.gsi.de/~weick/atima/.

[53] URL: https://elog.gsi.de/land/s444_s467/51.

[54] T. Aumann, C. A. Bertulani, and J. Ryckebusch. "Quasifree (p,$2p$) and (p,pn) reactions with unstable nuclei". In: *Phys. Rev. C* 88 (6 Dec. 2013), p. 064610. DOI: 10.1103/PhysRevC.88.064610. URL: https://link.aps.org/doi/10.1103/PhysRevC.88.064610.

[55] L. Sihver, M. Lantz, and A. Kohama. "Improved parametrization of the transparency parameter in Kox and Shen models of total reaction cross sections". In: *Phys. Rev. C* 89 (6 June 2014), p. 067602. DOI: 10.1103/PhysRevC.89.067602. URL: https://link.aps.org/doi/10.1103/PhysRevC.89.067602.

[56] URL: https://www.gsi.de/en/researchaccelerators/fair.

[57] M. Mager. "ALPIDE, the Monolithic Active Pixel Sensor for the ALICE ITS upgrade". In: *Nuclear Instruments and Methods in Physics Research Section A: Accelerators, Spectrometers, Detectors and Associated Equipment* 824 (2016). Frontier Detectors for Frontier Physics: Proceedings of the 13th Pisa Meeting on Advanced Detectors, pp. 434–438. ISSN: 0168-9002. DOI: https://doi.org/10.1016/j.nima.2015.09.057. URL: https://www.sciencedirect.com/science/article/pii/S0168900215011122.

[58] Chenfei Yang et al. "A Prototype Readout System for the ALPIDE Pixel Sensor". In: *IEEE Transactions on Nuclear Science* 66.7 (2019), pp. 1088–1094. DOI: 10.1109/TNS.2019.2913335.

[59] G. Robertis et al. "A MOdular System for Acquisition, Interface and Control (MOSAIC) of detectors and their related electronics for high energy physics experiment". In: *EPJ Web of Conferences* 174 (Jan. 2018), p. 07002. DOI: 10.1051/epjconf/201817407002.

[60] http://fy.chalmers.se/~f96hajo/rataser.

[61] https://web-docs.gsi.de/~bloeher/wrtclk/docs/.

[62] https://fy.chalmers.se/~f96hajo/trloii.

[63] https://wwwcompass.cern.ch/.

[64] https://amber.web.cern.ch/.

[65] Simone Garrafa Botta. "Sviluppo e progettazione della meccanica di supporto al servizio del nuovo tracker di particelle dell'Esperimento CSES-LIMADOU-02". PhD thesis. Polytechnic of Turin, Master's degree course in Mechanical Engineering, 2021.

Appendix A

Appendix

For a function f(x,y,z...) such that errors exist δx,δy,δz ... we can calculate the error for the function using,

$$\epsilon f = \left((\frac{\partial f}{\partial x})^2 (\delta x)^2 + (\frac{\partial f}{\partial y})^2 (\delta y)^2 + (\frac{\partial f}{\partial z})^2 (\delta z)^2 + ... \right)^{\frac{1}{2}} \tag{A.1}$$

We now list some of the useful relations that were used in the error propagation of this thesis.

$$f(x,y) = \alpha x \pm \beta y, \qquad \alpha, \beta \in \mathbb{R}. \tag{A.2}$$

$$\frac{\partial f}{\partial x} = \alpha, \qquad \frac{\partial f}{\partial y} = \pm\beta.$$

$$\epsilon f = \left((\alpha\delta x)^2 + (\beta\delta y)^2\right)^{\frac{1}{2}}. \tag{A.3}$$

$$f(x,y) = \alpha x y, \qquad \alpha \in \mathbb{R}. \tag{A.4}$$

$$\frac{\partial f}{\partial x} = \alpha y, \qquad \frac{\partial f}{\partial y} = \alpha x.$$

$$\epsilon f = \alpha \left((y\delta x)^2 + (x\delta y)^2\right)^{\frac{1}{2}} \tag{A.5}$$

$$f(x,y) = \alpha \frac{x}{y}., \qquad \alpha \in \mathbb{R}. \tag{A.6}$$

$$\frac{\partial f}{\partial x} = \alpha \frac{1}{y}, \qquad \frac{\partial f}{\partial y} = -\alpha \frac{x}{y^2}.$$

$$\epsilon f = \left((\delta x)^2 \left(\alpha \frac{1}{y} \right)^2 + (\delta y)^2 \left(\alpha \frac{x}{y^2} \right)^2 \right)^{\frac{1}{2}}$$

$$\epsilon f = \alpha \left(\frac{xy}{xy} \right) \left(\left((\delta x)^2 \left(\frac{1}{y} \right)^2 + (\delta y)^2 \left(\frac{x}{y^2} \right)^2 \right) \right)^{\frac{1}{2}}$$

$$\epsilon f = \alpha \left(\frac{x}{y} \right) \left(\left(\frac{y}{x} \right)^2 \left((\delta x)^2 \left(\frac{1}{y} \right)^2 + (\delta y)^2 \left(\frac{x}{y^2} \right)^2 \right) \right)^{\frac{1}{2}}$$

$$\epsilon f = f \left(\left(\frac{\delta x}{x} \right)^2 + \left(\frac{\delta y}{y} \right)^2 \right)^{\frac{1}{2}} \tag{A.7}$$

$$f(x,y) = \frac{1}{\alpha x + \beta y}, \qquad \alpha, \beta \in \mathbb{R}. \tag{A.8}$$

$$\frac{\partial f}{\partial x} = -\alpha \left(\frac{1}{\alpha x + \beta y} \right)^2, \qquad \frac{\partial f}{\partial y} = -\beta \left(\frac{1}{\alpha x + \beta y} \right)^2.$$

$$\epsilon f = \left((\alpha\delta x)^2 \left(\frac{1}{x+y} \right)^4 + (\beta\delta y)^2 \left(\frac{1}{x+y} \right)^4 \right)^{\frac{1}{2}}$$

$$\epsilon f = f^2 \left((\alpha\delta x)^2 + (\beta\delta y)^2 \right)^{\frac{1}{2}} \tag{A.9}$$

$$f(x,y) = \alpha ln\left(\frac{x}{y}\right), \qquad \alpha \in \mathbb{R}. \tag{A.10}$$

$$f(x,y) = \alpha ln(x) - \alpha ln(y).$$

$$\frac{\partial f}{\partial x} = \alpha\frac{1}{x}, \qquad \frac{\partial f}{\partial y} = -\alpha\frac{1}{y}.$$

$$\epsilon f = \left(\left(\frac{\alpha\delta x}{x}\right)^2 + \left(\frac{\alpha\delta y}{y}\right)^2\right)^{\frac{1}{2}}$$

$$\epsilon f = \alpha\left(\left(\frac{\delta x}{x}\right)^2 + \left(\frac{\delta y}{y}\right)^2\right)^{\frac{1}{2}}. \tag{A.11}$$

$$f(x,y) = e^{\alpha x+\beta y}, \qquad \alpha,\beta \in \mathbb{R}. \tag{A.12}$$

$$\frac{\partial f}{\partial x} = \alpha f, \qquad \frac{\partial f}{\partial y} = \beta f.$$

$$\epsilon f = \left((\alpha f\delta x)^2 + (\beta f\delta y)^2\right)^{\frac{1}{2}}$$

$$\epsilon f = f\left((\alpha\delta x)^2 + (\beta\delta y)^2\right)^{\frac{1}{2}} \tag{A.13}$$